UNIVERSIDADE ESTADUAL DE CAMPINAS

FACULDADE DE ENGENHARIA QUÍMICA

DIOGO SILVA SANCHES JORQUEIRA

INVESTIGAÇÃO DE MODELO PSEUDO-HOMOGÊNEO PARA SÍNTESE DA AMÔNIA: USO DE UMA ABORDAGEM COMPOSICIONAL

INVESTIGATION OF THE PSEUDO-HOMOGENEOUS MODEL FOR AMMONIA SYNTHESIS: USE OF A COMPOSITIONAL APPROACH

CAMPINAS

2018

DIOGO SILVA SANCHES JORQUEIRA

INVESTIGAÇÃO DE MODELO PSEUDO-HOMOGÊNEO PARA SÍNTESE DA AMÔNIA: USO DE UMA ABORDAGEM COMPOSICIONAL

INVESTIGATION OF THE PSEUDO-HOMOGENEOUS MODEL FOR AMMONIA SYNTHESIS: USE OF A COMPOSITIONAL APPROACH

Dissertation presented to the School of Chemical Engineering of the University of Campinas in partial fulfillment of the requirements for the degree of Master in Chemical Engineering.

Advisor: Prof. Maria Teresa Moreira Rodrigues

ESTE EXEMPLAR CORRESPONDE À VERSÃO FINAL DA DISSERTAÇÃO DEFENDIDA PELO ALUNO DIOGO SILVA SANCHES JORQUEIRA, E ORIENTADO PELA PROFESSORA MARIA TERESA MOREIRA RODRIGUES.

Campinas
2018

Ficha catalográfica
Universidade Estadual de Campinas
Biblioteca da Área de Engenharia e Arquitetura
Luciana Pietrosanto Milla - CRB 8/8129

J769i
Jorqueira, Diogo Silva Sanches, 1992-
Investigation of the pseudo-homogeneous model for ammonia synthesis : use of a compositional approach / Diogo Silva Sanches Jorqueira. – Campinas, SP : [s.n.], 2018.

Orientador: Maria Teresa Moreira Rodrigues.
Dissertação (mestrado) – Universidade Estadual de Campinas, Faculdade de Engenharia Química.

1. Reatores. 2. Compostos de amonia. 3. Equações de estado. 4. Modelagem matemática e simulação. I. Rodrigues, Maria Teresa Moreira, 1955-. II. Universidade Estadual de Campinas. Faculdade de Engenharia Química. III. Título.

Informações para Biblioteca Digital

Título em outro idioma: Investigação de modelo pseudo-homogêneo para síntese da amônia : uso de uma abordagem composicional
Palavras-chave em inglês:
Reactors
Ammonia compounds
State equations
Mathematical modeling and simulation
Área de concentração: Sistemas de Processos Químicos e Informática
Titulação: Mestre em Engenharia Química
Banca examinadora:
Maria Teresa Moreira Rodrigues [Orientador]
Lucimara Gaziola de La Torre
Reinaldo Giudici
Data de defesa: 20-02-2018
Programa de Pós-Graduação: Engenharia Química

Folha de Aprovação da Dissertação de Mestrado defendida por Diogo Silva Sanches Jorqueira e aprovada em 20 de fevereiro de 2018 pela banca examinadora constituída pelos seguintes doutores:

_____

Profa Dra. Maria Teresa Moreira Rodrigues

_____

Profa Dra. Lucimara Gaziola de La Torre

_____

Profa Dr. Reinaldo Giudici

A ATA da Defesa com as respectivas assinaturas dos membros encontra-se no Processo de vida acadêmica do aluno.

DEDICATÓRIA

"I see a beautiful city and a brilliant people rising from this abyss. I see the lives for which I lay down my life, peaceful, useful, prosperous and happy. I see that I hold a sanctuary in their hearts, and in the hearts of their descendants, generations hence. It is a far, far better thing that I do, than I have ever done; it is a far, far better rest that I go to than I have ever known."

Charles Dickens (1812-1870), A Tale of Two Cities (1859)

AGRADECIMENTOS

Seria muito difícil a realização de um trabalho de mestrado sem a colaboração de muitas pessoas comigo. Desta forma os agradecimentos irão se estender um pouco. Fica aqui minha imensa gratidão a:

- A Deus, pelos dias de vida dados a mim e pela sabedoria fornecida;

- A minha mãe Maria e ao meu pai Adilson pela educação dada durante toda a vida e pelos investimentos em meu conhecimento;

- A orientadora e professora Maria Teresa Moreira Rodrigues, pelos conselhos e ajudas dados ao longo do trabalho;

- Ao amigo Antônio Marinho Barbosa Neto, por toda a paciência e dedicação em ensinar os primeiros passos em programação, e por toda a ajuda fornecida até hoje;

- A toda FEQ, por sua estrutura fornecida ao longo dos cinco anos de graduação e dos dois de mestrado. Fica aqui minha gratidão às pessoas do SIFEQ e das coordenações também;

- Aos professores que tive ao longo da graduação, especialmente aos professores José Vicente, Flávio Vasconcelos, Martín Aznar, Oswaldir Taranto e Marisa Beppu;

- Aos colegas Marcos Mendes, Ednir Nigra, Saon Crispim, Mauro Oliveira e Ivan Saavedra pela amizade e conselhos;

- Ao Colégio Santa Maria por toda a formação dada durante o ensino médio, especialmente aos professores Cabral e Severino e à diretora Rosa Amélia;

ABSTRACT

JORQUEIRA, Diogo Silva Sanches. Investigation of the Pseudo Homogeneous Model for Ammonia Synthesis: Use of a Compositional Approach. Campinas: Department of Engineering of Chemical Systems, School of Chemical Engineering, State University of Campinas, 2018. 142 p. Dissertation (Masters).

Ammonia synthesis process completed 100 years in 2013. It was one of the most important inventions in 20th century. Moreover, the process has a variety of temperatures and pressures, going from 1 atm to 300 atm, and from 200 K to 810 K. The ammonia production takes place in reactors from 150 to 300 atm and 600 to 800 K with 30 % of conversion, because it is highly exothermic. Besides, ammonia is a polar gas and hydrogen is a quantic gas in these conditions. Therefore, the prediction of composition, temperature and pressure inside ammonia converters using appropriate models is important. Furthermore, many reaction rates were proposed for ammonia synthesis. However, most of the expressions used chemical activity without computing compositional interactions between components. So, the modeling of reactors using a rigorous thermodynamic model was proposed. The Peng Robinson and Soave Redlich Kwong expressions were used in Singh and Saraf rate expression. Two modes of operations were modeled: adiabatic (which reaction releases heat without removal) and autothermal (non isothermal operation). The catalyst activity was fitted to EoS modeling. Both models were validated with plant data and they presented good reliability. The adiabatic model presented maximum error of 1.6 % with temperature and 11.4 % with conversion. On the other hand, autothermal model presented maximum error of 2.7 % with temperature. Moreover, the sensitivity analysis of input variables was proposed in both models. The adiabatic operation showed more sensitive to inlet pressure and temperature variations, while the autothermal reactor presented higher conversions and better energy removal. In final part, the estimation of properties in mass boundary layer were made. The values of mass diffusion were low due to high pressure and external resistance was significant. However, when it was compared to internal resistance, the resistance computed by effectiveness factor was dominant in ammonia synthesis reactor.

Keywords: Ammonia Converters, Cubic Equations of State, Temkin-Pyzhev Expression, High Temperature and High Pressure.

RESUMO

JORQUEIRA, Diogo Silva Sanches. Investigação de Modelo Pseudo-Homogêneo para Síntese da Amônia: Uso de uma Abordagem Composicional. Campinas: Departamento de Engenharia de Sistemas Químicos, Faculdade de Engenharia Química, Universidade Estadual de Campinas, 2018. 142 p. Dissertação (Mestrado).

O processo de síntese de amônia completou 100 anos em 2013. Esta foi uma das maiores invenções do século XX. Além disso, este processo possui uma elevada gama de temperaturas e pressões, indo de 1 atm a 300 atm e de 200 K até 800 K (na qual a reação pode ocorrer). A produção de amônia acontece em reatores de 150 a 300 atm e de 600 a 810 K, com 30 % de conversão por passe, pois a reação é altamente exotérmica. Mais ainda, a amônia é um gás polar e hidrogênio é um gás quântico nessas condições. Logo, a predição de composição, temperatura e de pressão dentro de reatores de amônia usando modelos apropriados se faz importante. Muitas leis de reação foram propostas. Porém, muitas dessas expressões usavam atividade química sem computar interações entre os componentes. Dessa forma, a modelagem de reatores de amônia utilizando um modelo termodinâmico rigoroso foi proposta neste trabalho. As expressões de Peng e Robinson e de Soave Redlich Kwong foram usadas na taxa de reação proposta por Singh e Saraf. Dois modos de operação foram modelados: adiabático (no qual a reação não troca calor com a vizinhança) e autotérmico (operando não isotermicamente). A atividade catalítica foi ajustada a modelagem por equações de estado. Os dois modelos de reatores foram comparados com dados de planta reais e apresentaram boa concordância. O modelo adiabático apresentou um erro máximo relativo de 1.6 % com a temperatura e de 11.4 % com a conversão. Por outro lado, o modelo autotérmico teve um erro máximo de 2.7 % com a temperatura. Posteriormente uma análise de sensitividade foi realizada em variáveis de entrada de ambos os modelos. A operação adiabática se mostrou mais sensível à variação de pressão e temperatura, enquanto a autotérmica apresentou maiores conversões e melhor remoção de energia. Na parte final, uma estimativa de propriedades na camada limite mássica foi realizada. Os valores de difusão mássica foram pequenos devido à elevada pressão, contudo a resistência externa à transferência de massa se mostrou significativa. Mesmo assim, a maior resistência no reator de síntese de amônia é interna a partícula catalítica.

Palavras-chave: Reatores de Amônia, Equações de Estado Cúbicas, Equação de Temkin-Pyzhev, Alta Temperatura e Alta Pressão.

LIST OF FIGURES

LIST OF TABLES

LIST OF ABBREVIATIONS AND ACRONYMS

HUT	$[m]$	Height of Transfer Unit
TVA	—	Tennessee Valley Authority Reactor
HPHT	—	High Pressure and High Temperature
PR	—	Peng Robinson
SRK	—	Soave Redlich Kwong
BWR	—	Benedict Webb Rubin
VLE	—	Vapor-Liquid Equilibrium
EoS	—	Equation of State
vec	—	Vector
mat	—	Matrix
mix	—	Mixture
PBR	—	Packed Bed Reactor
PFR	—	Plug Flow Reactor
i	—	Substance i

LIST OF SYMBOLS

N_2	–	Nitrogen
H_2	–	Hydrogen
NH_3	–	Ammonia
CH_4	–	Methane
Ar	–	Argon
CO	–	Carbon Monoxide
CO_2	–	Carbon Dioxide
H_2O	–	Water
Ru	–	Ruthenium
Co	–	Cobalt
Mo	–	Molybdenum

LIST OF ROMAN LETTERS

f	–	Catalyst activity
r_{N_2}	$kmol/(m^3.s)$	Nitrogen consumption rate
r or r_{NH_3}	$kmol/(m^3.s)$	Ammonia production rate
r_{direct}	$kmol/(m^3.s)$	Direct nitrogen consumption rate
$r_{reverse}$	$kmol/(m^3.s)$	Reverse nitrogen consumption rate
p_i	atm	Partial pressure of substance i
k_1	$kmol/(m^3.s.atm^{1.5})$	Rate constant of direct rate in Temkin and Pyzhev rate
k_2	$kmol/(m^3.s.atm^{-0.5})$	Rate constant of reverse rate in Temkin and Pyzhev rate
T	K	System temperature
R	$J/(mol.K)$	Ideal gas constant
$k_1{'}$	$kmol/(m^3.s.atm)$	Reaction rate constant in Temkin et al. expression
K_a	–	Dimensionless equilibrium constant in chemical activities
a_i	–	Chemical activity of substance i
K_3	–	Adsorption constant in Nielsen's rate
K_{eq}	–	Equilibrium constant for ammonia rate
P_{in}	atm or bar	Inlet pressure in ammonia reactor
y_i	–	Molar fraction of substance i in reactor

P	Pa	System pressure in reactor
P_{Rep}	Pa	Repulsive term in cubic EoS
P_{Att}	Pa	Attractive term in cubic EoS
v	m^3/mol	Molar volume of gaseous system
b	m^3/mol	Covolume term for cubic EoS
$a(T)$	$(Pa.m^6)/mol^2$	Function of temperature in cubic EoS
A_{mix}	–	Mixture term for cubic EoS computing interactions
B_{mix}	–	Mixture term for cubic EoS computing interactions
Z	–	Gas compressibility factor
Z_{mix}	–	Mixture compressibility factor
p,q,r	–	Auxiliary factors for Z_{mix} calculation
s,t,u,w	–	Auxiliary factors for Z_{mix} calculation
T_{c_i}	K	Critical temperature of component i
T_{r_i}	–	Reduced temperature of component i
P_{c_i}	Pa	Critical pressure of component i
P_{r_i}	–	Reduced pressure of component i
k_{ij}	–	Binary interaction parameter
c_i	m^3/mol	Correction factor in volume shift for i component
Z_{RA_i}	–	Rackett compressibility factor for i component
$\hat{f}_i^g$	Pa	Fugacity of i component in gaseous mixture
H_{mix}	J/mol	Real enthalpy of mixture
H_{mix}^{res}	J/mol	Residual enthalpy of mixture
H_{mix}^{ig}	J/mol	Ideal gas enthalpy of mixture
$\left(\dfrac{da}{dT}\right)$	$(Pa.m^6)/(mol^2.K)$	First derivative of $a(T)$ related to temperature
$\left(\dfrac{d^2a}{dT^2}\right)$	$(Pa.m^6)/(mol^2.K^2)$	Second derivative of $a(T)$ related to temperature
$C_{p_{mix}}$	$J/(mol.K)$	Real heat capacity at constant pressure of mixture
$C_p^{res}{}_{mix}$	$J/(mol.K)$	Residual heat capacity at constant pressure of mixture
$C_p^{ig}{}_{mix}$	$J/(mol.K)$	Ideal gas heat capacity at constant pressure of mixture
U_{mix}	J/mol	Real internal energy of mixture
U_{mix}^{res}	J/mol	Residual internal energy of mixture

U_{mix}^{ig}	J/mol	Ideal gas internal energy of mixture
$C_{v_{mix}}$	$J/(mol.K)$	Real heat capacity at constant volume of mixture
$C_v^{res}{}_{mix}$	$J/(mol.K)$	Residual heat capacity at constant volume of mixture
$C_v^{ig}{}_{mix}$	$J/(mol.K)$	Ideal gas heat capacity at constant volume of mixture
$Rate_i$	$mol/(m^3.s)$	Global reaction rate of component i
b_o-b_6	$-$	Experimental coefficients for η calculation
x_{N_2}	$-$	Nitrogen conversion
L	m	Reactor length
V	m^3	Reactor volume
y_i^o	$-$	Molar fraction of substance i in reactor inlet
ΔH_r	J/mol	Heat of reaction for ammonia synthesis
$\dot{m}$	kg/s	Mass flow inside the reactor
A	m^2	Sectional area of the reactor
T	K	Reactant gas temperature in reactor models
T_g	K	Cooling gas temperature in autothermal reactor
U	$W/(m^2.K)$	Overall heat transfer coefficient in autothermal converter
A'	m^2/m	Specific heat exchange area in length
a'	m^2/m^3	Specific heat exchange area in volume
u	m/s	Superficial velocity of gas in reactor
d_p	m	Particle diameter
D_i^o	m^2/s	Mass diffusivity of component i in mixture in 273 K and 1 atm
Sc_i	$-$	Schmidt number for i component
Re_p	$-$	Reynolds number for particle
j_d	$-$	Colburn factor for mass transfer
G	$kg/(m^2.s)$	Mass flow rate inside the reactor
Sh	$-$	Sherwood number
k_c	m/s	Mass transfer coefficient
N_i	$mol/(m^2.s)$	Molar flux in reactor
ΔC_i	mol/m^3	Concentration differences in boundary layer
a_g	m^2	External area of catalyst particle
v_g	m^3	Volume of catalyst particle

h	m or m^3	Step size along the reactor in numerical method

LIST OF GREEK LETTERS

ρ	mol/m^3	Molar density of gaseous system
δ_1	–	Constant for cubic *EoS* (*PR* or *SRK*)
δ_2	–	Constant for cubic *EoS* (*PR* or *SRK*)
ω	–	Acentric factor
$f(\omega_i)$	–	Acentric factor function
$\hat{\phi}_i^g$	–	Fugacity coefficient in gas phase
α_i	–	Function for reduced temperature
Ω_a, Ω_b	–	Constants for cubic *EoS* (*PR* or *SRK*)
Δ, ψ_i	–	Auxiliary factors for $\hat{\phi}_i^g$ calculation
τ_i, ξ	–	Auxiliary factors for $\hat{\phi}_i^g$ calculation
η	–	Effectiveness factor inside the catalyst pellet
ε	–	Bed porosity
μ	$Pa.s$	Gas viscosity
δ	m	Boundary layer thickness

SUMMARY

1 INTRODUCTION

In this introduction, the importance of studies of ammonia synthesis are discussed, as well as the motivation for continuing research along the years. In addition, the ammonia production process and main reactions are explained briefly.

1.1 Ammonia Importance

The development of the ammonia production process in the 20th century begun with systematic catalytic research and the widespread use of catalysts in industrial chemistry. Many subsequent achievements in the theoretical understanding and practical application of heterogeneous catalysis have their roots in the ammonia synthesis reaction, which is the best-understood catalytic process, as demonstrated by the enormous number of publications (APPL, 1999). Ammonia is one of the most important, large volume synthetic chemicals produced worldwide. More than 80% of fertilizer manufacturing is coupled with ammonia production. Besides this, ammonia is also an essential substance in the production of nitric acid and ethanol amines. In 2014, NH_3 global production reached 176 million tons and it is forecasted to be near 239 million tons in 2020 (ANANTHARAMAN et al., 2012).

Furthermore, the ammonia production should be a strategic sector of chemical industry in Brazil, because it is the 4th agriculture in the world. However, our country is only in the 27th place in fertilizers production. Moreover, about 75 % of fertilizers used in Brazil are imported (ANDA, 2012). Then, the value spent with fertilizers importations rise in economic crisis, due to dollar conversion. This problem could be solved investing in more professionals with knowledge in ammonia production. Therefore, research for a better comprehension of ammonia synthesis is still necessary.

1.2 Ammonia Synthesis Process

A concise ammonia production flowchart is illustrated in Figure 1.1. The first stage is the pre-treatment of natural gas. Sulfur needs to be removed because it is a poison to iron catalysts. After pre-treatment, reforming occurs to produce a syngas (mixture of CO and H_2). Synthesis gas production is the step in which CH_4 and minor hydrocarbons react to produce H_2, CO and CO_2. The principle method used is steam reforming, which uses steam to produce energy for the main reactions. Reactors are divided into primary and secondary reforming.
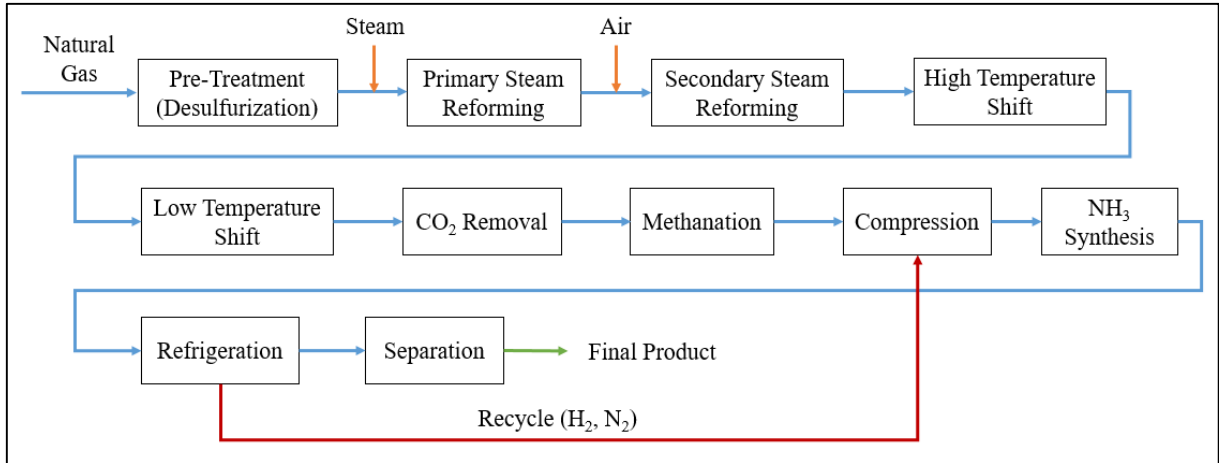
Figure 1.1. Basic flowchart of ammonia production (APPL, 1999).

In primary reforming, CH_4 and steam are converted to synthesis gas, as given in Equation (1.1). In addition, CO is also converted into CO_2 (shift reaction in Equation (1.2)) and CH_4 suffers methanation (Equation (1.3)). The primary reactor operates at 1000 K and 30 atm, because main reactions ((1.1) and (1.3)) are strongly endothermic. The H_2/CO ratios produced are between 3 and 5 depending on the feedstock.

$$CH_{4(g)} + H_2O_{(g)} \leftrightarrow CO_{(g)} + 3H_{2\ (g)} \quad \Delta H_R^o = 206\ kJ/mol\ CH_4 \tag{1.1}$$

$$CO_{(g)} + H_2O_{(g)} \leftrightarrow CO_{2(g)} + H_{2\ (g)} \quad \Delta H_R^o = -41\ kJ/mol\ CO \tag{1.2}$$

$$CH_{4(g)} + 2H_2O_{(g)} \leftrightarrow CO_{2(g)} + 4H_{2\ (g)} \quad \Delta H_R^o = 165\ kJ/mol\ CH_4 \tag{1.3}$$
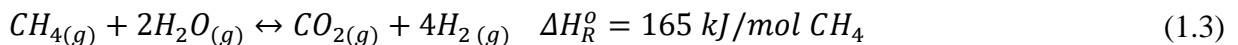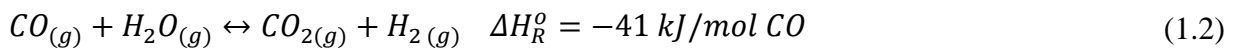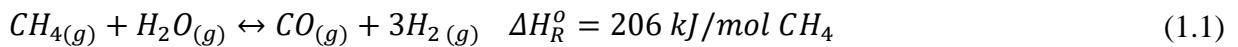
In secondary reforming, synthesis gas and shift reaction also occur. In addition, O_2 from the air reacts with H_2 and CH_4 reacts with CO, as given in Equation (1.4) and Equation (1.5) respectively.

$$CH_{4(g)} + 2CO_{(g)} \leftrightarrow CO_{2(g)} + 2H_2O_{(g)} \quad \Delta H_R^o = -581.6\ kJ/mol\ CH_4 \tag{1.4}$$

$$H_{2\ (g)} + 0.5O_{2\ (g)} \leftrightarrow H_2O_{(g)} \quad \Delta H_R^o = -241.8\ kJ/mol\ H_2O \tag{1.5}$$
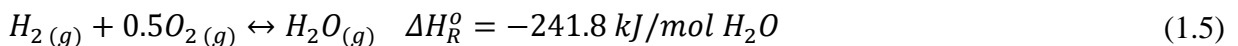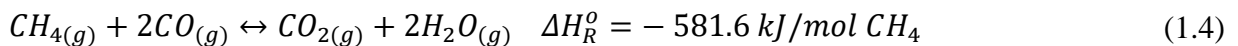
A nickel catalyst is used at 1200 K. The steam used to cool this gas is usually operated in turbines and compressors to preheat reactants. At the end of the secondary reforming, most of CH_4 is converted into CO. Our gas mixture also contains N_2, H_2, H_2O and Ar.

The remaining CO is converted into more H_2 (Equation (1.2)) in shift converters. The reaction occurs with steam at two stages, because it is exothermic. In the first the converter

(High Temperature Shift Reactor), temperature reaches 700 K in an iron/chromium oxide catalyst. In the second reactor (Low Temperature Shift Reactor), gas is at 500 K in a copper-zinc catalyst. The second converter temperature decreases because low temperatures produce high contents of CO_2.

In the next stage, CO_2 needs to be removed, because it is a greenhouse gas and it can disturb NH_3 synthesis. The removal is performed by an absorption operation, usually with amines. The last traces of CO and CO_2 are removed in methanation reactions, as described in Equations (1.6) and (1.7).

$$CO_{(g)} + 3H_{2\,(g)} \leftrightarrow CH_{4(g)} + H_2O_{(g)} \quad \Delta H_R^o = -205.8 \; kJ/mol \; H_2O \tag{1.6}$$

$$CO_{2(g)} + 4H_{2\,(g)} \leftrightarrow CH_{4(g)} + 2H_2O_{(g)} \quad \Delta H_R^o = -165 \; kJ/mol \; CO_2 \tag{1.7}$$
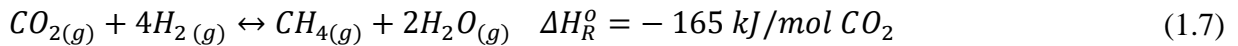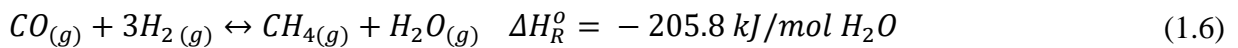
Now the reaction gas contains N_2, H_2, NH_3, CH_4 and Ar. The gas needs to be compressed for synthesis reaction. There are no side reactions and the product is stable, as given in Equation (1.8) (SINGH and SARAF, 1979). In the reaction system, NH_3 is produced.

$$N_{2(g)} + 3H_{2(g)} \leftrightarrow 2NH_{3(g)} \quad \Delta H_R^o = -45.94 \; kJ/mol \; NH_3 \tag{1.8}$$
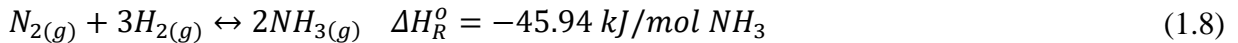
Observing Equation (1.8), the reaction is exothermic and there is a decrease in mole numbers. However, NH_3 synthesis in industry occurs in the gas phase with the presence of iron catalysts, at high temperatures and high-pressure ranges, from 573-820 K and 150-300 atm (KIROVA-YORDANOVA, 2004). The temperatures are higher in industry for higher rates, even for an exothermal reaction. However, conversions per pass are usually less than 35% in these operations. For this reason, the gas is recycled back to the reactor. After synthesis, the outlet stream is condensed and separated as NH_3, the final product. In this step, N_2 and H_2 are recycled to the reactor.

A first estimation of mass and energy balances in ammonia production can be done in commercial simulators, such as Aspen®, Hysys® and Pro II®. After all, most of the equipment is easily simulated in these programs, even in *HPHT* (High-Pressure and High Temperature) conditions. Moreover, one advantage of commercial simulators is their thermodynamic databank, which is constantly updated year by year.

1.3 Research Motivation

When a more detailed study is needed, simulators cannot offer many alternatives, though. The limitation of the simulators is obvious in reactor modules. The reaction rates must be specified in standard expressions. Moreover, they are usually computed using molar fraction, concentration or partial pressure. If a rate cannot be changed to simulator pattern it cannot be used at first. Instead, the user would have to program inside simulators, where many are black-box types.

For catalyst reactors in simulators, one can calculate a correction for reaction rate. However, process simulators consider a constant effectiveness factor η along the reactors, which normally is a limitation. After all, if the composition changes along the converter (for example, in a tubular reactor), the correction factor η also varies. Moreover, basic calculations of gradient concentrations in the boundary layer are not performed either. However, even in turbulent conditions, these differences exist. Therefore, if the user wants to perform such estimations, he must build a program outside the software, or link a code to simulator.

In this work, many rate expressions use fugacity in the gas phase and a correlation for effectiveness factor along the reactor. Therefore, a programming language is used to solve all the equations used. The environment and language used to program is Wolfram Mathematica®.

2 OBJECTIVES

In this part of the work, the objectives are divided into general and specific. The present work aims to model ammonia reactors with a more rigorous approach. The general objectives are related to thermodynamic and kinetic modeling. The specific objectives involve thermodynamic properties and computation and numerical methods.

2.1 General Objectives

For this dissertation, the general objectives are:

- Proposal of two reactor models for simulation: adiabatic and autothermal.
- Validation of both models with plant data.
- Use of kinetic expressions (especially Temkin-Pyzhev modified expression) in ammonia reactor models.
- Solution of mass, energy and momentum balances in ammonia synthesis converters.
- Contribute to software development with a module in ammonia converters.

2.2 Specific Objectives

The following specific objectives of this dissertation achieves the previous general objectives:

- Study thermodynamic models for *HPHT* conditions in ammonia synthesis reactors (Peng-Robinson and Soave-Redlich-Kwong).
- Program fixed and variable step Runge-Kutta Method.
- Compute variations in conversion, temperature and pressure along the reactor using effectiveness factor in pseudo-homogeneous expressions.
- Estimate differences of concentration in the boundary layer.
- Discuss differences between a rigorous thermodynamic model and a correlation on rate expressions.

3 LITERATURE REVIEW

In this section, the literature review is divided into four parts: ammonia synthesis catalysts, historical development of ammonia synthesis kinetic expressions, operation modes in ammonia reactors and ammonia converters modeling.

3.1 Ammonia Synthesis Catalysts

In Equation (1.8), that describes ammonia synthesis, it can be seen that products (right side) present lesser mole numbers than the reactants (left side). Moreover, the reaction is exothermic. So, according to thermodynamics, the highest equilibrium conversions are achieved in low temperature and high-pressure conditions, as expressed in Figure 3.1.
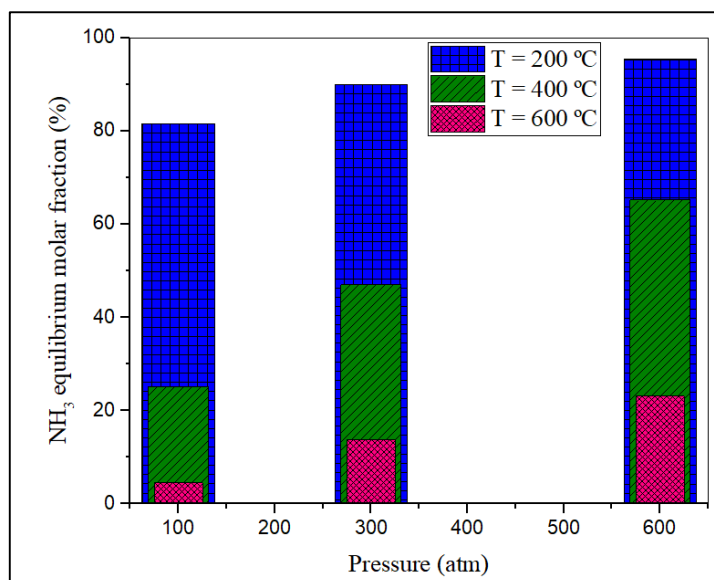
Figure 3.1. NH_3 equilibrium percentage in H_2/N_2 mixture 3:1 (LARSON and DODGE, 1923).

However, in industrial conditions, low temperatures do not provide high reaction rates, requiring larger reactors. Then, high temperatures are necessary to guarantee a high rate. Moreover, the reaction is not feasible in homogeneous phase due to high dissociation energies of N_2 and H_2 molecules (APPL, 1999). Therefore, reaction must happen in a catalyst particle. It makes industrial ammonia synthesis a heterogeneous catalysis challenge.

From 1909 to 1911, 2500 types of different catalysts were tested 6500 times by BASF. The selection trial continued until 1922, when 5000 catalysts systems were tested. Since the beginning, iron has been known as the best substance for ammonia synthesis.

In iron catalysts, ammonia synthesis can be schemed as the following individual steps, as shown in Equations (3.1) to (3.7):

$$H_{2(g)} + * \leftrightarrow 2H* \tag{3.1}$$

$$N_{2(g)} + * \leftrightarrow N_2* \tag{3.2}$$

$$N_2* \leftrightarrow 2N* \tag{3.3}$$

$$N* + H* \leftrightarrow NH* \tag{3.4}$$

$$NH* + H* \leftrightarrow NH_2* \tag{3.5}$$

$$NH_2* + H* \leftrightarrow NH_3* \tag{3.6}$$

$$NH_3* \leftrightarrow NH_3 + * \tag{3.7}$$
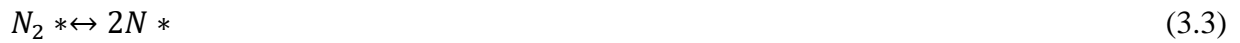
The energy profile for reactions is exposed in Figure 3.2. A catalyst helps the reaction decreasing activation energy. The adsorption and dissociation of N_2 in catalyst requires a large amount of energy.
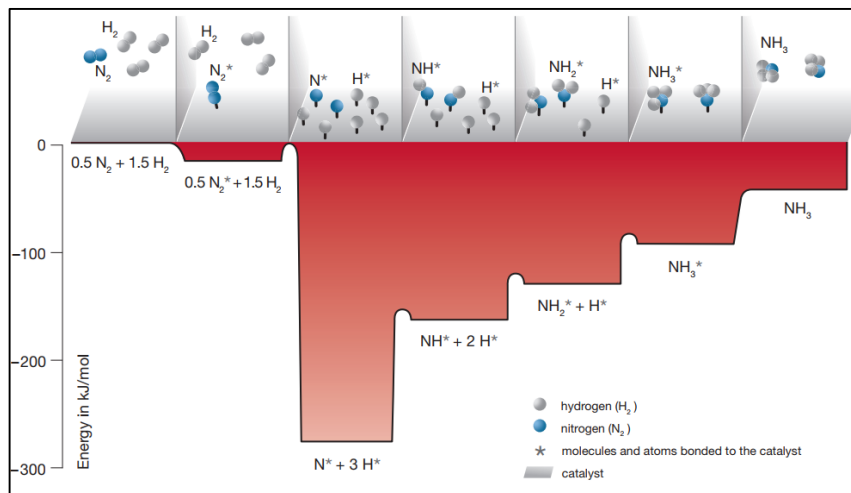
Figure 3.2. Schematic energy profile in ammonia reaction on Fe catalysts (energy in kJ/mol) (BASF, 2006).

Nowadays, the most used catalyst is a magnetite-based fused iron with a small number of promoters with a lifetime of 8 years (LIU, 2013). New catalysts containing Ru and Co-Mo have also been researched, however their costs are still high for industrial applications.

3.2 Historical Development of Ammonia Synthesis Kinetic Expressions

Scientific literature contains several examples of reaction rates for ammonia synthesis. In 1939, the first acceptable approach to rate expression was proposed by Temkin and Pyzhev (TEMKIN and PYZHEV, 1939). As described in Equation (3.8), this rate depends on partial pressure of hydrogen, nitrogen and ammonia. Over the years, this expression has been the most used in ammonia reactor design. Besides it is a sum of a direct rate r_{direct} and a reverse rate $r_{reverse}$.

$$r_{N_2} = r_{direct} - r_{reverse} = f. \left\{ k_1 \left[\frac{p_{N_2} \cdot p_{H_2}^{1,5}}{p_{NH_3}} \right] - k_2 \left[\frac{p_{NH_3}}{p_{H_2}^{1,5}} \right] \right\} \tag{3.8}$$

In the expression above, the term r_{N_2} is nitrogen consumption rate $[kmol/(m^3.s)]$, f is catalyst activity $[-]$, k_1 is direct reaction constant $[kmol/(m^3.s.atm^{1.5})]$, k_2 is reverse reaction constant $[kmol/(m^3.s.atm^{-0.5})]$, and p_i partial pressure of substance i $[atm]$. The kinetic constants k_1 and k_2 follow Arrhenius Law, as given in Equations (3.9) and (3.10):

$$k_1 = 4.971. exp\left(\frac{-87027}{R.T}\right) \tag{3.9}$$

$$k_2 = 7.1428 \times 10^{12}. exp\left(\frac{-198322}{R.T}\right) \tag{3.10}$$

In relations above, T is system temperature $[K]$ and R is the ideal gas constant $[Pa.m^3/mol.K]$. Moreover, in Equation (3.8), when ammonia partial pressure reaches zero, the rate r_{N_2} approaches infinite. Therefore, there is a numerical indetermination. For dilute ammonia concentrations, Temkin and contributors developed another expression, given by Equation (3.11) (TEMKIN et al., 1963). In Equation (3.11), $k_1{'}$ is the reaction rate constant $[kmol/(m^3.h.atm)]$.

$$r_{N_2} = k_1{'}. p_{N_2}{}^{\alpha}. p_{H_2}{}^{1-\alpha} \tag{3.11}$$

Equation (3.12) was also developed by Temkin and collaborators. This equation corrected previous relations and considered two consecutive steps in the surface reaction. The first is chemisorption of nitrogen followed by a chemisorbed nitrogen molecule with hydrogen giving a radical (TEMKIN et al., 1963). These hypotheses led to Equation (3.12). In relation (3.12) K_a is the equilibrium constant in terms of chemical activity $[-]$ and α is the catalyst activity $[-]$.

$$r_{N_2} = k_2.p_{N_2}{}^{1-\alpha}.\left[\frac{1 - \left(\dfrac{p_{NH_3}{}^2}{K_a.p_{N_2}.p_{H_2}{}^3}\right)}{\left[\left(\dfrac{1}{p_{H_2}}\right) + \left(\dfrac{1}{K_a}\right) + \left(\dfrac{p_{NH_3}{}^2}{p_{N_2}.p_{H_2}{}^3}\right).\left(1 + \dfrac{1}{p_{H_2}}\right)\right]^{(1-\alpha)}}\right] \tag{3.12}$$

Later Nielsen proposed a new equation based on chemical activities, due to high pressure and high temperature conditions (NIELSEN, 1968). Nielsen's data are also considered a reference for kinetic treatment. His expression is shown in Equation (3.13).

$$r_{N_2} = k_2.\left[\frac{a_{N_2}.K_a{}^2 - \left(\dfrac{a_{NH_3}{}^2}{a_{H_2}{}^3}\right)}{\left(1 + K_3.\dfrac{a_{NH_3}}{a_{H_2}{}^{1.5}}\right)^{1.5}}\right] \tag{3.13}$$

In the expression above, a_i is the chemical activity of substance $[-]$, k_2 is a kinetic constant $[kmol/m^3.h]$ in Arrhenius Law format, and K_3 is an adsorption constant $[-]$. More details for kinetic constants are given in Equations (3.14) and (3.15).

$$k_2 = 2.0417 \text{ x } 10^9.exp\left(\frac{-59040}{R.T}\right) \tag{3.14}$$

$$K_3 = 3.07 \text{ x } 10^{-2}.exp\left(\frac{81006}{R_g.T}\right) \tag{3.15}$$

Also, in 1968, Dyson and Simon proposed an expression based on chemical activities. This expression (Equation (3.16)) was a modification of the classic Temkin and Pyzhev relation (DYSON and SIMON, 1968).

$$r_{NH_3} = k_2.\left[K_{eq}{}^2.a_{N_2}.\left(\frac{a_{H_2}{}^3}{a_{NH_3}{}^2}\right)^\alpha - \left(\frac{a_{NH_3}{}^2}{a_{H_2}{}^3}\right)^{1-\alpha}\right] \tag{3.16}$$

In equation (3.16), k_2 is the reaction rate constant $[kmol/m^3.s]$, α is the kinetic fitting parameter $[-]$, and K_{eq} is the equilibrium constant $[-]$. The constant k_2 is given in equation (3.17).

$$k_2 = 4.91611 \text{ x } 10^{11}.exp\left(\frac{-170561}{R.T}\right) \tag{3.17}$$

In literature, some authors discuss about differences in α. Temkin suggested that α = 0.5 for all iron catalysts (TEMKIN and PYZHEV, 1939). However, Dyson and Simon

proposed that α vary from 0.5 to 0.75 in iron pellets (DYSON and SIMON, 1968). They used both values, which gave a good fit for their kinetic expression. Nielsen also published that α varied in a range of values. Moreover, even for two different operational conditions, values of α showed differences for the same catalyst (GUACCI et al., 1977). Therefore, this parameter can be used to adjust kinetic data in reaction rates.

In non-rigorous thermodynamic modeling, the activity coefficients φ are computed with the Lewis-Randall rule, as demonstrated in Equations (3.18), (3.19) and Table 3.1. Index i is related to substances N_2 and NH_3, while j corresponds to H_2. Temperature is used in $[K]$ and pressure in $[atm]$.

$$\varphi_i = A + B.T + C.P - D.T^2 + E.P^2 \tag{3.18}$$

$$\varphi_j = exp\left\{P.exp[(-A.T^{0.125} + B)] - P^2.exp[(-C.T^{0.5} - D)] \right.$$
$$\left. + 300.exp\left(-\frac{P}{300}\right).exp[-E.T - F]\right\} \tag{3.19}$$

Table 3.1. Fugacity coefficients in ammonia synthesis (Adapted from (DYSON and SIMON, 1968)).

Coefficient	N_2	H_2	NH_3
A	$9.3431737.10^{-1}$	-3.8402	$1.438996.10^{-1}$
B	$2.0285380.10^{-4}$	$5.41.10^{-1}$	$2.0285380.10^{-3}$
C	$2.9589600.10^{-4}$	$-1.263.10^{-1}$	$-4.4876720.10^{-4}$
D	$-2.7072700.10^{-7}$	$-1.598.10^{1}$	$-1.1429450.10^{-6}$
E	$4.7752070.10^{-7}$	$-1.1901.10^{-2}$	$2.7612160.10^{-7}$
F	$-$	-5.491	$-$

The equilibrium constant K_{eq} is computed in Equation (3.20) (GILLESPIE and BEATTIE, 1930).

$$K_{eq} = 10^{\left[-2.691122.log_{10}^{T}-50.951925.T+1.848863.10^{-7}.T^2+\left(\frac{2001.6}{T}\right)+2.689\right]} \tag{3.20}$$

Another challenge of ammonia synthesis is the variety of rate expressions. Buzzi Ferraris and others made important contributions to ammonia kinetics. Several expressions had

data regression and were tested as an alternative to all previous kinetics. They also concluded that in ammonia synthesis only mathematical analysis of kinetic data is not sufficient for giving an unambiguous response on the nature of the mechanism (associative or dissociative). Furthermore, the differences between catalyst particle and gas can make difficult interpretation of data (BUZZI FERRARIS et al., 1974).

Another model was developed by Guacci and collaborators. They used their own kinetic data to modify reaction constant k_2. Their result is shown in Equation (3.21) (GUACCI et al., 1977).

$$r_{NH_3} = 2.893 \times 10^{12}. exp\left(\frac{-185857}{R.T}\right).\left[K_{eq}{}^2.a_{N_2}.\left(\frac{a_{H_2}{}^3}{a_{NH_3}{}^2}\right)^{0.541} - \left(\frac{a_{NH_3}{}^2}{a_{H_2}{}^3}\right)^{0.459}\right] \quad (3.21)$$

Singh and Saraf also developed their own kinetic model in the Montecatini catalyst. The expression also used activities to compute non-ideal conditions (SINGH and SARAF, 1979). This expression is also a change in original Temkin and Pyzhev expression.

$$r_{NH_3} = 4.1105 \times 10^{10}. exp\left(\frac{-163422}{R.T}\right).\left[K_{eq}{}^2.a_{N_2}.\left(\frac{a_{H_2}{}^3}{a_{NH_3}{}^2}\right)^{0.55} - \left(\frac{a_{NH_3}{}^2}{a_{H_2}{}^3}\right)^{0.45}\right] \quad (3.22)$$

3.3 Operation Modes of Ammonia Synthesis Reactors

The main part of all ammonia synthesis loops is the converter, as expressed in Figure 1.1. One of the advantages of the ammonia process is that only one reaction happens in the reactor. Therefore, parallel reactions do not exist (SINGH and SARAF, 1979). Most ammonia plants nowadays are designed for 1000 t of NH_3/d production. Typical values for volumetric flows and NH_3 concentration in ammonia reactors are given in Table 3.2.

In Table 3.2, it is noted that for minor pressures, the ammonia content in the outlet stream is smaller than for higher pressures (17.1 % versus 19.9 %). This is explained by Le Chatelier's principle, because a more compressed reaction volume favors product formation (see mole numbers variation in Equation (1.8)). The inert content for minor pressures is also less than for high pressures. It happens because as more ammonia is produced, more energy is released by the reaction, requiring heat removal. Therefore, if the same inert content is used, the temperature rises above operational limits (the limit of most iron catalysts is about 810 K).

Table 3.2. Average operating parameters for modern NH_3 synthesis converters (1000 t/d NH_3) (APPL, 1999).

Parameters	P_{in} (140 bar)	P_{in} (220 bar)
Inlet flow (Nm³/h)	5×10^5	4.07×10^5
Inlet y_{NH_3}	4.1	3.8
Outlet y_{NH_3}	17.1	19.9
Inlet y_{inerts}	8.0	12

Moreover, oxygen is a poison to iron catalyst, as reported in Figure 3.3. Therefore, the separation of oxygen and nitrogen before the reaction is also important. Usually in the reactor inlet the O_2 content is about 10 ppm.
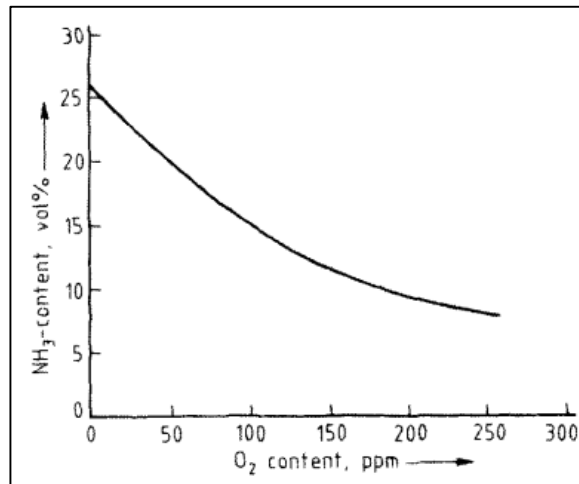
Figure 3.3. Ammonia content in outlet stream in reactor varying oxygen content in feed (APPL, 1999).

The design of an ammonia converter needs attention. First, the reaction releases energy, then, heat removal is required. Second, the high pressure in the reactor deviates gas from ideal conditions, changing thermodynamic and transport properties along it. Therefore, commercial ammonia converters are classified into two main groups: Internally Cooled Converters and Multibed Converters (APPL, 1999).

The internally cooled converters are operated similarly to a heat exchanger. The cooling tubes can run inside the catalyst bed or the catalyst can be put inside tubes with the cooling medium outside the shell. Cooling gas can flow counter or co-currently to the catalyst volume, which is inside the tubes. Moreover, water cannot be used due to the high mass flow

required (high-energy removal required). These converters are shown in Figure 3.4 (a) and Figure 3.4 (b). One disadvantage of this operation is that good heat transfer in each tube is not guaranteed. Therefore, this design has to be studied further for large scale production.

(a)   (b)
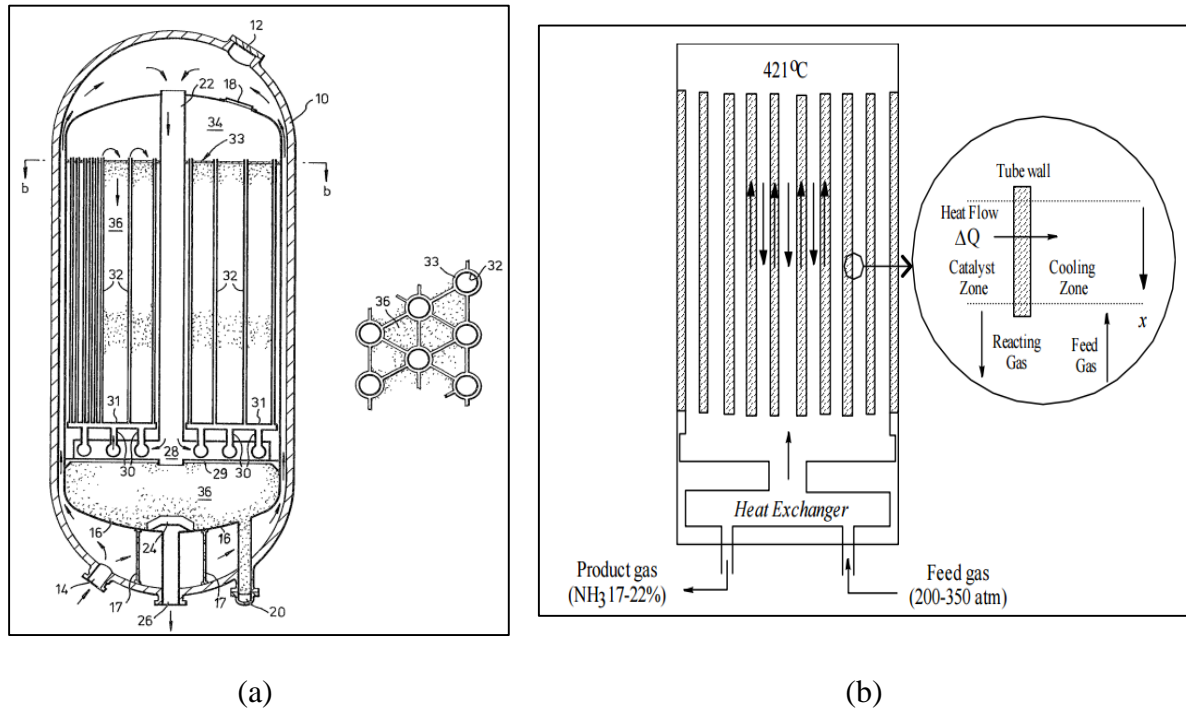
Figure 3.4. (a) Ammonia synthesis converter with catalyst outside cooling tubes (ALWYN PINTO, 1987) and (b) Autothermal ammonia reactor with catalyst inside tubes (EDGAR et al., 2001).

Another possible operation is the Multibed Converter. The use of only one bed is not possible due to the high flows and heat released by the reaction. Therefore, the division of the reactional volume into several beds is suggested. In this operation, heat is not removed along the bed (adiabatic model) and the outlet stream of each reactor is cooled before entering the next converter. The main differences relate to how the outlet streams are cooled. If the exit is refrigerated with direct injections (feed bypass), we have Direct Cooling Reactors, or Quench Converters. If the refrigeration is indirect, the reactor is called an Indirect Cooling Reactor (APPL, 1999).

In Quench Converters, the cooling injection is made of unconverted synthesis gas, as given in Figure 3.5. In these reactors, only a fraction of the recycled gas enters, at about 400 ºC. The exit temperature is approximately 780 K (catalyst deactivates at 820 K). Before entering the next bed, the gas is quenched by recycled gas (400 to 670 K). However, there are disadvantages in this operation. Not all recycled gas passes over the entire reactional volume,

so the product formation occurs at higher ammonia concentrations, providing smaller reaction rates. Therefore, the reactor volume necessary is higher compared to Multibed Reactors. In Indirect Cooling Converters, the heat exchange is indirect. In other words, heat exchangers and boilers are used. One of the most known converters is the Haldor- Topsøe S200 and Kellogg horizontal converters, as shown in Figure 3.6 (a) and Figure 3.6 (b).
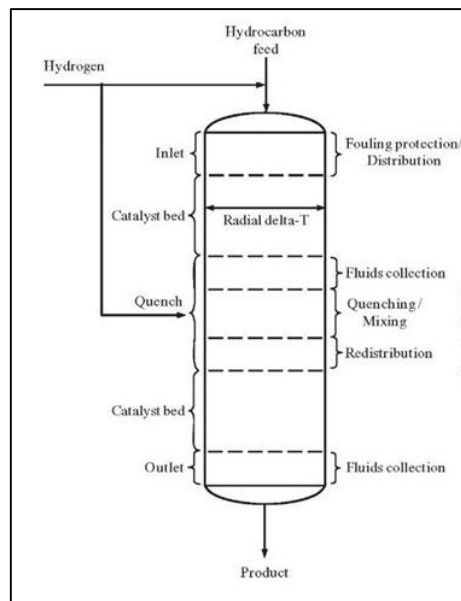
Figure 3.5. Quench cooler converter for hydrotrating process for petroleum refining. (WHAT-HENT-HOW, 2017).

(a) (b)
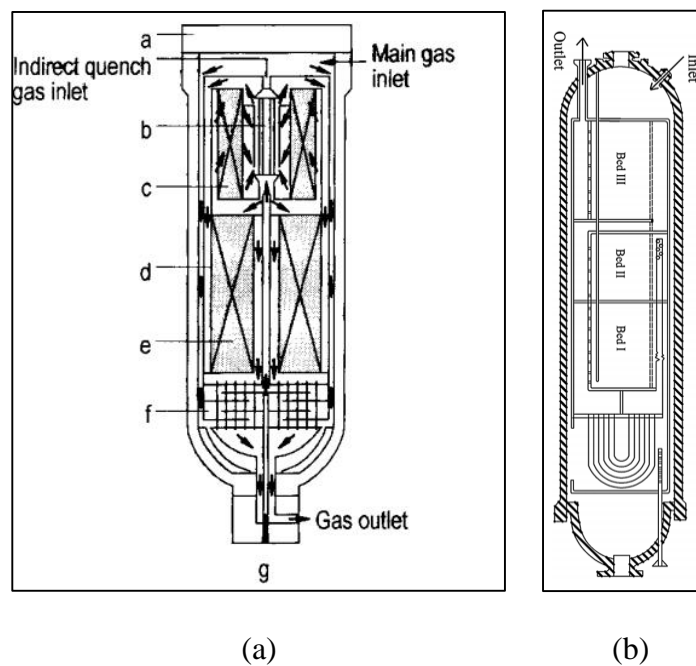
Figure 3.6. (a) Haldor-Topsøe S200 Converter (APPL, 1999) with radial flow and (b) Horizontal intercooling converter (AZARHOOSH et al., 2014).

Another important parameter in ammonia synthesis reactors is the flow pattern. The converters can present radial - Figure 3.6 (a), axial - Figure 3.6 (b), or axial-radial flows - Figure 3.7. Radial converters have fewer pressure drop problems. Consequently, with this configuration, it is possible to design reactors with high production and less catalyst volume, even with minor pellets. On the other hand, axial converters present higher pressure drop, with a less sophisticated design. Therefore, they need to have larger catalyst particles, presenting less activity and requiring a greater depth of bed, because the diameter has a constant value. The axial-radial flow reactor combines the advantages of both previous modes. This converter is shown in Figure 3.7.
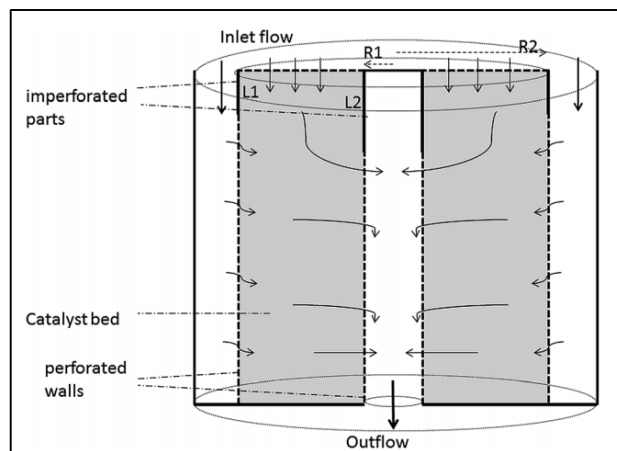
Figure 3.7. Axial-radial ammonia reactor (FARIVAR and EBRAHIM, 2014).

3.4 Historical Development of Ammonia Reactor Modeling

During the 20th century, the development of ammonia reactors modeling has been important to predict temperature, pressure and concentrations variations inside converters. In 1943, Emmett and Kummer applied the original Temkin and Pyzhev equation (Equation (3.8)) to high-pressure synthesis. Moreover, a kinetic treatment of data was also performed (see Figure 3.8). They concluded that rate should be formulated in fugacity terms, and not partial pressure (from 300 to 1000 atm). However, the lack of experimental data and numerical limitations did not allow future developments (EMMETT and KUMMER, 1943).
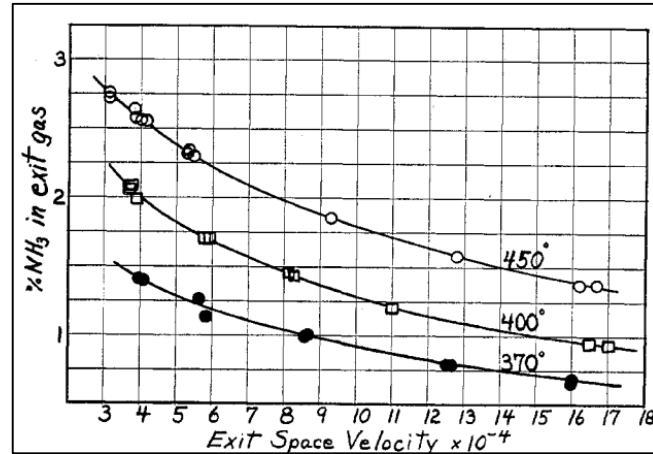
Figure 3.8. Kinetic treatment of ammonia reactions (Adapted from EMMETT and KUMMER, 1943).

In 1952, Annable made experimental research with catalysts and modeling in large-scale ammonia converters, obtaining kinetic constants. The work proposed optimal temperatures which gave maximum reaction rates in a certain design of catalyst bed (exposed in Figure 3.9). The Equation (3.8) was also used in modeling (ANNABLE, 1952).
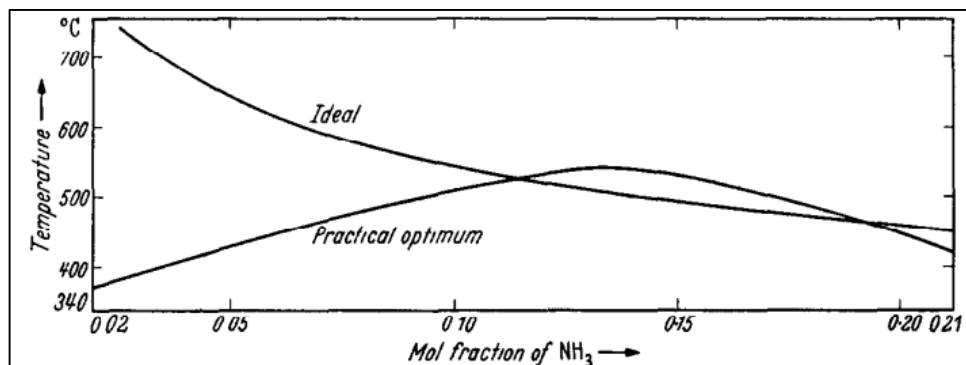
Figure 3.9. Temperature trajectories in ammonia reactor (ANNABLE, 1952).

Moreover, another important subject is the exothermic reaction's influence on converter stability. In 1953, van Heerden made a pioneering study to determine steady state multiplicity in autothermal reactors. In these reactors, the heat generated by the reaction follows an exponential tendency, while energy removed is linear. Therefore, multiple steady states can be achieved (VAN HEERDEN, 1953). In this mode, one can operate reactors in low conversions (safer) or in high conversions (with risks of heat generation). Figure 3.10 shows that only by varying the heat transfer coefficient, the number of possible steady states changed from 1 to 3.
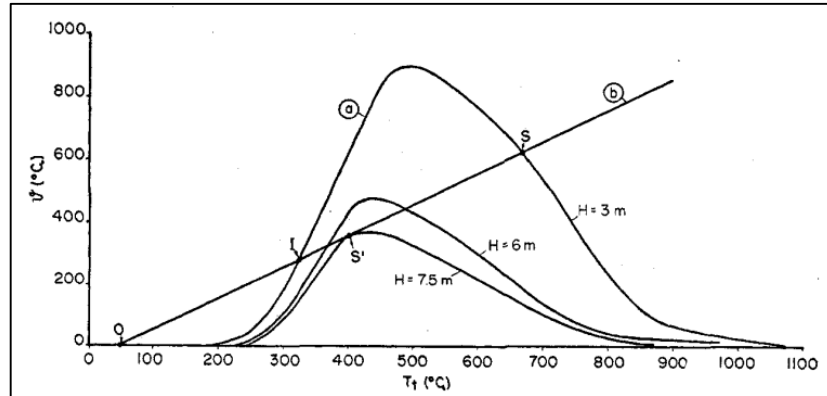
Figure 3.10. Multiple steady states in ammonia autothermal reactor varying *HUT* (VAN HEERDEN, 1953).

Between 1960 and 1990, most works focused on modeling ammonia converters. In 1965, Baddour and collaborators made a steady state simulation in a *TVA* reactor. A comparison was done with plant data. In simulation, the effects of space velocity, NH_3/inert contents in feed, reactor heat conductance, catalyst activity upon reactor stability, NH_3 production rate, and catalyst bed temperature profile were determined (BADDOUR et al., 1965). A comparison between their model and plant data is given in Figure 3.11.
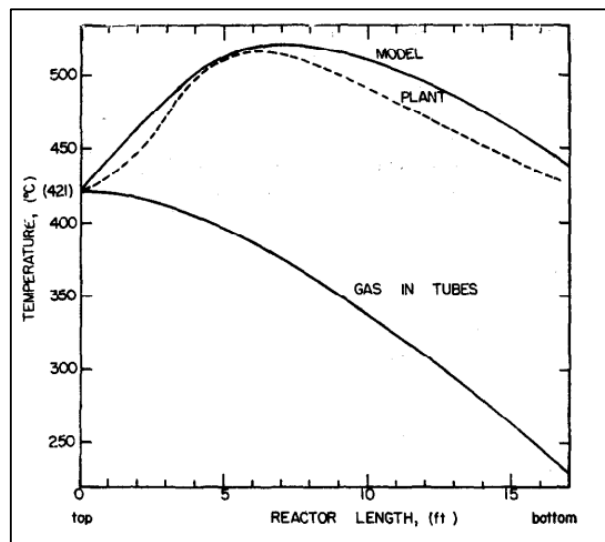
Figure 3.11. Comparison between one dimensional model and plant data (BADDOUR et al., 1965).

In 1965, Brian and collaborators made simulation of the same *TVA* reactor, now availing transient behavior. Their model predicted changes in catalyst temperature according to inlet temperature variations, as shown in Figure 3.12 (BRIAN et al., 1965). A numerical

resolution of a partial differential equations system was performed using Finite Differences Approximation.
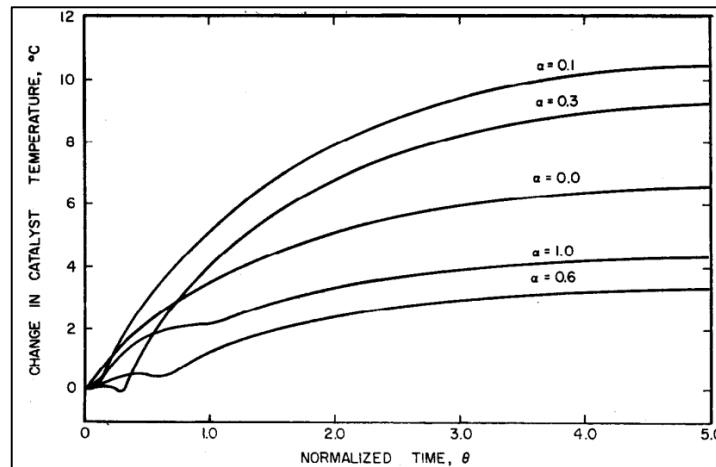
Figure 3.12. Catalyst temperature variations in time according to inlet temperature (BRIAN et al., 1965).

In 1968, J. M. Simon developed a PhD thesis studying quench converter behavior in both steady and transient modes. For transient behavior, a lumped parameter for quench converter was considered. The kinetic model used was described by Equation (3.16). An experimental correction factor for the reaction in catalyst particles was proposed. The model used the Beattie-Bridgeman *EoS* and proposed a methodology for quench points in the converter (SIMON, 1968).

In 1970, Murase and collaborators validated their model in an autothermal converter. The group used the Temkin-Pyzhev rate (Equation (3.8)) and supposed a constant density of gas. The model consisted of a one-dimensional differential equation system. The model presented good comparison with plant data, as seen in Figure 3.13. An optimal temperature trajectory along the reactor length was performed, applying Pontryagin's maximum principle (MURASE et al., 1970).
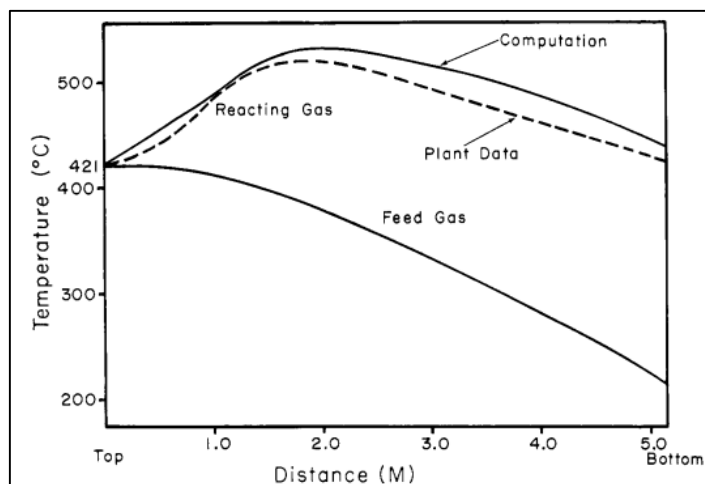
Figure 3.13. Comparison between temperatures profiles in an autothermal reactor (MURASE et al., 1970).

In 1975, Singh modeled quench type ammonia converters in a masters dissertation. Both axial and radial quench flow reactors were modeled. Furthermore, an optimization study was also done (SINGH, 1975). He concluded that pressure loss is crucial in ammonia converters. In the same year, Gaines developed a steady state model for a four-bed quench-type ammonia converter. The work used the *BWR* thermodynamic model. A simple method for reactor temperature control was proposed (GAINES, 1979).

In 1978, Singh developed a model for process simulation in ammonia plants. Not only ammonia converters were simulated, but also steam-hydrocarbon reformers and water gas-shift reactors (for hydrogen production). The effectiveness factor η was detailed by the solution of diffusion-reaction equations. This approach was different from the correlation used by Dyson and Simon, in 1968. However, there were difficulties in the numerical solution of differential equations. There were recommendations for heat transfer studies in primary and secondary reformers (SINGH, 1978).

In 1979, Singh and Saraf simulated both adiabatic and autothermal operations and compared them to plant data using a rigorous heterogeneous model. The modified rate presented by Dyson and Simon was used (Equation (3.16)). Furthermore, the work computed effectiveness factor solving diffusion-reaction equations instead of correlations (SINGH and SARAF, 1979).

The simulation of ammonia synthesis loop was also performed. In 1982, Reddy and Husain simulated an ammonia synthesis plant. Models for reactor, condenser, ejector and boiler were described. The vapor-liquid equilibrium was described according to Redlich-Kwong *EoS*.

Furthermore, heat transfer coefficients were also estimated (REDDY and HUSEIN, 1982). This work predicted the use of simulators in ammonia chemical plant's mass and heat balance.

In 1984, Rodrigues studied the kinetics of ammonia synthesis in a master dissertation. An experimental study was made to determine a reaction law. Even in steady state, there were differences of temperature and concentration in catalyst particles. Also, thermodynamic and transport properties were estimated for the reaction mixture (RODRIGUES, 1984).

In 1988, Elnashaie and collaborators simulated an interstage cooled ammonia reactor with a rigorous approach. Three adiabatic beds composed the converter system. The effectiveness factor η was calculated computing diffusion-reaction equations, as shown in Figure 3.14. For heat and mass balance, a variable step method was used, while for boundary value problems the orthogonal collocation method was proposed (about 3 points). Some difficulties were exposed especially in η computation. At the beginning of each reactor, 7 collocation points needed to be used (diffusion limitations due to high nonlinearity), causing difficulties in integration. An optimization analysis was also performed. They concluded that their model was reliable (ELNASHAIE et al., 1988).
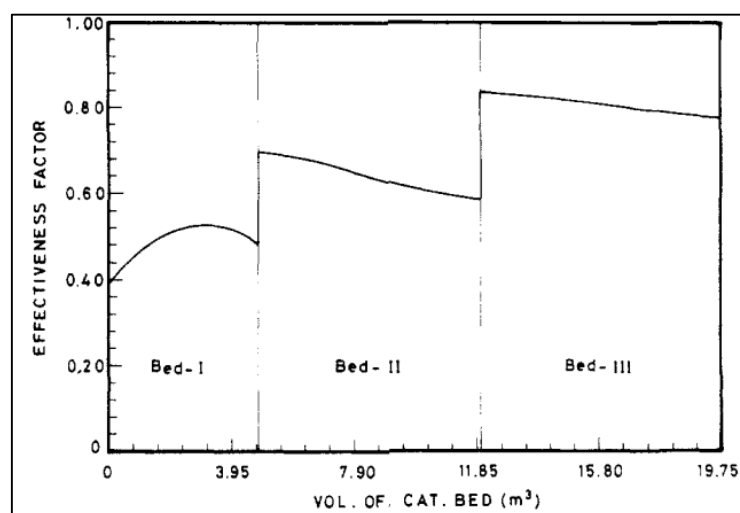
Figure 3.14. Effectiveness factor profile using orthogonal collocation method in ammonia converters (ELNASHAIE et al., 1988).

From 1990 to 2016, many works focused on the optimization of ammonia converters, with or without process simulators. In 1992, Reis simulated a radial quench converter in an ammonia plant using *SRK-EoS* to predict thermodynamic properties in a PhD thesis. The study was made using the Hysim® simulator. A parametric study was proposed to

verify influences at the reactor exit. However, the parametric study did not bring significant improvements to ammonia production. The model showed reliability, though. (REIS, 1992).

In 1993, Morud and Skogestad studied the temperature oscillation in an industrial ammonia plant converter. A root locus for the reaction system and a linearized model for the reactor were detailed. The instability occurred due to a pair of conjugate pole crosses. An oscillation is shown at Figure 3.15. They concluded that a suitable control system was capable of reaching a steady-state (MORUD and SKOGESTAD, 1993). A great achievement of this work was the control for an ammonia reactor.
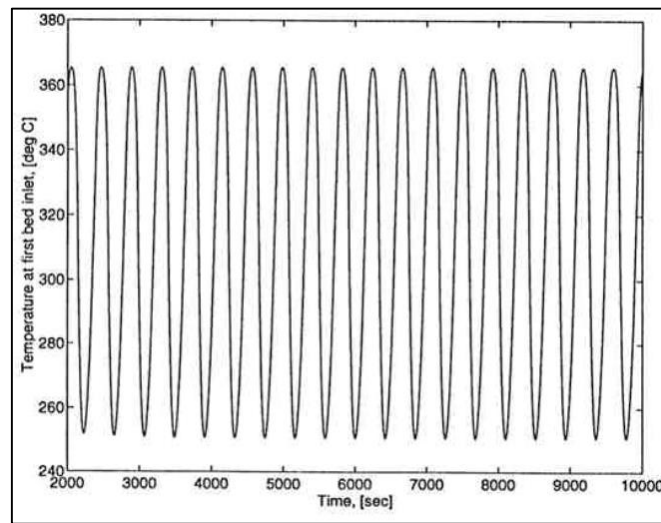
Figure 3.15. Temperature oscillations in an adiabatic reactor (MORUD and SKOGESTAD, 1993).

In 1997, Upreti and Deb made optimization in an autothermal ammonia reactor using genetic algorithms. The yields for an ammonia plant were studied in a wide range of inlet temperatures in the reactor. As inlet temperature rose, the yield increased. However, beyond 706 K, the simulation was not feasible, as seen in Figure 3.16. They concluded that genetic algorithms can be used in the modeling of reactors, even in the presence of inexact information for reactor performance (UPRETI and DEB, 1997).
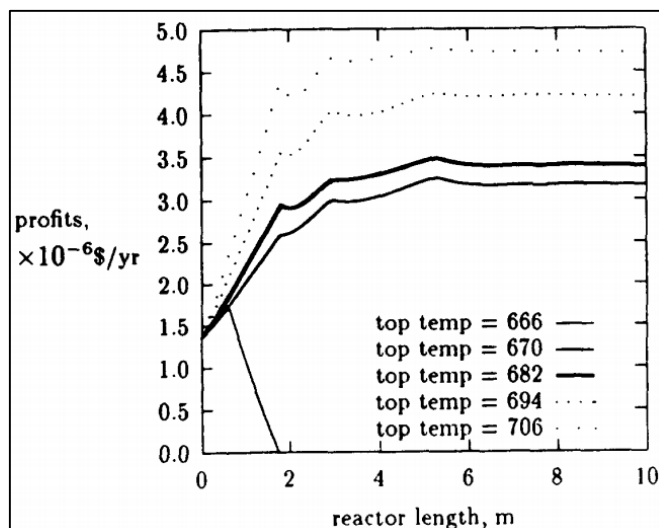
Figure 3.16. Profit for ammonia reactor at many top temperatures (UPRETI and DEB, 1997).

In 2005, Babu and Angira used an NAG subroutine in Matlab® to determine the optimal reactor length of an ammonia synthesis reactor. They reported errors in previous formulation by Upreti and Deb (BABU and ANGIRA, 2005).

In 2010, Holter proposed in a masters dissertation the feedforward control for an ammonia reactor. Reactor heat exchangers and quench points were modeled. The model presented high non-linearity, due to the reaction rate. He concluded that the system could not be stabilized with a PI-controller. A derivative term must be included in order to stabilize the ammonia reactor (HOLTER, 2010).

In 2012, Esturilio also proposed a control for a radial ammonia converter (Haldor-Topsøe S-200) in a masters dissertation. The model was developed in Matlab® and it was validated with plant data. For thermodynamic properties, the *SRK-EoS* was used. A predictive control was also formulated, showing reliable results with perturbations (ESTURILIO, 2012).

In 2014, Azarhoosh and collaborators performed an optimization in a horizontal ammonia synthesis reactor. The model was validated with industrial data and an optimization with a genetic algorithm was made. Moreover, a sensitivity analysis was also performed. The model proved reliable in predicting variations in ammonia reactors (AZARHOOSH et al., 2014).

In 2016, Carvalho made an analysis of an ammonia reactor in the EMSO simulator. The *PR-EoS* was implemented to compute the thermodynamic properties. The finite volume technique was used. The model was calibrated and a sensitivity analysis was performed (CARVALHO, 2016).

Even with numerous studies of ammonia reactors, some points can be improved. In many rate expressions, there is use of chemical activities. However, they are not calculated according to a compositional model (Table 3.1). In other words, a substance is not influenced by the molar fraction variation of other components in the mixture. Moreover, although industrial reactors operate at small residence times, there are still some differences of concentration in the boundary layer. Therefore, a different alternative for process simulators can be developed.

4 METHODOLOGY

In engineering of chemical reactions, it is necessary to understand the calculation methods. After all, the field of study involves multiple subjects, such as numerical methods, heat and mass transfer, and so on. In this section, the main algorithms for each part of reactor modeling are explained. First, all thermodynamic models used are described. Furthermore, the calculations of the main thermodynamic and transport properties are explained. After that, the mass, energy and momentum balances of adiabatic and autothermal models are detailed, as well as the kinetic correction factor η. Once the reactor models were defined, the boundary layer estimations were made. It helped to decide if the mass transfer resistance outside catalyst was significant. Lastly, the two numerical methods for solving ODE systems were detailed: 4th Order Runge-Kutta (with fixed step-size) and 4th and 5th Order Runge-Kutta-Fehlberg (with variable step size and error control strategy).

4.1 Thermodynamic Modeling

The prediction of thermodynamic and transport properties is important in modeling. One example is density variation along the reactor. In this section, thermodynamic methods are explained with expressions and flowsheets.

4.1.1 Cubic Equations of State

Cubic *EoS* are classical models for high-pressure conditions. From the thermodynamic point of view, high pressure refers to values that present a significant effect on the thermodynamic and transport properties of certain phases. The great success of cubic *EoS* lies in the ability of fast calculations and accurate representations of low and high-pressure *VLE* for mixtures of hydrocarbons and hydrocarbons with gases (KONTOGEORGIS and FOLAS, 2010). Two *EoS* models that are very used are Peng Robinson and Soave-Redlich-Kwong.

The most used cubic *EoS* are *PR* and *SRK*. The main hypothesis is that pressure is composed of a repulsive term P_{Rep} and an attractive term P_{Att} and, as shown in Equation (4.1).

$$P = P_{Rep} + P_{Att} \tag{4.1}$$

The repulsive term P_{Rep} corrects finite volume of molecules. Attractive term P_{Att} accounts for intermolecular forces similarly. Moreover, P_{Att} varies according to each cubic *EoS*. A general format for *PR* and *SRK* cubic *EoS* is given in Equation (4.2).

$$P = \frac{RT}{v - b} - \frac{a(T)}{(v + \delta_1.b).(v + \delta_2.b)} \qquad (4.2)$$

In the equation above, P is pressure $[Pa]$, R denotes ideal gas constant $[Pa.m^3/mol.K]$, T is system temperature $[K]$, v is molar volume $[m^3/mol]$, b is covolume term $[m^3/mol]$, $a(T)$ is a function of temperature $[m^3/mol]$ and δ_1 and δ_2 are coefficients which vary according to *EoS*. These coefficients are shown in Table 4.1.

Table 4.1. Coefficients δ_1 and δ_2 for general formulation of cubic *EoS* (NICHITA, 2006).

EoS	δ_1	δ_2
PR	$1 + \sqrt{2}$	$1 - \sqrt{2}$
SRK	0	1

One can replace δ_1 and δ_2 coefficients. It results in *PR* and *SRK EoS*, expressed in relations (4.3) and (4.4) respectively.

$$P = \frac{RT}{v - b} - \frac{a(T)}{v(v + b) + b(v - b)} \qquad (4.3)$$

$$P = \frac{RT}{v - b} - \frac{a(T)}{v(v + b)} \qquad (4.4)$$

Observing the equations above, some differences are noted in denominators of *PR* and *SRK* models. The liquid volume predicted by *SRK* is usually higher than in experimental data. It occurs especially in high ω deviations. After all, in the liquid phase, other forces of attraction and repulsion must be accounted for. Therefore, Peng and Robinson introduced the term $b(v - b)$ in denominator of Equation (4.3), which improved the representation of the attractive pressure forces, and in consequence, the ability of the equation to predict liquid densities (LOPEZ-ECHEVERRY et al., 2017).

4.1.1.1 Compressibility Factor Calculation

The coefficients $a(T)$ and b in Equation (4.2) can be replaced according to relations (4.5) and (4.6) for mixtures. The variables A_{mix} and B_{mix} are usually calculated to compute the compressibility factor Z_{mix}.

$$A_{mix} = \frac{a.p}{(R.T)^2} \qquad (4.5)$$

$$B_{mix} = \frac{b.p}{R.T} \tag{4.6}$$

For real gases, the compressibility factor Z is a correction of volume, as expressed in Equation (4.7).

$$P.v = Z.R.T \tag{4.7}$$

In relation to the above, P is system pressure $[Pa]$, v is molar volume $[m^3/mol]$, Z is compressibility factor $[-]$, R is ideal gas constant $[Pa.m^3/(mol.K)]$ and T is temperature $[K]$. If $Z = 1$, the gas is considered ideal. Therefore, in cubic EoS, the main calculation for density and volume prediction depends on Z. For a gas mixture, the calculation of mixture compressibility factor Z_{mix} is obtained in Equation (4.8).

$$Z_{mix}^3 + p.Z_{mix}^2 + q.Z_{mix} + r = 0 \tag{4.8}$$

In relation to the above, p, q and r are coefficients which depend on EoS type, composition, temperature $[K]$ and pressure $[Pa]$ of system. They are summarized in Table 4.2 and Table 4.3. At each iteration, the values for Z_{mix} are calculated using the Newton-Raphson method (more details in APPENDIX).

Table 4.2. Auxiliary coefficients for Equation (4.8) (NICHITA, 2006).

EoS	s	t	u	w
PR/SRK	$\delta_1 + \delta_2 - 1$	$\delta_1 + \delta_2$	$\delta_1.\delta_2$	$B_{mix} + 1$

Table 4.3. Main constants for Equation (4.8) (NICHITA, 2006).

EoS	p	q	r
PR/SRK	$s.B_{mix} - 1$	$A_{mix} + u.B_{mix}^2 - t.B_{mix}.w$	$-\left(A_{mix}.B_{mix} + u.B_{mix}^2.w\right)$

The coefficients A_{mix} and B_{mix} are calculated according to correction α_i, which depends on reduced temperature T_{r_i} and pressure P_{r_i} of components. The reduced factors specify the state of aggregation of a substance. For component i in the mixture, these relations were given in Equations (4.9) and (4.10).

$$T_{r_i} = \frac{T_{c_i}}{T} \tag{4.9}$$

$$P_{r_i} = \frac{P_{c_i}}{P} \tag{4.10}$$

In Equations (4.9) and (4.10), T_{c_i} represents the critical temperature of substance i [K] and T is system temperature [K]. For pressure, P_{c_i} denotes critical pressure of substance i [Pa] and P is system pressure [Pa]. Therefore, EoS tries to compute all substances according to its reduced properties, making the model robust. Critical properties can be found in literature.

Acentric factor ω_i also has an influence on EoS. If the molecule is non-spherical, ω_i deviates from zero. The corrections for ω_i are shown in Equations (4.11) and (4.12).

$$f(\omega_i) = (0.37464 + 1.54226\omega_i - 0.26992{\omega_i}^2) \; if \; (\omega_i < 0.5215) \tag{4.11}$$

$$f(\omega_i) = (0.3796 + 1.485\omega_i - 0.1644{\omega_i}^2 + 0.0166{\omega_i}^3) \; if \; (\omega_i > 0.5215) \tag{4.12}$$

In ammonia synthesis, acentric factors are not high, so normally Equation (4.11) is used. In addition, correction with temperature and acentric factor ω_i are resumed in α_i function in relation (4.13).

$$\alpha_i = \left[1 + f(\omega_i).\left(1 - \sqrt{T_{ri}}\right)\right]^2 \tag{4.13}$$

Once previous calculations are computed, individual factors A_i, A_{ij}, and B_i can be calculated in the expressions below. These factors will help to compute A_{mix} and B_{mix} for each model chosen, as shown in expressions (4.14) to (4.16).

$$A_i = \Omega_a.\left(\frac{P_r}{{T_r}^2}\right)_i . \alpha_i \tag{4.14}$$

$$A_{ij} = \left(1 - k_{ij}\right).\sqrt{A_{ii}A_{jj}} \tag{4.15}$$

$$B_i = \Omega_b.\left(\frac{P_r}{T_r}\right)_i \tag{4.16}$$

In relations (4.14) to (4.16), B_i is a vector (with dimension as component number N_{comp}) and A_{ij} is a square matrix ($N_{comp} \; x \; N_{comp}$). The van der Waals mixing rules are used to compute energy A_{mix} and volume B_{mix}, as given in Equations (4.17) and (4.18).

$$A_{mix} = \sum_{i=1}^{N_{comp}} \sum_{j=1}^{N_{comp}} y_i \cdot y_j \cdot A_{ij} \tag{4.17}$$

$$B_{mix} = \sum_{j=1}^{N_{comp}} y_j \cdot B_j \tag{4.18}$$

Factors Ω_a and Ω_b are constants. Both depend on the EoS chosen, as denoted in Table 4.4.

Table 4.4. Coefficients Ω_a and Ω_b for cubic *EoS* (MICHELSEN, 1986).

EoS	Ω_a	Ω_b
PR	0.45724	0.07780
SRK	0.42747	0.08664

Moreover, k_{ij} is the binary interaction parameter. It can be tabulated (from experimental equilibria), set to zero or computed as Equation (4.19) (PEDERSEN, 2014). Again, a k_{ij} square matrix with dimensions (N_{comp} x N_{comp}) is computed. In Equation (4.19), T_{c_i} is critical temperature of i component [K] and Z_{c_i} is the critical compressibility factor of i component [$-$].

$$k_{ij} = 1 - \left[2 \cdot \sqrt{\left(\frac{T_{c_i} \cdot T_{c_j}}{T_{c_i} + T_{c_j}} \right)} \right]^{\left(\frac{Z_{c_i} + Z_{c_j}}{2} \right)} \tag{4.19}$$

In Figure 4.1, there is a flowsheet for Z_{mix} calculation. It depends on temperature, pressure and composition at each step of the reactor.
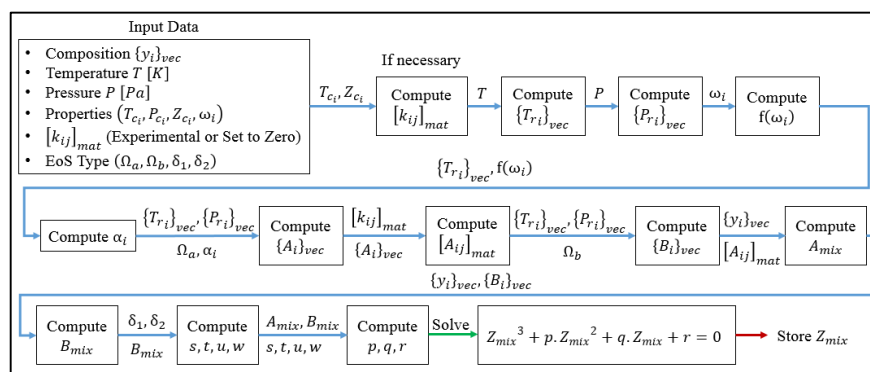
Figure 4.1. Flowchart for Z_{mix} calculation.

In the next situations, Figure 4.1 will be named as "Compute Z_{mix}".

4.1.1.2 Molar Volume and Density Calculation

Volume and density are the properties that present most variations along the ammonia reactor. As temperature increases, density rises because flow is compressible. As pressure increases, density also grows, because gas molecules approximate to one another. Once Z_{mix} is calculated by an appropriated method, mixture molar volume v $[m^3/mol]$ is obtained by real gas law, as presented in Equations (4.20) and (4.21).

$$p.v = Z_{mix}.R.T \tag{4.20}$$

$$v = \frac{Z_{mix}.R.T}{p} \tag{4.21}$$

However, in high-pressure situations, intermolecular forces take important roles. These forces change v, even with Z_{mix} calculation in cubic *EoS*. Therefore, an additional technique must be used to account for v, now computing these new interactions.

In the volume translation technique (or volume shift), molar volume is calculated according to a correction given in Equation (4.22). This alteration is valid both in liquid and gas phases. In liquid phases, volume shift is useful, because cubic *EoS* presents different volumes compared to experimental data. In the gas phase, the adjustment is smaller than in the liquid phase. Compared with the high molar volume of gases at low and moderate pressures, the volume correction value is relatively low (DANESH, 1998). However, this correction is more effective at high pressures (EBRAHIMI et al., 2017), which is the case of ammonia synthesis.

$$v = v_{CEoS} - \sum_{i=1}^{N_{comp}} c_i \tag{4.22}$$

In Equation (4.22), v_{CEoS} represents molar volume determined from cubic *EoS* $[m^3/mol]$ while c_i is the correction factor $[m^3/mol]$ for component i. This relation is valid for single and multi-component situations. Each EoS presents different formulations for coefficient c, as presented in Table 4.5.

In Table 4.5, Z_{RA_i} is the Rackett compressibility factor for each component. Z_{RA_i} represents a contribution of acentric factor ω_i for each substance, as seen in Equation (4.23).

$$Z_{RA_i} = 0.29506 - 0.08775.\omega_i \tag{4.23}$$

Table 4.5. Coefficient c_i (volume shift) for each EoS (PENÉLOUZ and FRÉZE, 1982) and (EBRAHIMI et al., 2017).

EoS	$c_i \; [m^3/mol]$
PR	$0.40768.\left(\dfrac{R.T_{c_i}}{P_{c_i}}\right).\left(0.29441 - Z_{RA_i}\right)$
SRK	$0.50033.\left(\dfrac{R.T_{c_i}}{P_{c_i}}\right).\left(0.25969 - Z_{RA_i}\right)$

After corrections, mixture molar density $\rho_{molar} \; [mol/m^3]$ is computed with inverse of corrected molar volume $[m^3/mol]$, as described in Equation (4.24).

$$\rho_{molar} = \frac{1}{v} \tag{4.24}$$

The density in mass units can also be determined. Only the mixture molar weight $MM_{mix} \; [kg/mol]$ is necessary. Therefore, mass density $\rho_{mass} \; [kg/m^3]$ is obtained and mass volume is calculated as in Equation (4.24).

$$MM_{mix} = \sum_{i=1}^{N_c} y_i.MM_i \tag{4.25}$$

$$\rho_{mass} = \rho_{molar}.MM_{mix} \tag{4.26}$$

Lastly, the new value of Z_{mix} is calculated again in Equation (4.20). A flowchart for molar volume and density calculation is described in Figure 4.2. There is an option to use volume shift.
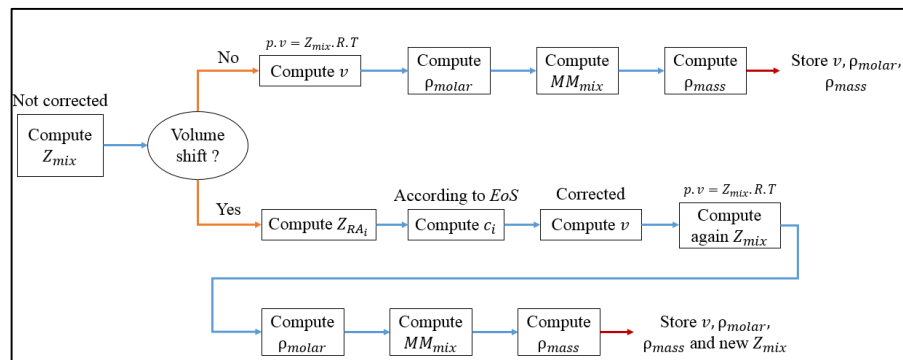
Figure 4.2. Flowchart for v, ρ_{molar} and ρ_{mass} calculation (with or without volume shift).

4.1.1.3 Fugacity Coefficient and Fugacity Calculation

For ammonia reactions, it is necessary to predict chemical activities and fugacities (Equations (3.8) from (3.22)). Especially under higher pressures, fugacities correct partial pressure deviations. Moreover, in *HPHT* conditions, the Lewis-Randall rule is not allowed.

Fugacity coefficients $\hat{\varphi}_i^g$ are necessary to compute fugacities $\hat{f}_i^g$ in gas mixtures. In NH_3 reactor, there is no liquid phase. For *PR* and *SRK* cubic *EoS*, the formulation for $\hat{\varphi}_i^g$ calculation is described in Equation (4.27).

$$ln(\hat{\phi}_i^g) = (Z_{mix} - 1).\left(\frac{B_i}{B_{mix}}\right) - ln(Z_{mix} - B_{mix}) - \left(\frac{A_{mix}}{\Delta. B_{mix}}\right).\tau_i.ln(\xi) \tag{4.27}$$

In Equation (4.27) $\hat{\varphi}_i^g$ is the fugacity coefficient $[-]$. Moreover, Δ, ψ_i, τ_i and ξ are coefficients for Equation (4.27), summarized in Table 4.6. δ_1 and δ_2 were given in Table 4.1.

Table 4.6. Auxiliary coefficients for equation (4.27) (NICHITA, 2006).

Δ	ψ_i	τ_i	ξ
$(\delta_1 - \delta_2)$	$\sum_{j=1}^{N_{comp}} y_j.A_{ij}$	$\left(\frac{2.\psi_i}{A_{mix}} - \frac{B_i}{B_{mix}}\right)$	$\left(\frac{Z_{mix} + \delta_1.B_{mix}}{Z_{mix} + \delta_2.B_{mix}}\right)$

If a gas is ideal, $\hat{\varphi}_i^g$ is one. However, if the gas is not in ideal conditions, $\hat{\varphi}_i^g$ will differ from one. Once $\hat{\varphi}_i^g$ is computed according to each *EoS*, fugacity can be calculated, as expressed in relation (4.28).

$$\hat{f}_i^g = \hat{\varphi}_i^g.y_i.P \tag{4.28}$$

In the equation above, $\hat{f}_i^g$ is fugacity of a component in mixture $[Pa]$ and y_i is the molar fraction of i component $[-]$. In addition, both values of $\hat{\varphi}_i^g$ and $\hat{f}_i^g$ are changed with volume shift, because this method alters Z_{mix}. The procedure for calculation is described in Figure 4.3.
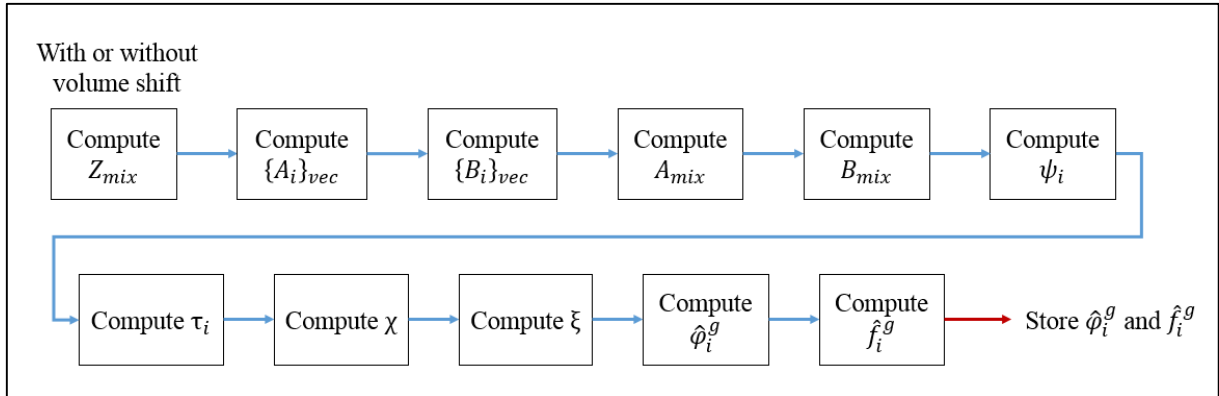
Figure 4.3. Flowchart for $\hat{\varphi}_i^g$ and $\hat{f}_i^g$ calculation (with or without volume shift).

4.1.1.4 Chemical Activity Calculation

Chemical activity a_i $[-]$ is determined using Equation (4.29). It can be noted in Equation (4.29) that it depends on the $\hat{\varphi}_i^g$ and $\hat{f}_i^g$ calculation.

$$a_i = \frac{\hat{\varphi}_i^g \cdot y_i \cdot P}{P_{ref}} = \frac{\hat{f}_i^g}{P_{ref}} \tag{4.29}$$

In relation to the above, P_{ref} is reference pressure, usually taken as 101325 Pa or 1 atm.

4.1.1.5 Enthalpy Calculation

The enthalpy H is the measure of energy in a system. Its effect includes the internal energy U, pressure p and volume v of a system, as given in Equation (4.30).

$$H = U + p \cdot v \tag{4.30}$$

In real situations, the enthalpy of a gas H_{mix} $[J/mol]$ is a sum of two contributions: ideal H_{mix}^{ig} $[J/mol]$ and residual H_{mix}^{res} $[J/mol]$, as described in Equation (4.31).

$$H_{mix} = H_{mix}^{ig} + H_{mix}^{res} \tag{4.31}$$

H_{mix}^{ig} is computed using polynomial correlations (more details in APPENDIX Section). A general approach is given in Equation (4.32).

$$H_{mix}^{ig} = \int_{T_{ref}}^{T} \left[C_p^{ig}(T) \right]_{mix} dT = \int_{T_{ref}}^{T} \left[\sum_{i=1}^{N_{comp}} y_i \cdot C_{p\ i}^{ig}(T) \right] dT \tag{4.32}$$

On the other hand, H_{mix}^{res} is a correction using *EoS*. In ideal gas situations, the term H_{mix}^{res} is zero. For cubic EoS, a general formulation for H_{mix}^{res} is given relating to (4.33). The deduction of this equation is in APPENDIX Section.

$$H_{mix}^{res} = R.T.(Z_{mix} - 1) + \left[\frac{T.\left(\frac{da}{dT}\right) - a}{b.(\delta_1 - \delta_2)}\right].ln\left(\frac{Z_{mix} + \delta_1.B_{mix}}{Z_{mix} + \delta_2.B_{mix}}\right) \tag{4.33}$$

In the equation above, $\left(\frac{da}{dT}\right)$ is the first derivative of $a(T)$. A flowchart for residual enthalpy calculation is given in Figure 4.4.
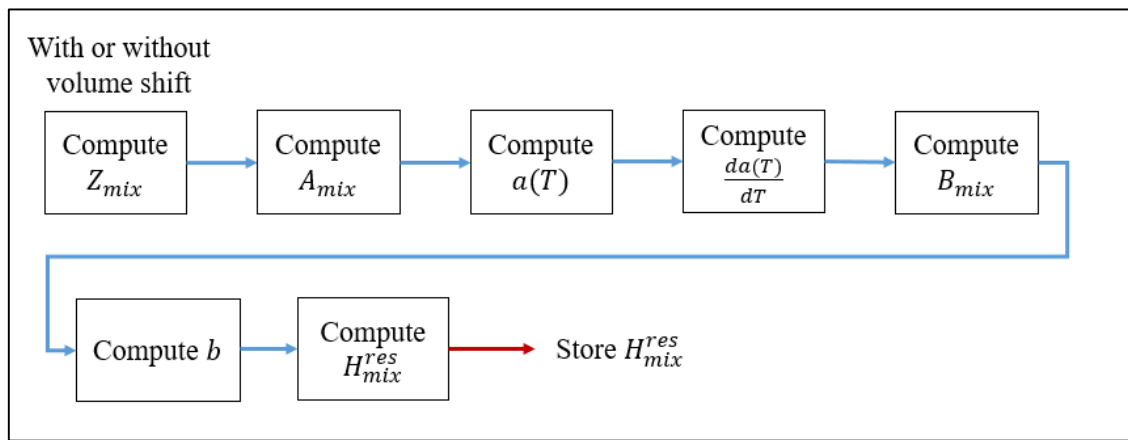
Figure 4.4. Flowchart for residual enthalpy H_{mix}^{res} calculation.

It can be seen in Figure 4.5 that H_{mix}^{ig} is a correction for low pressures and H_{mix}^{res} is a correction for high pressures.
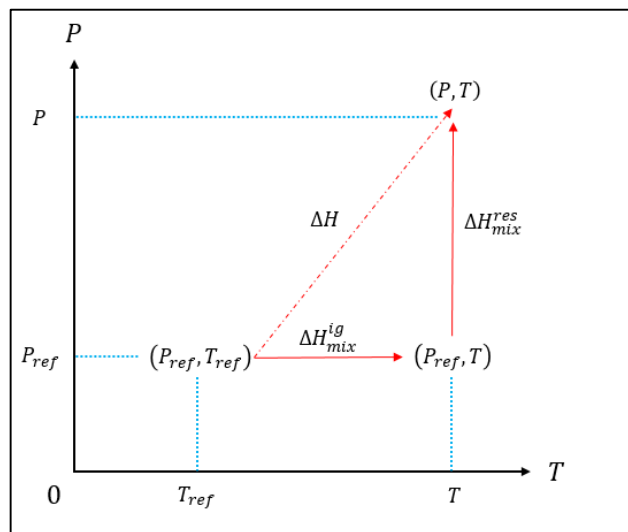
Figure 4.5. Path for enthalpy variation using ideal and residual contributions.

The formulations for H_{mix}^{res} *PR* and *SRK EoS* are given in Table 4.7

Table 4.7. Formulation for residual enthalpy in *PR* and *SRK EoS*.

EoS	H_{mix}^{res} (J/mol)
PR	$R.T.(Z_{mix} - 1) + \left[\dfrac{T.\left(\frac{da}{dT}\right) - a}{2\sqrt{2}b}\right].ln\left[\dfrac{Z_{mix} + (1 + \sqrt{2}).B_{mix}}{Z_{mix} + (1 - \sqrt{2}).B_{mix}}\right]$
SRK	$R.T.(Z_{mix} - 1) + \left[\dfrac{T.\left(\frac{da}{dT}\right) - a}{b}\right].ln\left(\dfrac{Z_{mix} + B_{mix}}{Z_{mix}}\right)$

Another important aspect of enthalpy is the reference state. Usually it is taken as 298.15 K and 1 atm in our calculations (same as Aspen). However, the enthalpy zero is also a significant point. In the Aspen simulator, elements at their most usual state at T_{ref} and P_{ref} define zero enthalpy, as described in Figure 4.6.
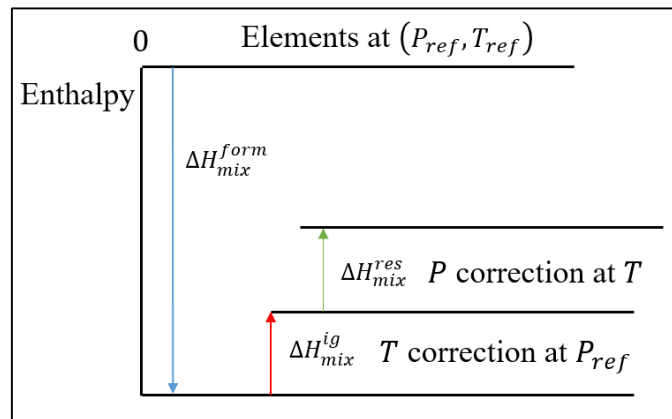
Figure 4.6. Pattern for enthalpy zero using enthalpy of formation.

Therefore, when comparing two simulators, enthalpy of formation must be accounted for (changing Equation (4.31)), as represented in Equation (4.34). In our calculations, we did not account for this enthalpy.

$$H_{mix} = H_{mix}^{form} + H_{mix}^{ig} + H_{mix}^{res} \tag{4.34}$$

Enthalpy of mixture can be displayed in molar or mass units. We can use mixture molar weight in Equation (4.25) to conversion. Therefore, enthalpy will be in mass units, as given in Equation (4.35).

$$H_{mix}^{mass} = \frac{H_{mix}^{molar}}{MM_{mix}} \tag{4.35}$$

In relation to the above, H_{mix}^{mass} in enthalpy in mass units $[J/kg]$, H_{mix}^{molar} is enthalpy computed by equation (4.34) $[J/mol]$ and MM_{mix} is mixture molar weight $[kg/mol]$.

4.1.1.6 Heat capacity C_p Calculation

Heat capacity C_p is important for energy balance equations, because it is normally a denominator. Due to high-pressure conditions, heat capacity in real gases is determined using a correction in ideal gas formulation. In elevate pressures; the mean free path between gas molecules is decreased, modifying heat capacity values. For a mixture, $C_{p_{mix}}$ $[J/(mol.K)]$ is described by Equation (4.36), with an ideal and a residual contribution.

$$C_{p_{mix}} = C_p^{ig}{}_{mix} + C_p^{res}{}_{mix} \tag{4.36}$$

Ideal gas heat capacity $C_p^{ig}{}_{mix}$ is computed using a similar correlation to enthalpy (more details in APPENDIX) in Equation (4.37).

$$C_p^{ig}{}_{mix} = \sum_{i=1}^{N_{comp}} y_i \cdot C_p^{ig}{}_i(T) \tag{4.37}$$

The residual contribution $C_p^{res}{}_{mix}$ $[J/(mol.K)]$ depends on cubic EoS used (δ_1 and δ_2). Hence $C_p^{res}{}_{mix}$ is influenced by H_{mix}^{res}, the second derivative of $a(T)$ must be computed, as detailed in Equations (4.38) to (4.42). A more complete approach to $C_p^{res}{}_{mix}$ and derivatives $\left(\frac{\partial Z_{mix}}{\partial T}\right)_P$ and $\left(\frac{dB_{mix}}{dT}\right)$ is described in APPENDIX.

$$C_p^{res}{}_{mix} = C_p^{res}{}_{mix1} + C_p^{res}{}_{mix2} + \left(C_p^{res}{}_{mix3} \cdot C_p^{res}{}_{mix4}\right) \tag{4.38}$$

$$C_p^{res}{}_{mix1} = R \cdot \left[T \cdot \left(\frac{\partial Z_{mix}}{\partial T}\right)_P + Z_{mix} - 1\right] \tag{4.39}$$

$$C_p^{res}{}_{mix2} = \left[ln\left(\frac{Z_{mix} + \delta_1 \cdot B_{mix}}{Z_{mix} + \delta_2 \cdot B_{mix}}\right)\right] \cdot \left[\frac{1}{b \cdot (\delta_1 - \delta_2)}\right] \cdot \left(T \cdot \frac{d^2a}{dT^2}\right) \tag{4.40}$$

$$C_p^{res}{}_{mix3} = \left[\frac{(\delta_1 - \delta_2)}{(Z_{mix} + \delta_1 \cdot B_{mix}) \cdot (Z_{mix} + \delta_2 \cdot B_{mix})}\right] \tag{4.41}$$

$$C_p^{res}{}_{mix4} = \left[Z_{mix} \cdot \left(\frac{dB_{mix}}{dT}\right) + B_{mix} \cdot \left(\frac{\partial Z_{mix}}{\partial T}\right)_P\right] \tag{4.42}$$

A flowchart for $C_p^{res}{}_{mix}$ in molar units determination is given in Figure 4.7.
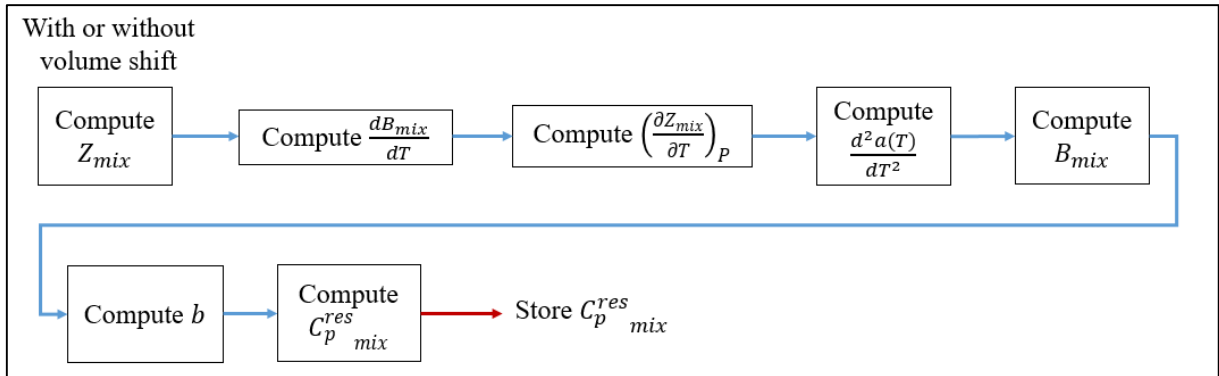
Figure 4.7. Flowchart for residual heat capacity $C_p^{res}{}_{mix}$ calculation.

The heat capacity of a mixture can also be computed in mass units $[J/(kg.K)]$, as well as enthalpy. It is described in Equation (4.43).

$$C_p^{mass}{}_{mix} = \frac{C_p^{molar}{}_{mix}}{MM_{mix}} \tag{4.43}$$

4.1.1.7 Internal Energy Calculation

The internal energy is used to compute heat capacity $C_{v\,mix}$. Moreover, in energy balances the enthalpy will be used, because it accounts for the effect of pressure and volume too. The internal energy U_{mix} is a sum of the ideal contribution U_{mix}^{ig} and residual term U_{mix}^{res}, as described in expression (4.44).

$$U_{mix} = U_{mix}^{ig} + U_{mix}^{res} \tag{4.44}$$

The ideal internal energy U_{mix}^{ig} $[J/mol]$ depends on enthalpy H_{mix}^{ig} $[J/mol]$, as given in Equation (4.45). The polynomial expressions for ideal calculations are given in the APPENDIX.

$$U_{mix}^{ig} = \int_{T_{ref}}^{T} [C_p^{ig}(T) - R]_{mix} dT = \int_{T_{ref}}^{T} [C_v^{ig}(T)]_{mix} dT = \int_{T_{ref}}^{T} \left[\sum_{i=1}^{N_{comp}} y_i . C_v^{ig}{}_i(T) \right] dT \tag{4.45}$$

The residual contribution U_{mix}^{res} $[J/mol]$ is computed according to relation (4.46).

$$U_{mix}^{res} = \left[\frac{T.\left(\frac{da}{dT}\right) - a}{b.(\delta_1 - \delta_2)}\right].ln\left(\frac{Z_{mix} + \delta_1.B_{mix}}{Z_{mix} + \delta_2.B_{mix}}\right) \tag{4.46}$$

The procedure for U_{mix}^{res} calculation is analogous to H_{mix}^{res}, as given in Figure 4.8. The only difference is in term $R.T.(Z_{mix} - 1)$ in H_{mix}^{res}.
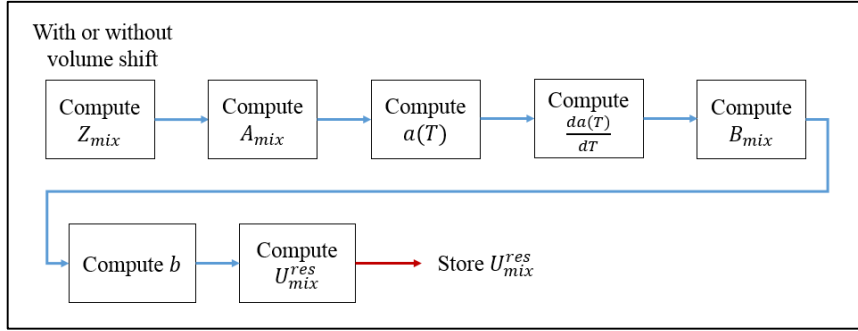
Figure 4.8. Flowchart for residual U_{mix}^{res} calculation.

The formulation for U_{mix}^{res} PR and SRK EoS are given in Table 4.8.

Table 4.8. Formulation for residual internal energy in PR and SRK EoS.

EoS	U_{mix}^{res} (J/mol)
PR	$\left[\dfrac{T.\left(\frac{da}{dT}\right) - a}{2\sqrt{2}b}\right].ln\left[\dfrac{Z_{mix} + (1+\sqrt{2}).B_{mix}}{Z_{mix} + (1-\sqrt{2}).B_{mix}}\right]$
SRK	$\left[\dfrac{T.\left(\frac{da}{dT}\right) - a}{b}\right].ln\left(\dfrac{Z_{mix} + B_{mix}}{Z_{mix}}\right)$

Lastly, we can also compute internal energy U_{mix}^{mass} in mass units $[J/kg]$, as expressed in Equation (4.47).

$$U_{mix}^{mass} = \frac{U_{mix}^{molar}}{MM_{mix}} \tag{4.47}$$

4.1.1.8 Heat capacity C$_v$ Calculation

Heat capacity C_v does not appear in the energy balance. However, it is a great measure of the lack of ideality of a gas. In ideal gas situations, it is demonstrated that the difference between $C_p^{ig}{}_{mix}$ and $C_v^{ig}{}_{mix}$ is equal to R (Equation (4.48)).

$$C_p^{ig}{}_{mix} - C_v^{ig}{}_{mix} = R \tag{4.48}$$

There is also an ideal and a residual contribution, as expressed in Equation (4.49).

$$C_{v\,mix} = C_v^{ig}{}_{mix} + C_v^{res}{}_{mix} \tag{4.49}$$

In real gas conditions, this difference is not equal to R, though. Therefore, one must compute $C_{v\,mix}$ with its ideal and residual contributions. Ideal gas heat capacity $C_v^{ig}{}_{mix}$ is computed using a similar correlation to internal energy U_{mix}^{ig}, as given in relation (4.50) (more details in APPENDIX).

$$C_v^{ig}{}_{mix} = \sum_{i=1}^{N_{comp}} y_i \cdot C_v^{ig}{}_i(T) \tag{4.50}$$

The residual contribution $C_v^{res}{}_{mix}$ is deduced similarly to $C_p^{res}{}_{mix}$, which is described in Equation (4.38). Equations (4.38) and (4.51) prove that the difference between $C_p^{ig}{}_{mix}$ and $C_v^{ig}{}_{mix}$ is more complex in real gas situations. Details can be found in the APPENDIX.

$$C_v^{res}{}_{mix} = ln\left(\frac{Z_{mix} + \delta_1 \cdot B_{mix}}{Z_{mix} + \delta_2 \cdot B_{mix}}\right) \cdot \left[\frac{T \cdot \left(\frac{d^2 a}{dT^2}\right)}{b \cdot (\delta_1 - \delta_2)}\right] \tag{4.51}$$

A flowchart for the $C_v^{res}{}_{mix}$ calculation is given in Figure 4.9.
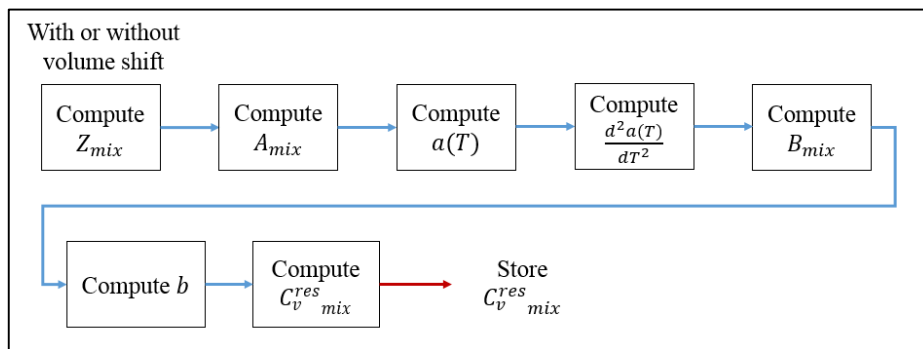
Figure 4.9. Flowchart for residual $C_v^{res}{}_{mix}$ calculation.

Finally, heat capacity $C_{v\,mix}$ of mixture can also be computed in mass units $[J/(kg.K)]$, as demonstrated in (4.52).

$$C_v^{mass}{}_{mix} = \frac{C_v^{molar}{}_{mix}}{MM_{mix}}$$

(4.52)

4.2 Reactor Modeling

Once thermodynamic and transport properties can be calculated, the modeling of a reactor is necessary. After all, the thermodynamic properties will be used to solve differential equations from mass, energy and momentum balances for adiabatic and autothermal operations.

4.2.1 Mass Balance

As discussed in the LITERATURE REVIEW, reactors used for ammonia synthesis are tubular. Generally, this operation occurs in a packed bed reactor (*PBR*), because the reaction arises in heterogeneous catalysis. In this work, flow in *PBR* will be modeled as in a *PFR*. Moreover, reaction rates of Section 3.2 were given in catalyst bed volume $[m^3]$ and not catalyst weight $[kg]$. Then, it will require the determination of the reactor volume. A scheme of a PFR reactor in terms of molar flows F_i $[mol/s]$ is given in Figure 4.10.
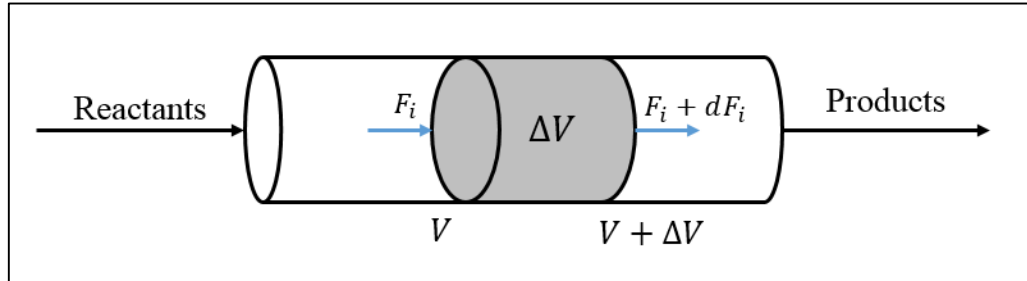
Figure 4.10. PFR in reactional volume ΔV (FOGLER, 2006).

A mass balance in element ΔV at steady state is performed, obtaining Equations (4.53) to (4.55).

$$Input - Output + Generation = Accumulation$$

(4.53)

$$F_i - (F_i + dF_i) + Rate_i . \Delta V = 0$$

(4.54)

$$\frac{dF_i}{dV} = Rate_i$$

(4.55)

In the expressions above, $Rate_i$ is the global reaction rate of component i $[mol/m^3 . s]$. However, as the reaction is heterogeneous, the effect of the mass transfer must be

accounted in the pseudo-homogeneous rate. This is given by the effectiveness factor η, as shown in Equation (4.56).

$$Rate_i = r_i.\eta \tag{4.56}$$

Effectiveness factor η varies from 0 to 1. It provides comparison between the reaction rate that has effects of mass transfer with the intrinsic rate. If η → 1, then the rate inside the particle is equal to the surface rate. If η → 0, then rate inside a particle is much lower than on the surface, exposing mass transfer problems. The calculation of η is explained in Section 4.2.4. Substituting Equation (4.56) in (4.55), we obtain the basic equation for a *PBR*.

$$\frac{dF_i}{dV} = r_i.\eta \tag{4.57}$$

Kinetic correction factor η goes from 0 to 1 and depends on pressure $[atm]$, temperature T $[K]$ and fractional conversion x_{N_2} $(-)$, in a polynomial expression, suggested by (DYSON and SIMON, 1968) in Equation (4.58). The coefficients b_o to b_6 are computed only in 150, 225 and 300 $[atm]$, as given in Table 4.9. Due to non-linearity, interpolation is not possible.

$$\eta = b_o + b_1.T + b_2.x_{N_2} + b_3.T^2 + b_4.x_{N_2}{}^2 + b_5.T^3 + b_6.x_{N_2}{}^3 \tag{4.58}$$

Table 4.9. Coefficients b_0 to b_6 for Equation (4.58). (DYSON and SIMON, 1968).

P (atm)	b_o	b_1	b_2	b_3	b_4	b_5	b_6
150	-17.539	0.0769	6.901	-1.083×10^{-4}	-26.425	4.928×10^{-8}	38.937
225	-8.213	0.0377	6.190	-5.355×10^{-5}	-20.869	2.379×10^{-8}	27.880
300	-4.676	0.0235	4.687	-3.463×10^{-5}	-11.280	1.541×10^{-8}	10.460

Moreover, the main component chosen is N_2, because it is the limiting reagent in many cases. Specifying molar flow F_i $[mol/s]$ in terms of conversion x_{N_2}, we obtain Equations (4.59) and (4.60). Many works also used x_{N_2} in its formulation (ELNAHSAIE et al., 1988).

$$F_{N_2} = F.y_{N_2}^o.\left(1 - x_{N_2}\right) = F_{N_2}^o.\left(1 - x_{N_2}\right) \tag{4.59}$$

$$dF_{N_2} = -F_{N_2}^o.dx_{N_2} \tag{4.60}$$

In the equation above, $F_{N_2}^o$ is initial molar flow of N_2 $[mol/s]$. Moreover, reaction rate r_{N_2} is computed in terms of r_{NH_3}, as shown in Equation (4.61).

$$r_{N_2} = \frac{-r_{NH_3}}{2} \tag{4.61}$$

Therefore, the final form of the equation (4.57) is given in volume or length, as shown in Equations (4.62) and (4.63). The reaction rate used was Singh and Saraf`s rate (Equation (3.22)). The only difference between differentials dL and dV is the sectional area A $[m^2]$.

$$\frac{dx_{N_2}}{dL} = \frac{A \cdot r_{NH_3} \cdot \eta}{2 \cdot F_{N_2}^o} \tag{4.62}$$

$$\frac{dx_{N_2}}{dV} = \frac{r_{NH_3} \cdot \eta}{2 \cdot F_{N_2}^o} \tag{4.63}$$

The conversion x_{N_2} is computed at each point of the reactor to calculate individual molar flows, as given in Table 4.10. Besides, y_i^o and y_i are the molar fractions of component i in the inlet and outlet stream of reactor $[-]$ and F is the total molar flow inside the reactor $[mol/s]$.

Table 4.10. Mass balance for ammonia reaction (DASHTI et al., 2006).

Component	Begin $[mol/s]$	Reaction $[mol/s]$	End $[mol/s]$	y_i
N_2	$F \cdot y_{N_2}^o$	$-F \cdot y_{N_2}^o \cdot x_{N_2}$	$F \cdot y_{N_2}^o \left(1 - x_{N_2}\right)$	$\dfrac{y_{N_2}^o \left(1 - x_{N_2}\right)}{1 - 2 \cdot y_{N_2}^o \cdot x_{N_2}}$
H_2	$F \cdot y_{H_2}^o$	$-3 \cdot F \cdot y_{N_2}^o \cdot x_{N_2}$	$F \cdot \left(y_{H_2}^o - 3 \cdot y_{N_2}^o \cdot x_{N_2}\right)$	$\dfrac{y_{H_2}^o - 3 \cdot y_{N_2}^o \cdot x_{N_2}}{1 - 2 \cdot y_{N_2}^o \cdot x_{N_2}}$
NH_3	$F \cdot y_{NH_3}^o$	$+2 \cdot F \cdot y_{N_2}^o \cdot x_{N_2}$	$F \cdot \left(y_{NH_3}^o + 2 \cdot y_{N_2}^o \cdot x_{N_2}\right)$	$\dfrac{y_{NH_3}^o + 2 \cdot y_{N_2}^o \cdot x_{N_2}}{1 - 2 \cdot y_{N_2}^o \cdot x_{N_2}}$
CH_4	$F \cdot y_{CH_4}^o$	$-$	$F \cdot y_{CH_4}^o$	$\dfrac{y_{CH_4}^o}{1 - 2 \cdot y_{N_2}^o \cdot x_{N_2}}$
Ar	$F \cdot y_{Ar}^o$	$-$	$F \cdot y_{Ar}^o$	$\dfrac{y_{Ar}^o}{1 - 2 \cdot y_{N_2}^o \cdot x_{N_2}}$

4.2.2 Energy Balances

For the same scheme in Figure 4.10, it is possible to compute the energy flows into the volume ΔV. This is given in Figure 4.11.
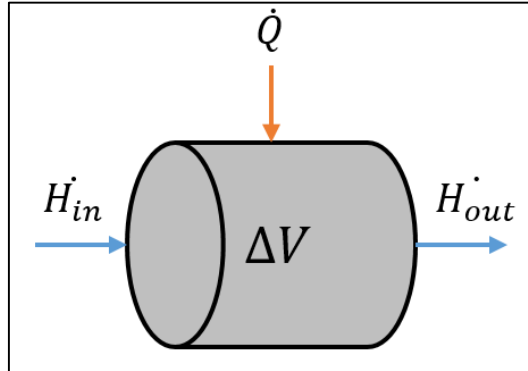
Figure 4.11. Energy flows in an element volume ΔV.

The energy balance in steady state is described by Equation (4.64).

$$\dot{Q} - \dot{W}_s + \dot{H}_{in} - \dot{H}_{out} = 0 \tag{4.64}$$

In the relation above, $\dot{Q}$ is energy removed or added by a stream $[W]$, $\dot{W}_s$ is the shaft work $[W]$, $\dot{H}_{in}$ is enthalpy rate in inlet stream $[W]$ and $\dot{H}_{out}$ is enthalpy rate in outlet stream $[W]$. Generally, the energy released by a reaction is superior to shaft work. Therefore, $\dot{W}_s$ is zero. Now the enthalpies $\dot{H}_{in}$ and $\dot{H}_{out}$ must be computed.

$$\dot{H}_{in} - \dot{H}_{out} = \sum_{i=1}^{N_{comp}} F_i^o \cdot (H_i^o - H_i) - \sum_{i=1}^{N_r} \xi_k \sum_{i=1}^{N_{comp}} v_{ki} \cdot H_i \tag{4.65}$$

In Equation (4.65), N_r is the number of reactions and ξ_k is the extent of the reaction $[mol/s]$. We must replace the terms v_{ki}, H_i and $(H_i^o - H_i)$, as expressed in the relations below. First, the heat of the reaction ΔH_r is found in Equation (4.66), and the term $(H_i^o - H_i)$ is specified in Equation (4.67).

$$\sum_{i=1}^{N_{comp}} v_{ki} \cdot H_i = \Delta H_r(T) \tag{4.66}$$

$$(H_i^o - H_i) = \int_T^{T_o} c_{p,i} dT = C_{p_{mix}} \cdot (T_o - T) \tag{4.67}$$

Therefore, Equation (4.64) becomes relation (4.68).

$$\dot{Q} - \left(\sum_{i=1}^{N_{comp}} F_i^o . C_{p_{mix}} \right) . (T - T_o) - \sum_{i=1}^{N_r} \xi_k . \Delta H_r(T) = 0 \tag{4.68}$$

In mass units, we can modify F_i^o.

$$\dot{Q} - \left(\dot{m} . C_{p_{mix}} \right) . (T - T_o) - \sum_{i=1}^{N_r} \xi_k . \Delta H_r(T) = 0 \tag{4.69}$$

As only one reaction takes place, the summation above becomes Equation (4.70). Therefore, the integrated equation is given in (4.71).

$$\sum_{i=1}^{N_r} \xi_k . \Delta H_r(T) = F_i^o . x_i . \Delta H_r(T) \tag{4.70}$$

$$\dot{Q} - \left(\dot{m} . C_{p_{mix}} \right) . (T - T_o) - F_i^o . x_i . \Delta H_r(T) = 0 \tag{4.71}$$

4.2.2.1 Adiabatic Operation

In the adiabatic operation, $\dot{Q} = 0$, because no heat is removed along the reactor. Therefore, we can write Equation (4.71) in differential form for *PFR*.

$$\dot{m} . C_{p_{mix}} . dT = F_i^o . dx_i . [-\Delta H_r(T)] \tag{4.72}$$

In the equation above, it is possible to replace dx_{N_2}/dL or dx_{N_2}/dV relations. Therefore, we obtain energy balance for the adiabatic case in terms of length and volume.

$$\frac{dT}{dL} = \frac{A . r_{NH_3} . \eta . (-\Delta H_r)}{\dot{m} . C_{p_{mix}}} \tag{4.73}$$

$$\frac{dT}{dV} = \frac{r_{NH_3} . \eta . (-\Delta H_r)}{\dot{m} . C_{p_{mix}}} \tag{4.74}$$

Observing relations in mass and energy, we can note that temperature rises without control along the reactor in the adiabatic operation. However, the reactor cannot exceed a maximum temperature, which is the catalyst limit. The heat of reaction ΔH_r $[J/mol]$ is

computed at each temperature T $[K]$ and pressure P $[atm]$ using a correlation (GILLESPIE and BEATTIE, 1930), as shown in Equation (4.75) and Table 4.11.

$$\Delta H_r = conv.\left[\left(a + \frac{b}{T} + \frac{c}{T^3}\right).P + (d.T) + (e.T^2) + (f.T^3) + g\right] \tag{4.75}$$

Table 4.11. Parameters for equation (4.75) (GILLESPIE and BEATTIE, 1930).

Parameter	Value	Parameter	Value
a	-0.5426	e	$-0.2525 \cdot 10^{-3}$
b	-840.609	f	$1.69197 \cdot 10^{-6}$
c	$-4.59734 \cdot 10^{8}$	g	-9157.09
d	-5.34685	$conv$ $[J/(mol)]$	4.184

4.2.2.2 Autothermal Operation

In autothermal mode, heat is also generated by the reaction. However, the reaction fluid removes the energy released by NH_3 production. Therefore, Equation (4.73) converts into Equation (4.76). There are two terms: one for temperature rise (same as adiabatic) the other for temperature decrease (cooling gas). Normally these converters are internally cooled, as given in Figure 3.4 (b).

$$\frac{dT}{dL} = \frac{A.r_{NH_3}.\eta.(-\Delta H_r)}{\dot{m}.C_{p_{mix}}} - \frac{U.A'.\left(T - T_g\right)}{\dot{m}.C_{p_{mix}}} \tag{4.76}$$

In the relation above, A' is the energy exchange area $[m^2/m]$, T_g is the cooling gas temperature $[K]$ and U is the overall heat exchange coefficient $[W/m^2.K]$. The signs $\pm$ in $\frac{dT_g}{dL}$ refer to co-current $(+)$ or countercurrent operation $(-)$. Therefore, the cooling fluid also changes its temperature according to Equation (4.77).

$$\frac{dT_g}{dL} = -\frac{U.A'.\left(T - T_g\right)}{\dot{m}.C_{p_{mix}}} \tag{4.77}$$

The values of U given in literature vary from 450 W/(m².K) to 850 W/(m².K) . A higher value of U provides more removal of energy released by reaction (MURASE et al., 1970). A co-current operation provides smaller gradients in temperature, while for countercurrent the differences are bigger. This is given in Figure 4.12 (a) and Figure 4.12 (b).

(a)   (b)
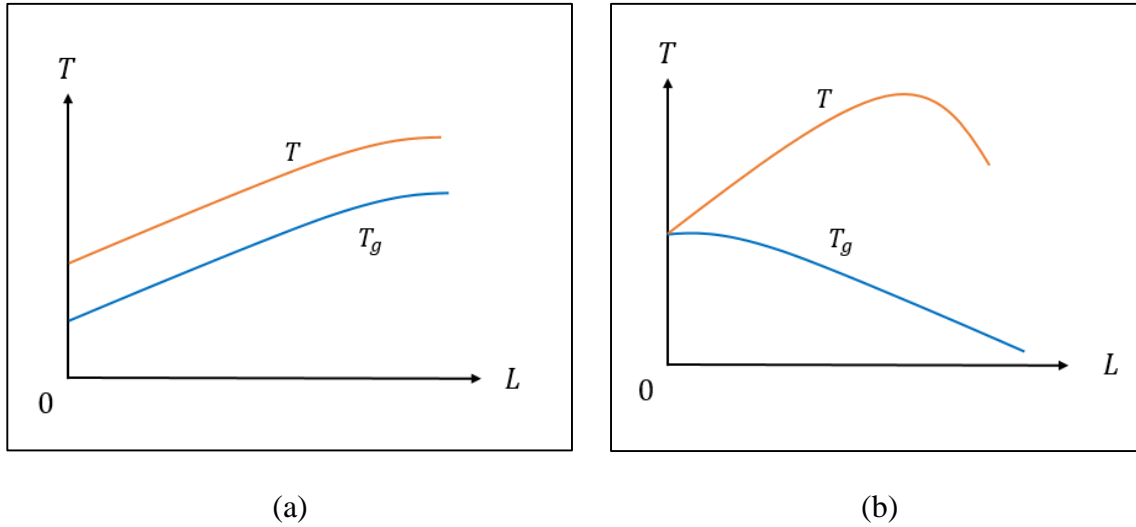
Figure 4.12. Average temperature profiles in (a) Co-current operation and (b) Countercurrent operation (FOGLER, 2006).

The differential equations can also be expressed in volume format, as expressed in Equations (4.78) and (4.79).

$$\frac{dT}{dV} = \frac{A.r_{NH_3}.\eta.(-\Delta H_r)}{\dot{m}.C_{p_{mix}}} - \frac{U.a'.(T - T_g)}{\dot{m}.C_{p_{mix}}} \tag{4.78}$$

$$\frac{dT_g}{dV} = -\frac{U.a'.(T - T_g)}{\dot{m}.C_{p_{mix}}} \tag{4.79}$$

The only change in relations above is a', which is the specific exchange area $[m^2/m^3]$.

4.2.3 Momentum Balance

The pressure is not constant along a fixed bed. Generally, the pressure loss is modeled using the Ergun Equation (ERGUN, 1952).

$$\frac{dP}{dL} = \frac{150.(1 - \varepsilon)^2.\mu.u}{\varepsilon^3.d_p{}^2} - 1.75.\frac{(1 - \varepsilon).\rho.u^2}{\varepsilon^3.d_p} \tag{4.80}$$

In the equation above, u is fluid superficial velocity $[m/s]$, μ is fluid viscosity $[Pa.s]$, ε is bed porosity $[-]$ and d_p is particle bed diameter $[m]$. For volume V, the pressure loss $\frac{dP}{dV}$ was set to zero (SINGH and SARAF, 1979). The viscosity is computed with a modified

PR model (WU et al., 2014). The values of particle diameter and void fraction of catalyst bed for adiabatic and autothermal reactors are given in Table 4.12 (DYSON and SIMON, 1968).

Table 4.12. Values for particle diameter and bed porosity used for simulation.

Model	d_p (m)	ε_{bed} $(-)$
Adiabatic	0.006	0.4
Autothermal	0.005	0.4

4.2.4 Pseudo-Homogeneous Model

In order to transpose the problem of heterogeneous catalysis, we use a pseudo-homogeneous model. It treats heterogeneous problems as one dimensional equations. The propositions below are used together with mass, energy and momentum balances in reactor simulations (Sections 4.2.1 to 4.2.3).

- Reactor operation occurs in steady-state.
- The pseudo-homogeneous model considers catalyst particle and bulk as one phase only. There are no partitions between gas in bulk and the catalyst surface.
- Reaction rate is only limited by experimental effectiveness factor η.
- There are only axial gradients in the reactor, due to the plug-flow pattern. Radial gradients are not accounted.

4.2.5 Mass Boundary Layer Calculations

Initially, the heterogeneous catalysis problem in an ammonia reactor is described in Figure 4.13. We can observe that there are thermal and mass boundary layers. Therefore, differences in temperature and concentrations exist between the catalyst surface and the boundary layer. Moreover, inside catalyst particles these gradients also occur, but they are not computed.

The main objective is to estimate the concentration differences between bulk and catalyst surface. The calculation requires dimensionless numbers, such as Sc, Re_p, j_d and others. First, the mass diffusivity is explained.
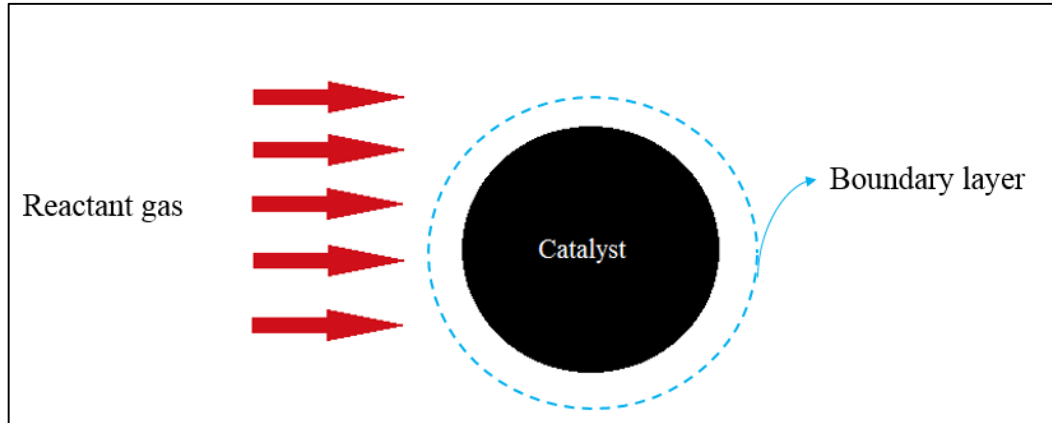
Figure 4.13. Representation of iron catalyst in an ammonia reactor.

4.2.5.1 Mass Diffusivity in a Gas Mixture

The mass diffusivity coefficient is important to measure limitations of mass transfer in the mixture. In the gaseous phase, as temperature increases, the diffusivity also increases, whereas as pressure increases, the diffusivity decreases. Therefore, under high pressures, the gas molecules have more difficulty in movement, causing diminution in diffusivity.

The calculation of diffusivity coefficients at 273 K and 1 atm conditions is made according to Equation (4.81) (ELNASHAIE, 1989). The equation below is the Maxwell-Stefan expression for mass diffusivities.

$$D_i^o = \frac{1}{\sum_{\substack{j=1 \\ j \neq i}}^{N_{comp}} \left[\left(\frac{1}{D_{ji}^o} \right) \cdot \left(y_j - \frac{v_j \cdot y_j}{v_i} \right) \right]} \tag{4.81}$$

In the equation above, D_i^o is the mass diffusivity of component i in mixture $[m^2/s]$, y_j is molar fraction of j component in mixture $[-]$. Moreover, v_i is the stoichiometric coefficient for i component in ammonia synthesis reaction and D_{ji}^o are the binary diffusivities for j and i components at 273 K and 1 atm $[m^2/s]$. The stoichiometric coefficients used are given in Table 4.13.

Table 4.13. Parameters for Equation (4.81).

Parameter	N_2 ($i = 1$)	H_2 ($i = 2$)	NH_3 ($i = 3$)
v	0.5	1.5	-1

The coefficients D_{ji}^o $[m^2/s]$ are given in a matrix computed by (DYSON and SIMON, 1968), and shown in Equation (4.82). Therefore, values for D_i^o can be calculated.

$$D_{ji}^o \; matrix = \begin{pmatrix} 1.55 \cdot 10^{-5} & 5.71 \cdot 10^{-5} & 1.61 \cdot 10^{-5} \\ 5.71 \cdot 10^{-5} & 1.604 \cdot 10^{-4} & 6.29 \cdot 10^{-5} \\ 1.61 \cdot 10^{-5} & 6.29 \cdot 10^{-5} & 1.92 \cdot 10^{-5} \end{pmatrix} \qquad (4.82)$$

Once diffusivities are computed in 273 K and 1 atm, the correction in temperature $T\;[K]$ and pressure $P\;[Pa]$ can be calculated. This is given in Equation (4.83).

$$D_i = D_i^o \cdot \left(\frac{T}{273.15}\right)^{1.75} \cdot \left(\frac{1}{P}\right) \qquad (4.83)$$

To summarize, the procedure for the calculation of the diffusivity vector is given in Figure 4.14. Methane (CH$_4$) and argon (Ar) diffusivities are not calculated because they are inert and are in low concentrations along synthesis. Moreover, NH$_3$ is considered the key component in diffusion, because it is the product of the main reaction.
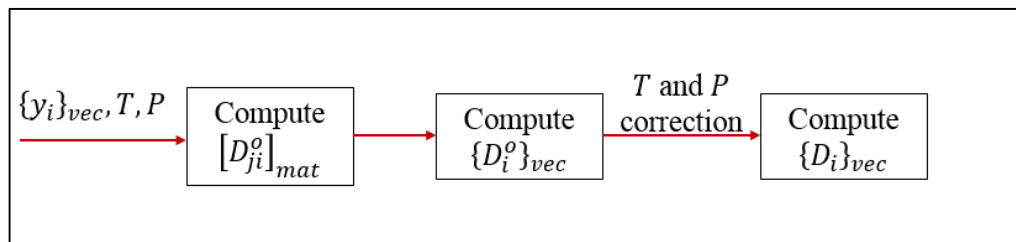
Figure 4.14. Flowchart for diffusivity vector calculation.

4.2.5.2 Schmidt Number

The Schmidt Sc number is calculated according to Equation (4.84). The number depends on viscosity, density and diffusivity in mixture. Moreover, three values of diffusivity D_i are computed, and a vector of Sc is obtained. However, as NH$_3$ is chosen as a key component, its value of Sc is computed.

$$Sc_i = \frac{\mu}{\rho \cdot D_i} \qquad (4.84)$$

4.2.5.3 Colburn Factor j$_d$

The j_d factor is important for mass transfer calculations. For fixed beds, it can be computed with experimental correlations. The correlation chosen was made by (DWIVEDI and UPADHYAY, 1977). It is valid for $Re_p > 10$ and given in Equation (4.85).

$$j_d = \left(\frac{0.4548}{\varepsilon_{bed}}\right) . Re_p^{-0.4069} \tag{4.85}$$

In the equation above, ε_{bed} is the bed void fraction $[-]$ and Re_p is the particle Reynolds number $[-]$. Furthermore, Re_p is calculated with particle diameter d_p $[m]$, mass flow rate G $[kg/(m^2.s)]$ and viscosity μ $[Pa.s]$, as given in Equation (4.86). Also, G is computed according to Equation (4.87).

$$Re_p = \frac{d_p . G}{\mu} \tag{4.86}$$

$$G = \frac{\dot{m}}{A} \tag{4.87}$$

To sum up, a flowchart for the calculation procedure for j_d is given in Figure 4.15.
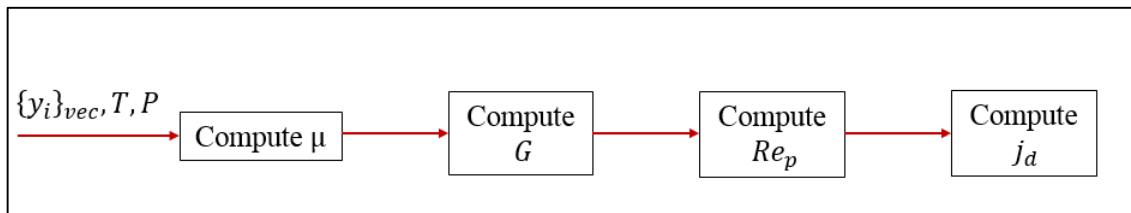
Figure 4.15. Flowchart for j_d factor calculation.

4.2.5.4 Sherwood Number

Another definition of the Sherwood number Sh $[-]$ is shown based on Colburn j_d factor, as given in Equation (4.88).

$$j_d = \frac{Sh}{Re_p . Sc^{1/3}} \tag{4.88}$$

Therefore, Sh is computed according to Equation (4.89). The j_d factor is computed in Equation (4.85).

$$Sh = j_d . Re_p . Sc^{1/3} \tag{4.89}$$

4.2.5.5 Mass Transfer Coefficient k_c and Boundary Layer Thickness δ

The coefficient k_c $[m/s]$ measures the resistance in mass transfer in a particle. A high value of k_c means low resistance in external mass transfer of particle to bulk. However,

under high pressures, different results can be achieved. The definition of this factor is found in Equation (4.90).

$$k_c = \frac{D_i . Sh}{d_p} \tag{4.90}$$

We can compute boundary layer thickness δ $[m]$ in catalyst particles using stagnant film theory, as given in Equation (4.91). Therefore, high values of k_c or low diffusivity D_i values decrease by δ. In our analysis of mass transfer, we consider that there are no differences of temperature between catalyst surface and bulk.

$$\delta = \frac{D_i}{k_c} \tag{4.91}$$

4.2.5.6 Concentration Differences in the Boundary Layer

All the previous factors are computed to estimate the concentration difference in mass external transport. The molar flux N_i $[mol/(m^2 . s)]$ is calculated using k_c $[m/s]$ and the concentration difference C_i $[mol/m^3]$, as given in Equation (4.92) by (ROBERTS, 2009).

$$N_i = k_c . \Delta C_i \tag{4.92}$$

The i component can be a reactant or a product. For convention, the key component was chosen as NH_3. Therefore, there will be more ammonia content at the catalyst surface than in bulk. We can multiply both sides of Equation (4.92) by the external area of particle a_g $[m^2]$, resulting in Equation (4.93).

$$R_{i_{part}} = N_i . a_g = k_c . a_g . \Delta C_i \tag{4.93}$$

In the equation above, $R_{i_{part}}$ is the rate which i reacts all over the catalyst $[mol/s]$. This rate can be transformed, because the pseudo homogeneous rate r_{NH_3} is given in $[mol/(m^3 . s)]$. So, we can multiply it by particle volume v_g $[m^3]$, obtaining Equation (4.94). Moreover, we must remember that rate r_{NH_3} is computed using bulk composition.

$$R_{i_{part}} = r_{NH_3} . \eta . v_g \tag{4.94}$$

Therefore, Equation (4.93) becomes Equation (4.95).

$$r_{NH_3} . \eta . v_g = k_c . a_g . \Delta C_i \tag{4.95}$$

Furthermore, our objective is to compute concentration difference ΔC_i. So, our final relation for ΔC_i is given in Equation (4.96).

$$\Delta C_i = \frac{r_{NH_3} \cdot \eta \cdot v_g}{k_c \cdot a_g} \tag{4.96}$$

ΔC_i is the difference of concentration between catalyst surface $C_{i_{surf}}$ $[mol/m^3]$ and bulk $C_{i_{bulk}}$ $[mol/m^3]$, as given in Equation (4.97).

$$\Delta C_i = C_{i_{surf}} - C_{i_{bulk}} \tag{4.97}$$

The concentration of the real gas in bulk is given by fugacities $\hat{f_i}$ $[Pa]$ (calculated in Thermodynamic Modeling), as given in Equation (4.98). Both temperature T $[K]$ and fugacities are computed with bulk parameters.

$$C_{i_{bulk}} = \frac{\hat{f_i}}{R \cdot T} \tag{4.98}$$

Finally, the concentration at the surface can be estimated. Therefore, we can compute if the difference in external transport is important, once the rate is computed with bulk parameters. To summarize all previous sections, a flowchart for the concentration difference is given in Figure 4.16. The vector $\{y_i\}_{vec}$ is the composition of the reactor at the length L or volume V at the integration of ODEs.
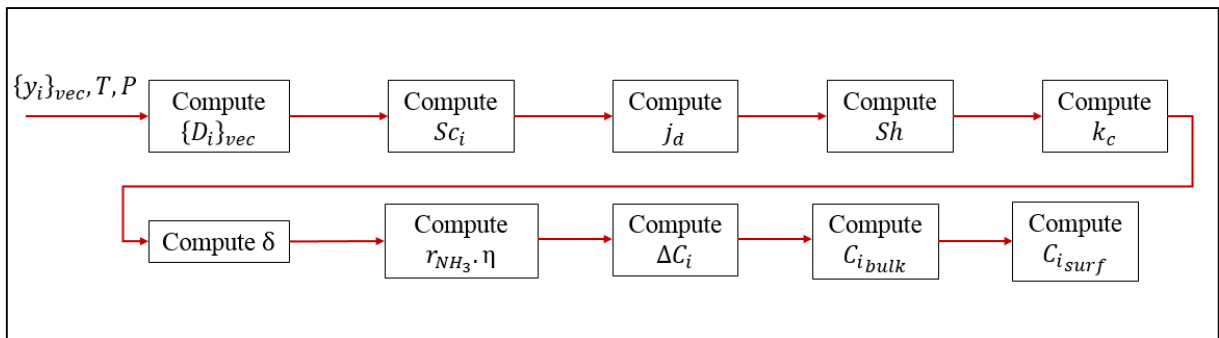
Figure 4.16. Flowchart for concentration differences calculation.

4.2.6 Numerical Simulation of a Reactor

All the pre-requisites for solutions to differential equations were explained. In this section, the main algorithms and flowcharts for simulation are given. The numerical simulation of an ammonia reactor consists in the solution to three different modules: Kinetic Module

(reaction rates given in Section 3.2), Thermodynamic Module (detailed in Section 4.1) and ODE Module (Section 4.2.1 to 4.2.4). They are interdependent, as given in Figure 4.17.
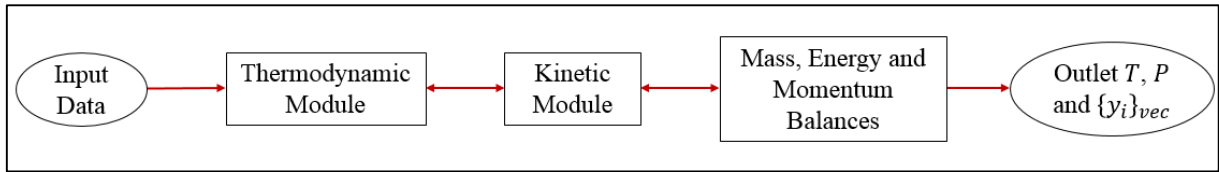
Figure 4.17. Main flowchart of modules used for calculations.

We must detail the input data, which is explained in Figure 4.18.
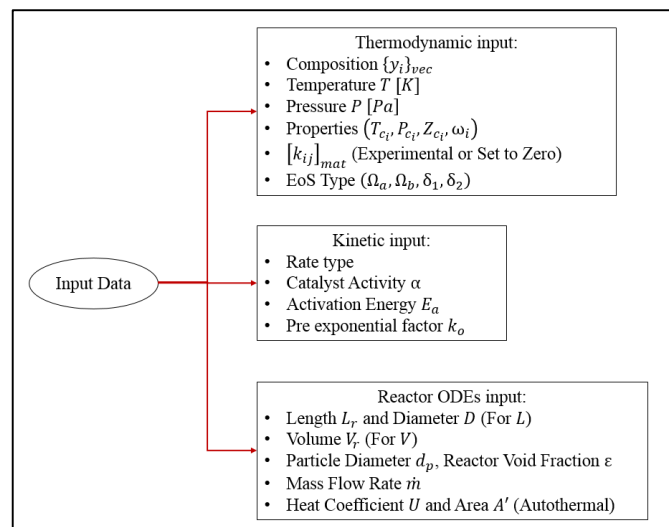
Figure 4.18. Input data detailed.

All thermodynamic properties are computed in Section 4.1. In the adiabatic case, the equations to be solved are (4.62), (4.73) and (4.80) in length and (4.63) and (4.74) in volume. For the autothermal mode, equations (4.62), (4.76), (4.77) and (4.80) are solved in length and equations (4.63), (4.78) and (4.79) are computed in volume. The solution procedure for conversion differential equation is detailed in Figure 4.19.
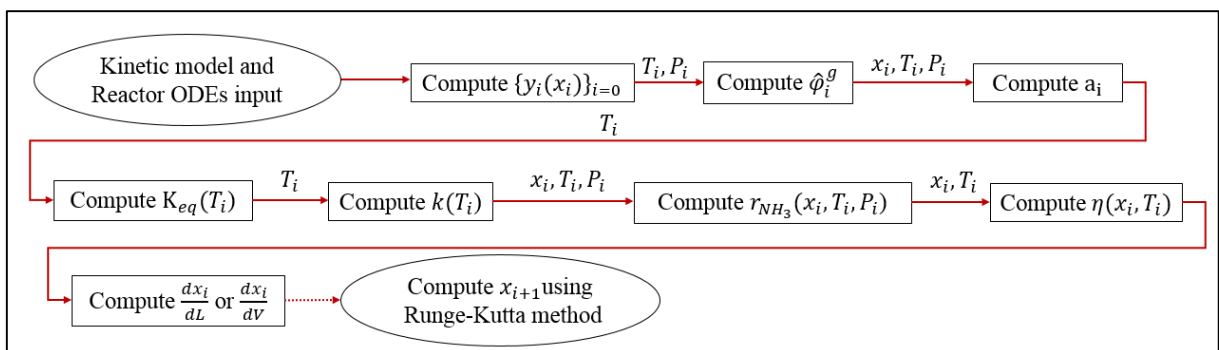
Figure 4.19. Calculation procedure for conversion block.

The conversion block in Figure 4.19 integrates kinetic, thermodynamic and mass transfer information. It makes this block the most important, because if the reaction rate is computed incorrectly, the energy balance will be wrong. Composition computation $\{y_i(X_i)\}$ to kinetic factor η will be reduced to "Calculate Corrected Reaction Rate". The next step is the energy balance for both adiabatic and autothermal models, visible in Figure 4.20.
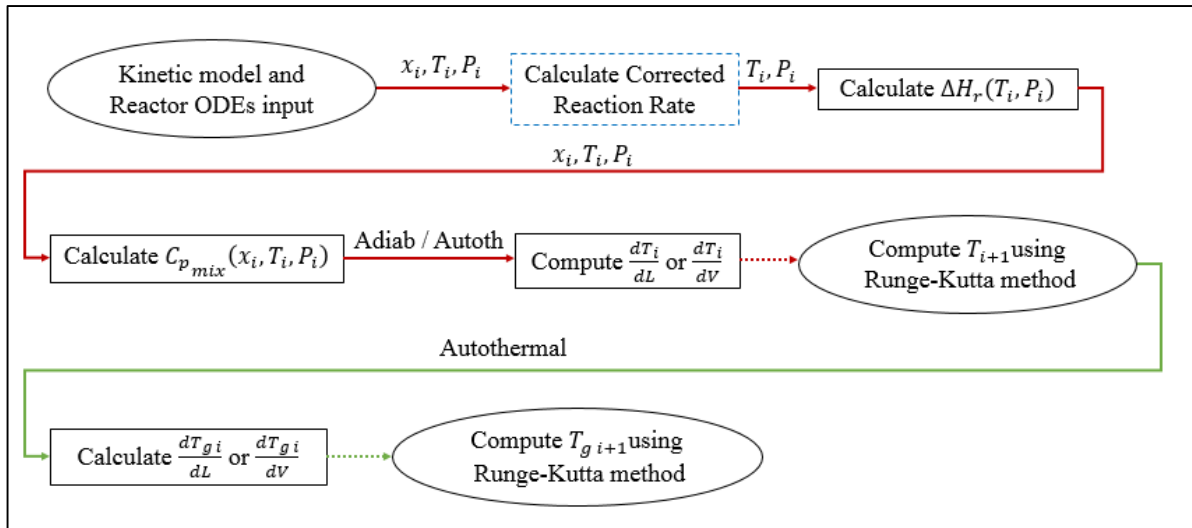
Figure 4.20. Calculation procedure for temperature block.

Finishing the reactors variables, the next step is to compute pressure at each iteration in L. This procedure is shown in Figure 4.21.
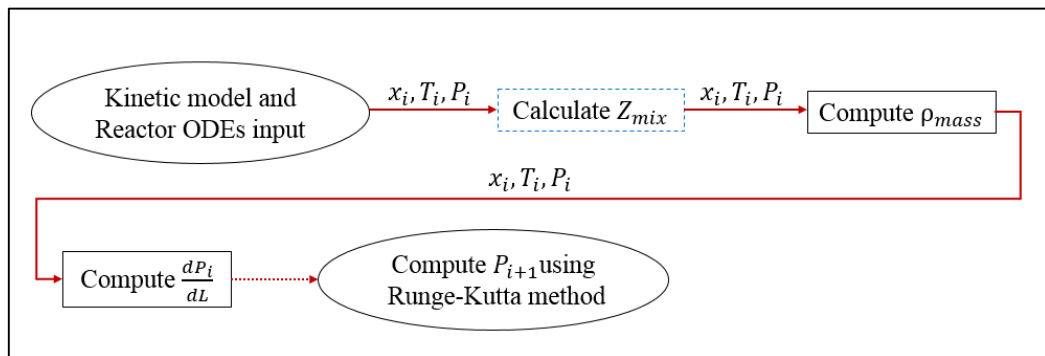
Figure 4.21. Calculation procedure for pressure block

The total approach for the ammonia reactor is given in Figure 4.22.
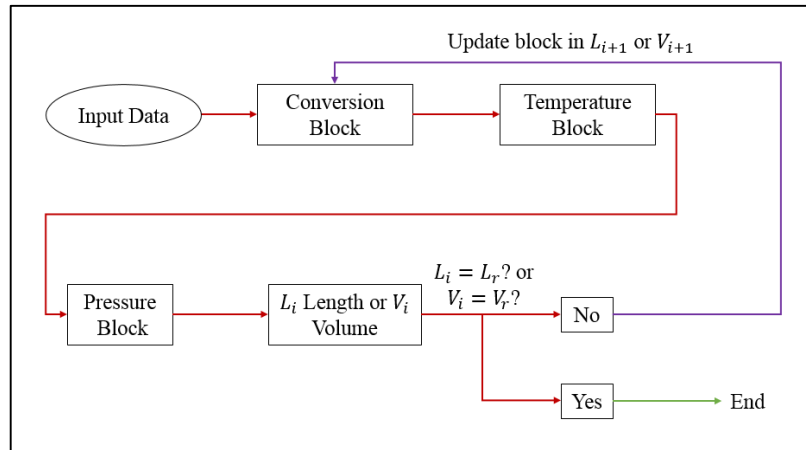
Figure 4.22. Concise flowchart for reactor calculation.

All content is joined in a code called *MARS (Models for Ammonia Synthesis Reactors)*. The program is developed on a modular structure using the software Wolfram Mathematica®, as given in Figure 4.23. All the items explained previously are separated into modules.
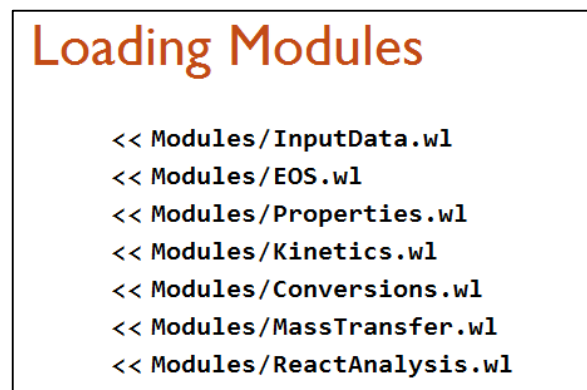
Figure 4.23. Modular structure of *MARS* using Wolfram Mathematica®.

The ODE system has only one dimension (L or V), therefore the stopping criteria for the numerical method is the end of the reactor. Moreover, the Runge-Kutta methods implemented are 4th order using fixed step size, or the Runge-Kutta-Fehlberg method with variable step size. The details of these methods are given below.

4.2.6.1 4th Order RK Method (fixed step size)

This method has a truncation error of 4th order. Therefore, 4 evaluations per step are made in each differential equation. For the adiabatic models, the variables are x_{N_2}, T and P. For the autothermal model, the variables solved are x_{N_2}, T, T_g and P. Both modes are solved by length L or volume V.

First, the fixed step h [m or m^3] is computed according to Equation (4.99). L_f is the final length of reactor [m] and L_i is the initial length, which normally is taken as zero. The same symbols are equivalent for the volume.

$$h = \frac{L_f - L_o}{N_{div}} = \frac{V_f - V_o}{N_{div}} \tag{4.99}$$

This step h is used to compute four k factors for each differential equation f, as given in Equations (4.100) to (4.103). In the equations below, $k_{1,i}$ is the first k factor for the i equation, and so on ($i = 1, 2, 3, \dots, m$). The parameter t_i refers to independent variable (L or V), whereas w_i is the m variable to be solved (CHAPRA and CANALE, 2009).

$$k_{1,i} = h.f(t_i, w_1, w_2, \dots, w_m) \tag{4.100}$$

$$k_{2,i} = h.f\left(t_i + 0.5.h, w_1 + 0.5.k_{1,1}, w_2 + 0.5.k_{1,2}, \dots, w_m + 0.5.k_{1,m}\right) \tag{4.101}$$

$$k_{3,i} = h.f\left(t_i + 0.5.h, w_1 + 0.5.k_{2,1}, w_2 + 0.5.k_{2,2}, \dots, w_m + 0.5.k_{2,m}\right) \tag{4.102}$$

$$k_{4,i} = h.f\left(t_i + 0.5.h, w_1 + k_{3,1}, w_2 + k_{3,2}, \dots, w_m + k_{3,m}\right) \tag{4.103}$$

Finally, an update of variables is needed to complete one iteration. It is shown in Equations (4.104) and (4.105). The method is finished with $t_i = L_f$ or $t_i = V_f$.

$$w_m = w_m + \left(\frac{k_{1,m} + 2.k_{2,m} + 2.k_{3,m} + k_{4,m}}{6}\right) \tag{4.104}$$

$$t_i = t_i + h \tag{4.105}$$

One of the disadvantages of this method is the fixed step size, causing overload. After all, in some regions, the functions can have a smaller truncation error, which could provide larger steps. With fewer steps, the computation time can decrease too. Moreover, if the dynamics of the system changes rapidly, this method can also present problems.

4.2.6.2 4th and 5th Order RKF Method (variable step size)

The Runge-Kutta-Fehlberg is a method that makes evaluations of 4th and 5th order functions. Generally, 9 total evaluations of each function would be required. However, the advantage of this method is that there are only 6 evaluations (from $k_{1,i}$ to $k_{6,i}$) for both estimations. Moreover, a strategy of error control will be implemented. It means that the step will vary according to the error between the 4th and 5th order estimations.

Initially, the previous step h given in Equation (4.99) is a first estimation. We will call it h_o. Furthermore, the k factors from Equations (4.106) to (4.111) below are computed.

$$k_{1,i} = h.f(t_i, w_m) \tag{4.106}$$

$$k_{2,i} = h.f\left(t_i + 0.25.h, w_m + 0.25.k_{1,m}\right) \tag{4.107}$$

$$k_{3,i} = h.f\left(t_i + \frac{3}{8}.h, w_m + \frac{3}{32}.k_{1,m} + \frac{9}{32}.k_{2,m}\right) \tag{4.108}$$

$$k_{4,i} = h.f\left(t_i + \frac{12}{13}.h, w_m + \frac{1932}{2197}.k_{1,m} - \frac{7200}{2197}.k_{2,m} + \frac{7296}{2197}.k_{3,m}\right) \tag{4.109}$$

$$k_{5,i} = h.f\left(t_i + h, w_m + \frac{439}{216}.k_{1,m} - 8.k_{2,m} + \frac{3680}{513}.k_{3,m} - \frac{845}{4104}.k_{4,m}\right) \tag{4.110}$$

$$k_{6,i} = h.f\left(t_i + 0.5.h, w_m - \frac{8}{27}.k_{1,m} + 2.k_{2,m} - \frac{3544}{2565}.k_{3,m} + \frac{1859}{4104}.k_{4,m}\right.$$
$$\left. - \frac{11}{40}.k_{5,m}\right) \tag{4.111}$$

The factors $k_{1,i}$ to $k_{6,i}$ are used to compute the update in system variables, as given in Equations (4.112) and (4.113).

$$\widetilde{w}_{m+1} = w_m + \frac{16}{35}.k_{1,m} + \frac{6656}{12825}.k_{3,m} + \frac{28561}{56430}.k_{4,m} - \frac{9}{5}.k_{5,m} + \frac{2}{55}.k_{6,m} \tag{4.112}$$

$$w_{m+1} = w_m + \frac{25}{216}.k_{1,m} + \frac{1408}{2565}.k_{3,m} + \frac{2197}{4104}.k_{4,m} - \frac{1}{5}.k_{5,m} \tag{4.113}$$

In the equations above, $\widetilde{w}_{m+1}$ is the 5th order estimation and w_{m+1} is the 4th order estimation. Therefore, it is possible to compute the difference w_{res_m} between the two approximations, as expressed in Equation (4.114).

$$w_{res_m} = |\widetilde{w}_{m+1} - w_{m+1}| \tag{4.114}$$

Once our iteration has ended, we now need to update the step h_o according to our error w_{res}. This is called the error control strategy. There are many described in (BURDEN and FAIRES, 2010) and (CHAPRA and CANALE, 2009). First, we calculate all errors w_{res_m}. The user can specify an absolute tolerance for each variable m (conversion, temperature(s) and

pressure), called tol_m. Therefore, the ratio q_m is computed for each variable m, as given in conditions (4.115) or (4.116).

If $tol_m \leq w_{res_m}$, we have Equation (4.115).

$$q_m = 0.9. \left(\frac{tol_m}{w_{res_m}} \right)^{0.2} \tag{4.115}$$

If $tol_m > w_{res_m}$, we have Equation (4.116).

$$q_m = 0.85. \left(\frac{tol_m}{w_{res_m}} \right)^{0.25} \tag{4.116}$$

Therefore, if the error is greater than tolerance, the initial step h_o will have to be decreased. To the contrary, the step h_o can be increased if the error is not significative. For an ODE system, we make a mean of q_m according to Equation (4.117). Finally, our next step h in the next iteration is expressed as given in Equation (4.118).

$$q = (q_1. q_2. q_3 .... q_m)^{1/m} \tag{4.117}$$

$$h = h_o. q \tag{4.118}$$

The procedure is repeated until the stopping criteria, which is the same as the fixed step size method. In other words, when the method reaches the end of the reactor (L_f or V_f), the problem is solved.

5   RESULTS/DISCUSSION

Historically, thermodynamic modeling has proved to be reliable in *HPHT* situations. Moreover, once all the methodology about mass, heat and momentum balances is explained, the results can be generated. Therefore, both results in adiabatic and autothermal model are given.

Initially, the expression developed by Singh and Saraf is chosen for all reactor simulations in this section (Equation (3.22)). Moreover, the *PR* model in *EoS* is chosen for simulation. The first part of the results is a summary of the effects in α variation in the reaction rate (Equation (3.22)), in order to fit the model with *EoS* computed chemical activity and not by correlation. Then, a comparison with the Runge-Kutta method is performed, now with α value tuned. All previous estimations are made to validate reactor models with plant data. After that, validation with adiabatic and autothermal models are performed using the fitted model. Then, the parametric sensitivity and boundary layer estimations with both models are also calculated.

5.1   Variation of α in the Reaction Rate

As discussed in Section 3, the chemical activities originally are computed using a correlation proposed by Dyson and Simon in Equation (3.22) (Singh and Saraf rate). However, when the *EoS* approach is used, it is expected that chemical activity decreases, due to compositional interactions. Therefore, the reaction rate computed also decreases its value. So, the catalyst activity factor α is fitted to the *EoS* approach in *MARS*. The fit is made according to an adiabatic reactor in literature (SINGH and SARAF, 1979). Only the first bed is calculated in temperature and conversion. After all, the entire adiabatic reactor is computed in Section 5.3.1. The parameters for this reactor are given in Table 5.1.

Table 5.1. Input parameters and experimental plant data for the 1st adiabatic bed (SINGH and SARAF, 1979).

Parameter	Value	Parameter	Value	Parameter	Value	Exp. Data	Value
y_{N_2}	0.2219	y_{CH_4}	0.0546	$T_{in}(K)$	658.15	$T_{out\,1}(K)$	780.15
y_{H_2}	0.6703	y_{Ar}	0.0256	$P_{in}(atm)$	226	$x_{N_2\,out\,1}(\%)$	15.78
y_{NH_3}	0.0276	$\dot{m}(kg/s)$	29.8215	$V_1(m^3)$	4.75		

The temperature variation in the adiabatic converter with α alterations is given in Figure 5.1.
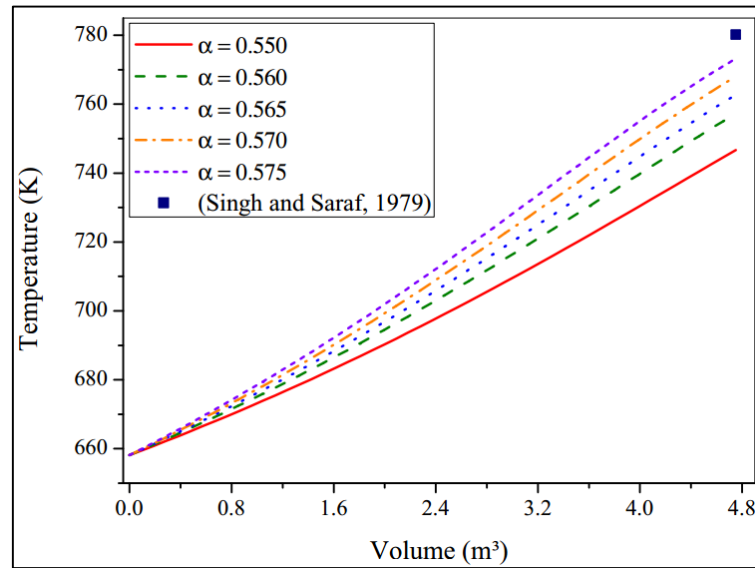
Figure 5.1. Temperature profile in 1st bed using α variations at *MARS* (*EoS* approach).

In Figure 5.1, some important features are noted. When $\alpha = 0.55$ (original value), the final temperature is quite distant from plant data. Therefore, α has to be increased. Even in the highest value $\alpha = 0.575$, there are some errors related to outlet temperature. Probably some interactions inside this reactor cannot be explained only by a pseudo-homogeneous approach. Then, the conversion profile has to be analyzed for a better decision. Moreover, as α increases, the outlet temperature also increases, due to a higher reaction rate. The N_2 conversion variation in an adiabatic converter with α alterations are shown in Figure 5.2.
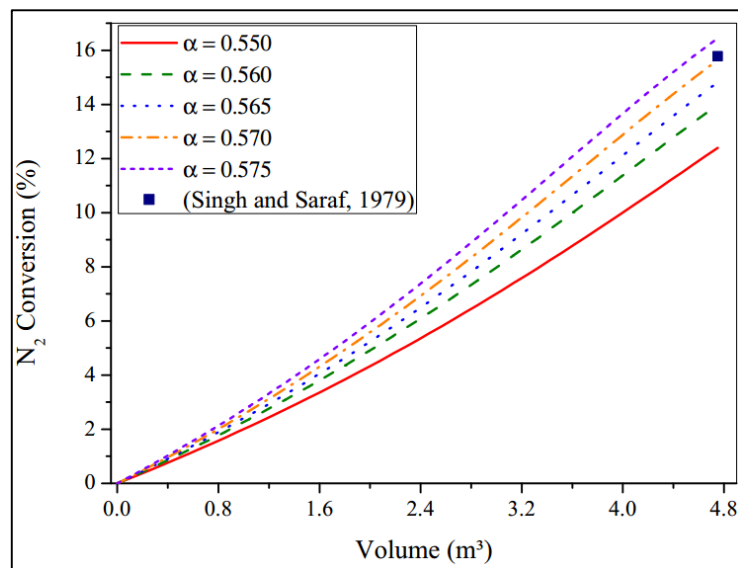
Figure 5.2. Conversion profile in 1st bed using α variations at *MARS* (*EoS* approach).

In Figure 5.2, as α rises, the outlet conversion also increases, because the reaction rate is higher. Moreover, at $\alpha = 0.570$, the model does well in predicting the outlet conversion. Therefore, the original value of $\alpha = 0.550$ in Singh and Saraf rate should be replaced by $\alpha = 0.570$ when using the *EoS* approach from now on.

5.2 Comparison between RK4 and RKF Methods

Besides α fitting in a rate expression, the total number of iterations in a reactor simulation is also important. After all, as the method computes fewer iterations, the computational time decreases. Therefore, the comparison between 4th order RK method with fixed step and 4th and 5th order *RKF* methods with variable step is necessary.

First, the adiabatic case is simulated. The same reactor studied in Table 5.1 is computed now using $\alpha = 0.570$ with both RK methods. The temperature profile is given in Figure 5.3.
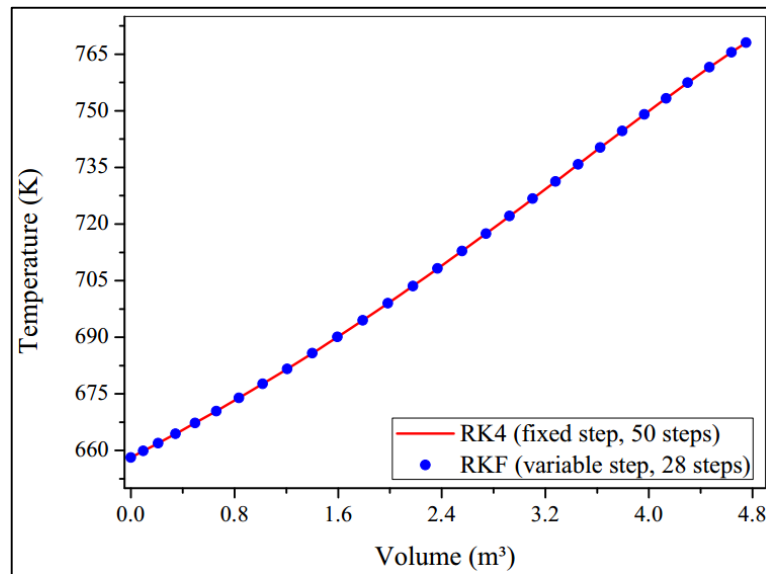
Figure 5.3. Temperature profile in 1st bed using two RK methods (α=0.570 and *EoS* approach).

In Figure 5.3, the temperature profiles registered by both Runge-Kutta methods are the same. The *RKF* method needs only 28 iterations, on the other hand, the *RK4* method needs 50 iterations. Therefore, many regions in the adiabatic reactor have small truncation errors, which makes the *RKF* method increase the step h and decrease total iterations. To summarize, both methods prove reliable in adiabatic simulation.

The autothermal case simulated has the parameters given in Table 5.2.

Table 5.2. Input parameters for autothermal reactor (SINGH and SARAF, 1979).

Parameter	Value	Parameter	Value	Parameter	Value
y_{N_2}	0.2190	y_{Ar}	0.0360	$V(m^3)$	4.07
y_{H_2}	0.6500	$\dot{m}(kg/s)$	6.038	$a'(m^2/m^3)$	10.29
y_{NH_3}	0.0520	$T_{in}(K)$	694.15	$U(W/m^2.K)$	465.2
y_{CH_4}	0.0430	$P_{in}(atm)$	279		

The temperature profiles given by the *RK4* and *RKF* method are given in Figure 5.4. The methods present differences in temperature prediction, though. Moreover, the main alterations are noted after the maximum temperature point (T_{max} in Figure 5.4). T_{max} is equivalent to a zero value in derivative $\frac{dT}{dV}$. Therefore, after this point, the equation $\frac{dT_g}{dV}$ becomes dominant, making T value only decrease. To summarize, the truncation errors are important after this point.

For the same step size, the *RKF* method provides better reliability, due to 4th and 5th order error estimations. Another important measure is the number of iterations needed. Even with variable step, 43 iterations are made. Therefore, the autothermal reactor contains more non-linear terms than the adiabatic case, make numerical integration more difficult.
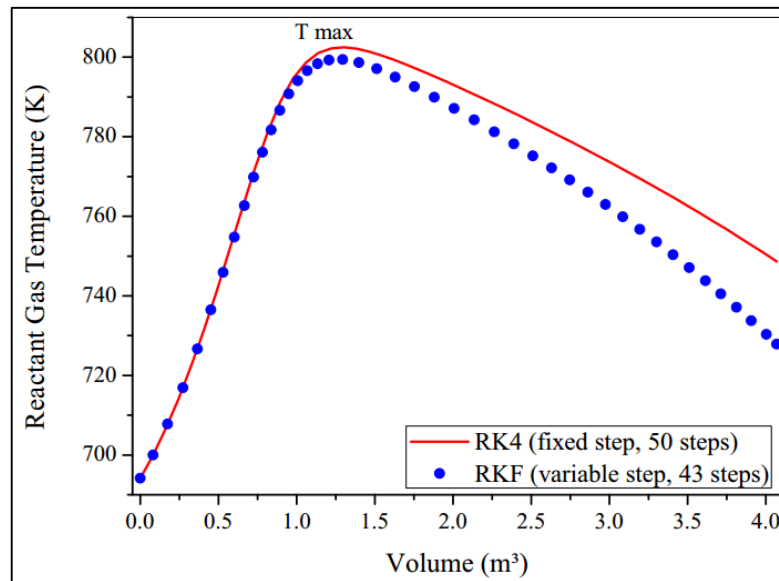
Figure 5.4. Temperature profile in autothermal reactor using two RK methods (α=0.570 and *EoS* approach).

Consequently, the RKF is chosen to simulate the remaining results with $\alpha = 0.570$.

5.3 Validations with Fitted Model

Even with a good numerical method and a robust code, validations of reactors models are necessary. The *RKF* method and $\alpha = 0.570$ are selected for Singh and Saraf modified rate. Furthermore, an adiabatic reactor containing 3 fixed beds in series and the same autothermal converter of Section 5.2 are calculated. Both models are reliable compared to plant data.

5.3.1 Adiabatic Case

Here we have three reactors in series. The first bed is computed in Section 5.1. Therefore, all inlets parameters remain the same. The only additional information for simulation is the inlet temperature of the 2nd and 3rd reactors and their respective volume, as given in Table 5.3.

Table 5.3. Plant data for three adiabatic beds in series (SINGH and SARAF, 1979).

Bed	$V(m^3)$	T_{in} (K)	T_{out} (K)	Outlet x_{N_2}(%)
1	4.75	658.15	780.15	15.78
2	7.2	706.15	775.15	25.55
3	7.8	688.15	728.15	30.91

The temperature profile computed is given in Figure 5.5.
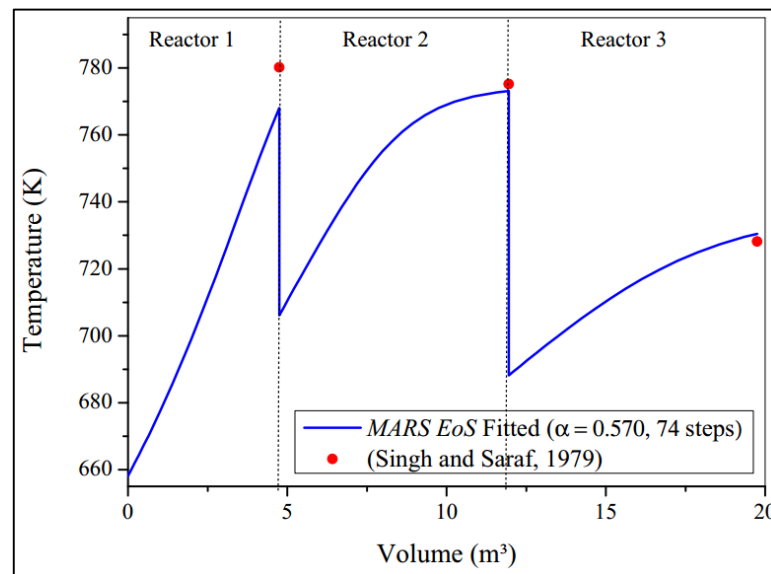
Figure 5.5. Plant data and *MARS EoS* model temperature profile (adiabatic reactor).

In Figure 5.5, the highest errors in temperature are noted in the first reactor. Moreover, the first converter is the place where the rate has its highest values, therefore, it can provide more errors compared to the others. However, in the second and third converters, the simulated temperature gives good results compared to plant data. In all simulations of the adiabatic arrangement, 74 iterations are required with *RKF*. It is a good result compared to our previous division on the *RK4* method (50 iterations at each reactor). After all, if the *RK4* method is used, 150 iterations would be required.

To complete, the relative errors of temperature are given in Table 5.4. It proves a good comparison between *MARS* and plant data (SINGH and SARAF, 1979). The maximum error of temperature reached by other authors was less than 6 % (SINGH and SARAF, 1979).

Table 5.4. Comparison between outlet temperature in plant data and the *MARS* model.

Bed	$T_{out_{plant}}$ (K)	$T_{out_{MARS}}$ (K)	$Rel.\,Error$ (%)
1	780.15	768.04	1.55
2	775.15	773.14	0.26
3	728.15	730.46	0.32

Even with good results in temperature predictions, the conversion is another important variable. The composition of the reactor depends on conversion, after all. Furthermore, it is more sensitive to variations than temperature. The conversion profile computed by *MARS* is given in Figure 5.6.
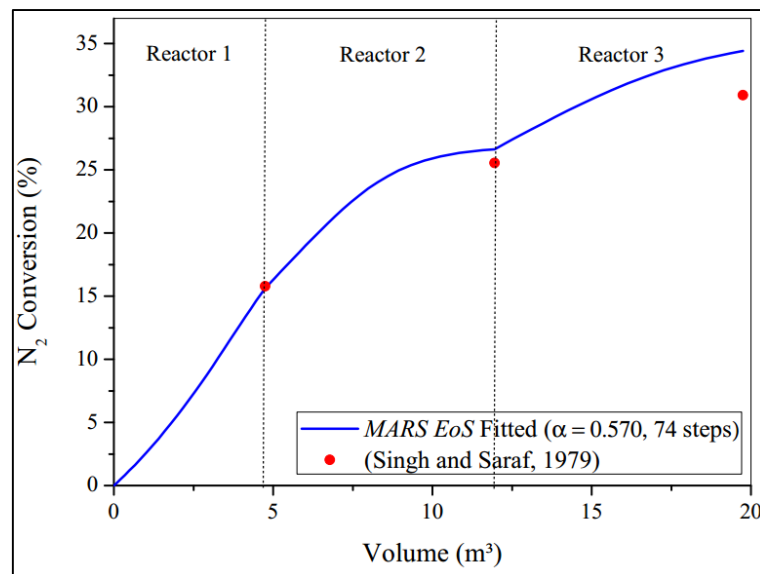
Figure 5.6. Plant data and *MARS EoS* model conversion profile (adiabatic reactor).

In Figure 5.6, the highest error in conversion occurred in the third reactor. The first and second converters present a good comparison with plant data. The main error in the third reactor is the previous errors inherited by the first and second reactors. In other words, the error was propagated. Moreover, the final converter is where the reaction rate presents the smallest value. The relative errors in conversion are summarized in Table 5.5. To summarize, even with the difference in conversion in the 3rd reactor, the *MARS* model is reliable for adiabatic reactor simulation, because the temperature is usually the control variable in ammonia reactors. Errors in literature reached less than 0.5 % (SINGH and SARAF, 1979).

Table 5.5. Comparison between outlet conversion in plant data and the *MARS* model.

Bed	$x_{N_2\,out\,plant}$ (%)	$x_{N_2\,out\,MARS}$ (%)	$Rel.\,Error$ (%)
1	15.78	15.64	0.88
2	25.55	26.64	4.27
3	30.91	34.42	11.36

5.3.2 Autothermal Case

The same autothermal reactor simulated in Section 5.2 will be compared to literature (SINGH and SARAF, 1979). The additional information given in Table 5.6 is related to plant data (countercurrent reactant gas temperature along the reactor).

Table 5.6. Reactant gas temperature in autothermal reactor (SINGH and SARAF, 1979).

$V\ (m^3)$	$T\ (K)$	$V\ (m^3)$	$T\ (K)$
0	694.15	2.21	781.15
0.17	716.15	2.54	771.15
0.51	759.15	2.88	756.15
0.85	789.15	3.22	748.15
1.19	799.15	3.56	733.15
1.53	796.15	3.90	719.15
1.87	787.15	4.07	711.15

Therefore, the numerical simulation is given in Figure 5.7.
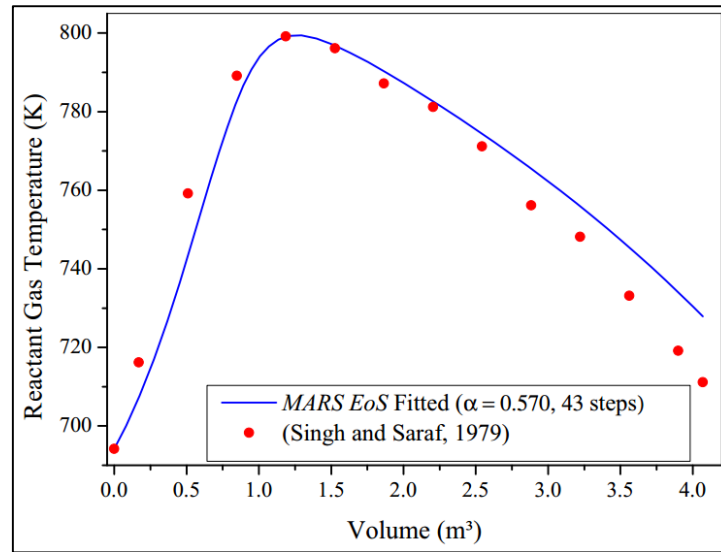
Figure 5.7. Comparison between the *MARS EoS* model and plant data (autothermal reactor).

In Figure 5.7, differences are noted between simulation and plant data. First, only at the end of the autothermal reactor are the differences significant. These occur due to a change of dynamics in the *ODE* system. However, the maximum temperature point is well predicted, which reinforces the method`s effectiveness. The maximum relative error was 2.7 % in the end of reactor, due to high nonlinearity of equations.

Moreover, the high non-linearity of the autothermal reactor is proved in Figure 5.8 below. We observe that in the maximum temperature region, the step h $[m^3]$ decreases, because the truncation errors are higher. Moreover, after this point, the step increases because fewer errors in *ODE* system are calculated by the *RKF* method.
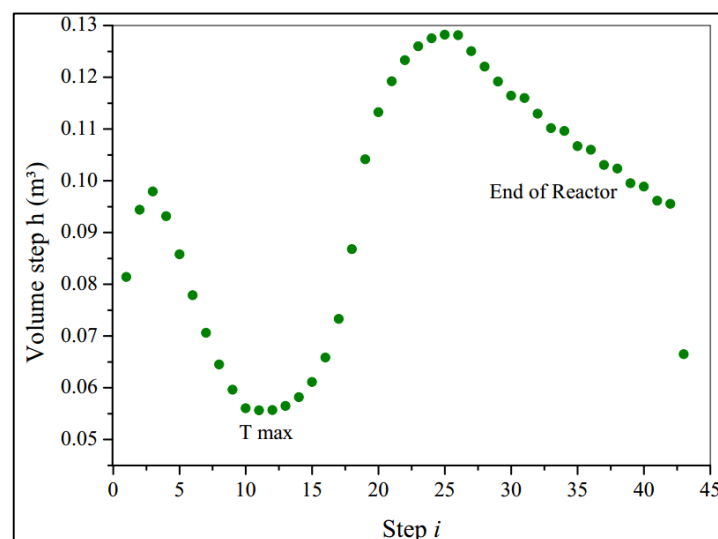
Figure 5.8. Step size variation in autothermal reactor using the *RKF* method.

To summarize, the relative errors at each point of the autothermal reactor are given in Table 5.7. It proves also the reliability of the *MARS* model for the autothermal reactor. Other authors reached 3.2 % of maximum relative difference in temperature, which was an acceptable value (SINGH and SARAF, 1979).

Table 5.7. Relative errors in reactant gas temperature in autothermal reactor (SINGH and SARAF, 1979).

$V\ (m^3)$	$Rel.\ Error\ (\%)$	$V\ (m^3)$	$Rel.\ Error\ (\%)$
0	0.00	2.21	0.01
0.17	1.47	2.54	0.17
0.51	1.78	2.88	1.27
0.85	1.05	3.22	1.28
1.19	0.07	3.56	1.68
1.53	0.46	3.90	1.84
1.87	0.56	4.07	2.66

5.4 Parametric Sensitivity

Both models show that they are reliable for simulations in the previous section. Therefore, more analysis can be done on pseudo-homogeneous modeling. One area is parametric sensitivity, when input variables are changed in order to detect variations in output variables. All calculations are made using the *RKF* method with variable step size and the fitted *EoS* model in reaction rate.

In the adiabatic model, the analysis is realized in three reactors. First, the inlet temperature, pressure and NH_3 molar fraction are varied. The effects on temperature, pressure, conversion and effectiveness factor profiles are detected in each case. Moreover, for one bed analysis, the inlet temperature effect in the final conversion and outlet temperature is also computed.

In the autothermal model, the same input variables are varied. Furthermore, the heat exchange coefficient is also changed. The inlet temperature effect on the maximum

temperature, output temperature and output conversion are also accounted for. There are no arrangements of reactors in this model.

5.4.1 Adiabatic Model

In this operation, there is no heat removed along the reactor, which is a disadvantage. However, this design is more suited to big production. In all the analysis, the reactor consists of 3 beds, with indirect cooling. Their dimensions are given in Figure 5.9. The values of volume and length were estimated using literature ((AZARHOOSH et al., 2014) and (SINGH and SARAF, 1979)).
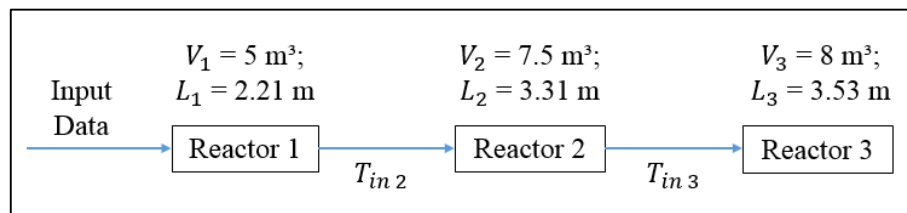
Figure 5.9. Flowchart for adiabatic beds parametric sensitivity.

5.4.1.1 Effect of inlet temperature T_{in}

In this operation, only the inlet temperature of the 1st reactor is varied. The temperatures $T_{in\,2}$ and $T_{in\,3}$ maintain the same values (as given in Table 5.8). Moreover, the *RKF* method with variable step size is used for numerical simulation.

Table 5.8. Parameters for inlet temperature variation in adiabatic model (643.15 K, 663.15 K and 683.15 K).

Constraints for adiabatic simulation T_{in_1}			
$P_{in}(atm) - 1st\ bed$	150	$y_{N_2\,in}$	0.22
$T_{in\,2}(K) - 2nd\ bed$	693.15	$y_{H_2\,in}$	0.66
$T_{in\,3}(K) - 3rd\ bed$	683.15	$y_{NH_3\,in}$	0.03
$D_r(m)$	1.7	$y_{CH_4\,in}$	0.045
$d_{part}(m)$	0.006	$y_{Ar\,in}$	0.045
$\varepsilon_{bed}(-)$	0.4	$\dot{m}(kg/s)$	30.0

The inlet temperature effect along gas temperature is given in Figure 5.10. Observing Figure 5.10, we can note that the lowest inlet temperature ($T_{in} = 643.15\ K$) gave the highest profiles along second and third reactors. After all, smaller temperatures provide smaller rates, which give minor conversions. Therefore, after first reactor, more N_2 can be converted, giving a more accentuated profile ($T_{in} = 643.15\ K$).

On the other hand, high inlet temperatures present high reaction rates, converting more N_2 in the first bed. However, it becomes more difficult to react in the second and third converters. Therefore, the temperature rise is not so large as in smaller T_{in} values, even with high rates. In the three cases, the number of iterations is similar. So, there is not a nonlinear increase from one case to another.
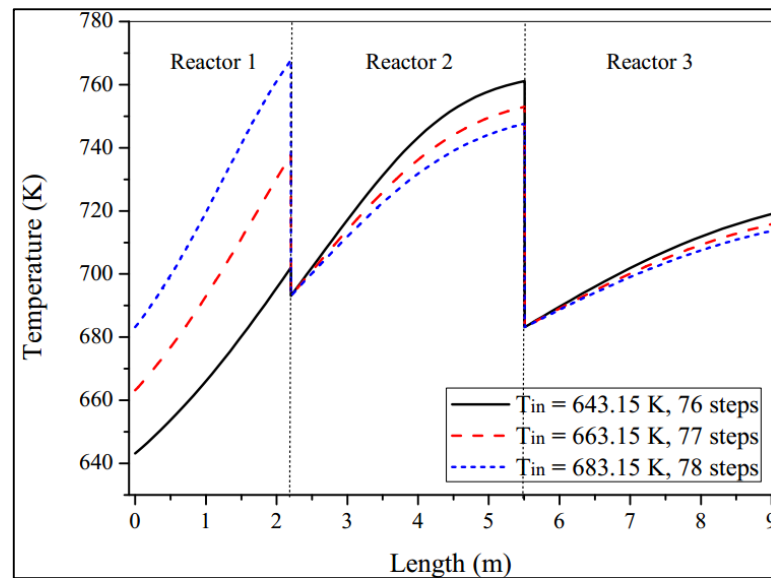
Figure 5.10. Temperature profiles in beds (Tin = 643.15 K, 663.15 K and 683.15 K).

The pressure profiles along reactors are shown in Figure 5.11. A smaller T_{in} value (643.15 K) provides minor pressure loss, while T_{in} values of 683.15 K give the maximum pressure loss. Moreover, the maximum value of ΔP in simulations is 6.7%, which is less than the 10% maximum allowed. In this situation, the high temperature makes gas viscosity increase in the first bed, raising pressure loss in the Ergun Equation (Equation (4.80)). Therefore, the pressure loss of the first bed is carried to the others.
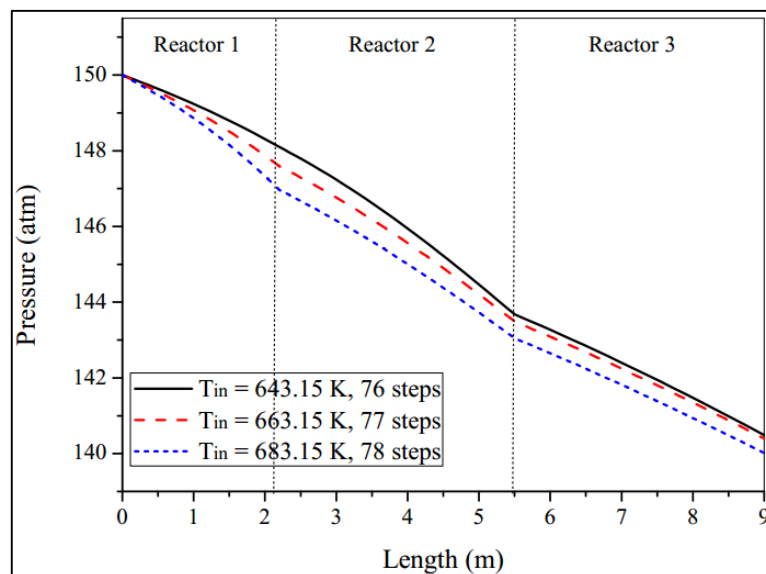
Figure 5.11. Pressure profiles in beds (Tin = 643.15 K, 663.15 K and 683.15 K).

Besides temperature and pressure, another important measure inside our reactor is composition. As there is only one reaction, the conversion profile x_{N_2} gives indirectly the other molar fractions (see Table 4.10). For the inlet temperature variation case, the conversion profile is given in Figure 5.12.
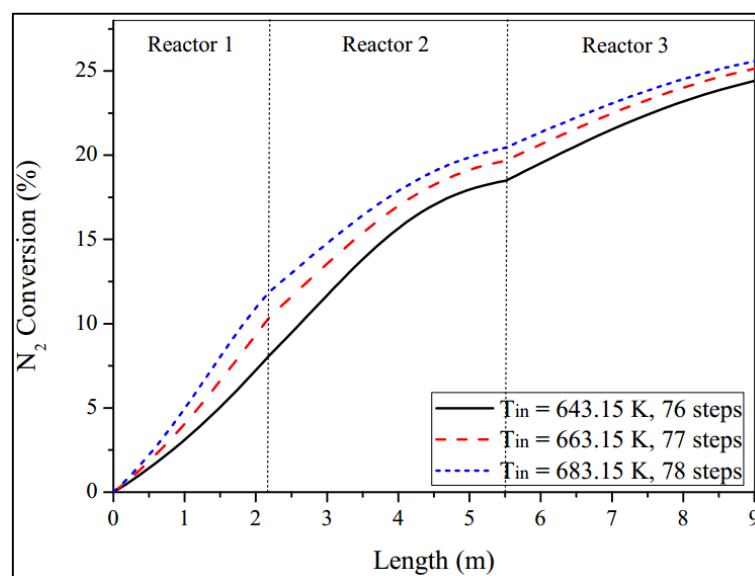
Figure 5.12. Conversion profiles in beds (Tin = 643.15 K, 663.15 K and 683.15 K).

In Figure 5.12, it is noted that larger inlet temperatures give higher N_2 conversions. However, a high T_{in} does not guarantee to elevate conversions, because the reaction is exothermic. After all, the reaction is reversible, and high temperatures provide low equilibrium conversion. Moreover, the biggest rise in conversions occurs in the first bed. It can be seen that

the growth of conversion between interval of 683.15 K and 663.15 K is smaller than 663.15 K and 643.15 K. Therefore, there is a limit to the T_{in} value.

Finally, in Figure 5.13, the effectiveness factor profiles are given. As inlet temperature increases, η factor also increases. This occurs due to a higher reaction rate. Moreover, the first reactor presents the smaller values of η. After all, the overall conversion is lower in first reactor.
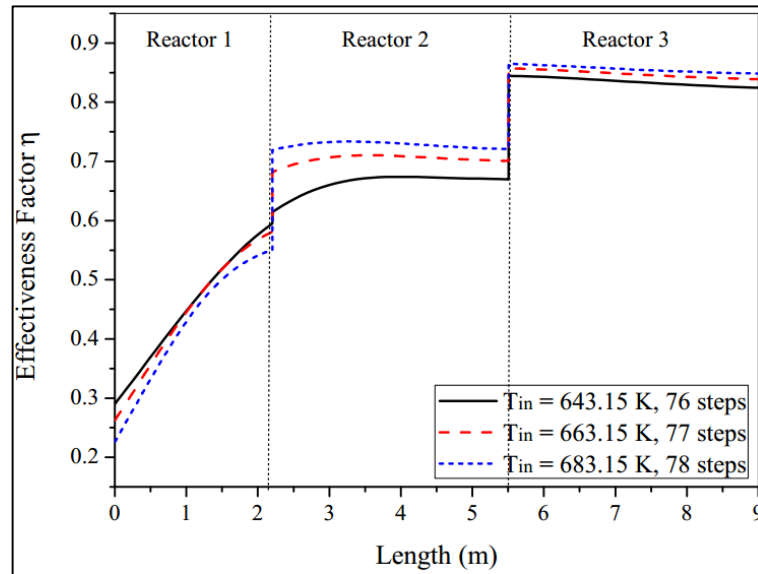
Figure 5.13. Effectiveness factor profiles in beds (Tin = 643.15 K, 663.15 K and 683.15 K).

5.4.1.2 Effect of inlet pressure P_{in}

The pressure operation in adiabatic reactors is also important. Even with an elevated rate, high pressures provide more energy release, raising temperature in the reactor. Therefore, adiabatic converters do not operate at maximum pressure. In this section, the dimension of the reaction system is the same as for Figure 5.9. The parameters for inlet pressure variation are given in Table 5.9.

Table 5.9. Parameters for inlet pressure variation in the adiabatic model (150 atm, 225 atm and 300 atm).

Constraints for adiabatic reactor simulation P_{in_1}					
$T_{in}(K) - 1st\ bed$	663.15	$y_{N_2\,in}$	0.22	$y_{CH_4\,in}$	0.045
$T_{in}(K) - 2nd\ bed$	693.15	$y_{H_2\,in}$	0.66	$y_{Ar\,in}$	0.045
$T_{in}(K) - 3rd\ bed$	683.15	$y_{NH_3\,in}$	0.03	$\dot{m}(kg/s)$	30.0

The temperature profiles along the beds are expressed in Figure 5.14. As inlet pressure increases, the temperature along the beds also rises. After all, more pressure promotes higher values for rate in the kinetic expression. Moreover, at 300 atm, the maximum temperature reaches 546 ℃, which exceeds the limit of iron catalyst (530 ℃). Therefore, at high pressures, the reactors must have smaller lengths (especially in the first bed), in order to prevent temperature rises. On the other side, the smaller P_{in} value (150 atm) gives smooth temperature profiles. In these situations, the reactor extent can be larger.
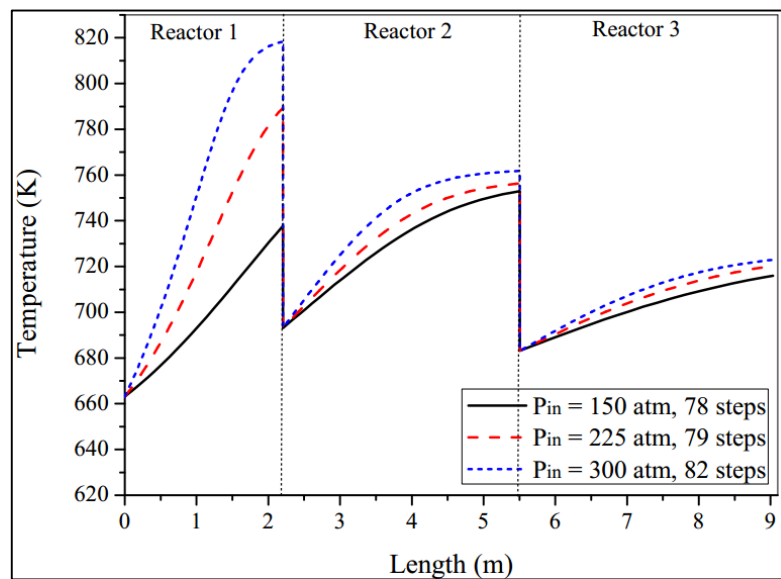
Figure 5.14. Temperature profiles in beds (Pin = 150 atm, 225 atm and 300 atm).

However, the opposite occurs in the pressure profiles. At smaller pressure P_{in} value (150 atm), the pressure loss presents the highest value (6.5 %). It occurs because with minor pressure, the fluid has less energy to flow, causing larger pressure loss. However, in biggest P_{in} value (300 atm), the pressure loss is 1.6 % because more compression makes gas flow with less pressure drop. Therefore, as pressure loss does not exceed the limit of 10 %, the profiles are not exposed.

The conversion profiles along the beds show a similar profile to temperature tendency, as expressed in Figure 5.15. There are big changes in conversion according to the P_{in} value. The highest conversion occurs at the pressure of 300 atm (about 44 %), because the reaction rate is higher than at other pressures. However, the temperature overcomes the limit of the catalyst. The pressure of 150 atm gives 24 % conversion, due to small rates. Finally, the pressure of 225 atm gives 33 % conversion and does not surpass the temperature value. Therefore, the intermediate pressure of 225 atm is better for this configuration.
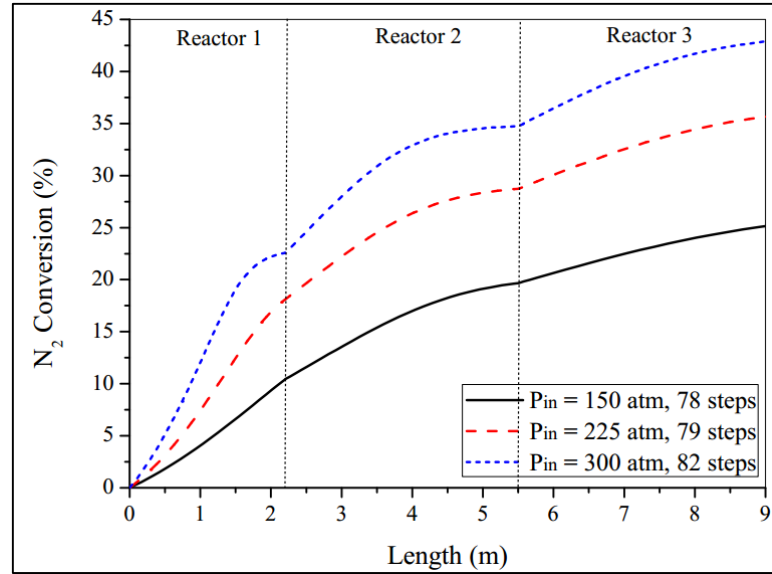
Figure 5.15. Conversion profiles in beds (Pin = 150 atm, 225 atm and 300 atm).

To summarize this section, the effectiveness factor η profiles are given in Figure 5.16.
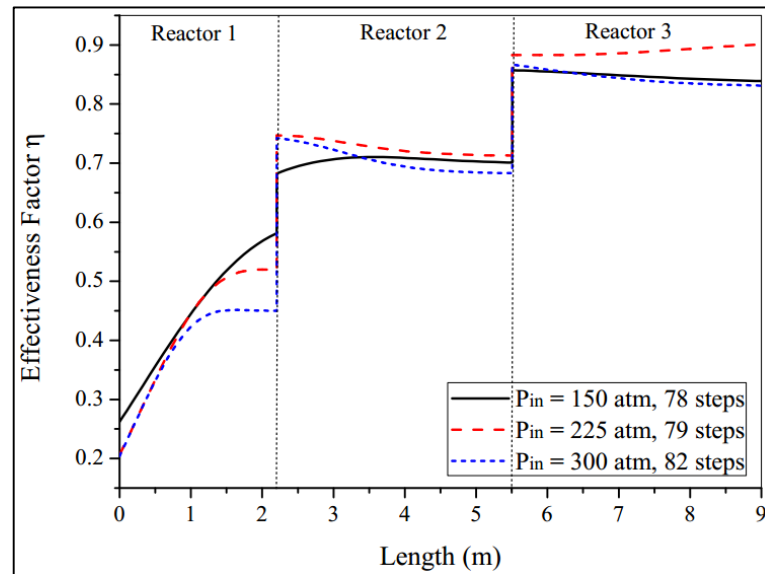
Figure 5.16. Effectiveness factor η profiles in beds (Pin = 150 atm, 225 atm and 300 atm).

A higher pressure makes η decrease, even raising the reaction rate. It happens because η computes diffusional resistances inside catalyst particles. Therefore, as pressure increases, the diffusion coefficient decreases. For this reason, when $P_{in} = 300\ atm$, η is lower than for the other cases in the three reactors. However, for $P_{in} = 225\ atm$, this factor is the highest in the 2nd and 3rd reactors, but not in the first. It occurs because pressure increase in the 1st reactor is higher when $P_{in} = 225\ atm$ than $P_{in} = 150\ atm$. Therefore, as temperature increases, η decreases. Moreover, the conversion is low in the first converter when $P_{in} =$

150 atm, then η becomes low in the other converters. It is important to note that as pressure increases, the reaction rate also increases, however the mass diffusivity decreases. Therefore, there is a balance between the pressure of operation and the limitation of mass transfer in ammonia reactor.

5.4.1.3 Effect of inlet NH₃ molar fraction yNH3ₙ

Besides temperature and pressure, another important variable for this converter is NH₃ content in the inlet stream. All the compositions used in simulations are summarized in Table 5.10. The dimensions and temperature between reactors were maintained.

Table 5.10. Parameters for inlet NH₃ molar fraction in adiabatic model (0.01, 0.03 and 0.05).

Constraints for adiabatic simulation $y_{NH_3\,in}$					
$y_{N_2\,in\,1}$	0.22	$y_{N_2\,in\,2}$	0.22	$y_{N_2\,in\,3}$	0.22
$y_{H_2\,in\,1}$	0.66	$y_{H_2\,in\,2}$	0.66	$y_{H_2\,in\,3}$	0.66
$y_{NH_3\,in\,1}$	0.01	$y_{NH_3\,in\,2}$	0.03	$y_{NH_3\,in\,3}$	0.05
$y_{CH_4\,in\,1}$	0.055	$y_{CH_4\,in\,2}$	0.045	$y_{CH_4\,in\,3}$	0.035
$y_{Ar\,in\,1}$	0.055	$y_{Ar\,in\,2}$	0.045	$y_{Ar\,in\,3}$	0.035
$T_{in\,1}(K)$	663.15	$T_{in\,2}(K)$	693.15	$T_{in\,3}(K)$	683.15

The effect of $y_{NH_3\,in}$ in temperature profiles is given in Figure 5.17.
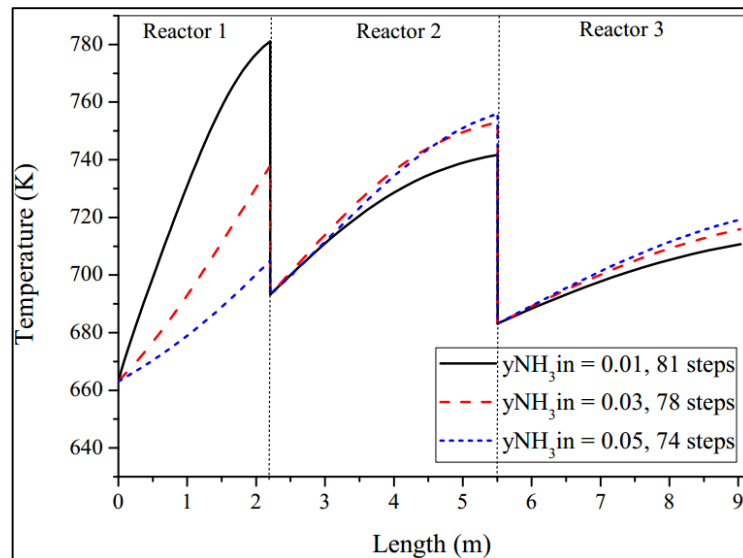
Figure 5.17. Temperature profiles in beds (yNH3in = 0.01, 0.03 and 0.05).

Smaller $y_{NH_3\,in} = 0.01$ provide high rates, making temperature higher especially in the first bed. Therefore, in the next beds, less nitrogen is available to be converted. Therefore, the profiles in the second and third beds are less than y_{NH_3} of 0.03 and 0.05. This impact in the first bed probably has effects on the conversions.

As the reaction rate in the first bed is larger, it is expected that pressure drop in $y_{NH_3\,in} = 0.01$ overcame the other molar fractions. This is given in Figure 5.18. However, $y_{NH_3\,in} = 0.03$ and $y_{NH_3\,in} = 0.05$ give more pressure drop in the final bed. It happens because much N_2 is consumed, decreasing the rate in the second and third beds.
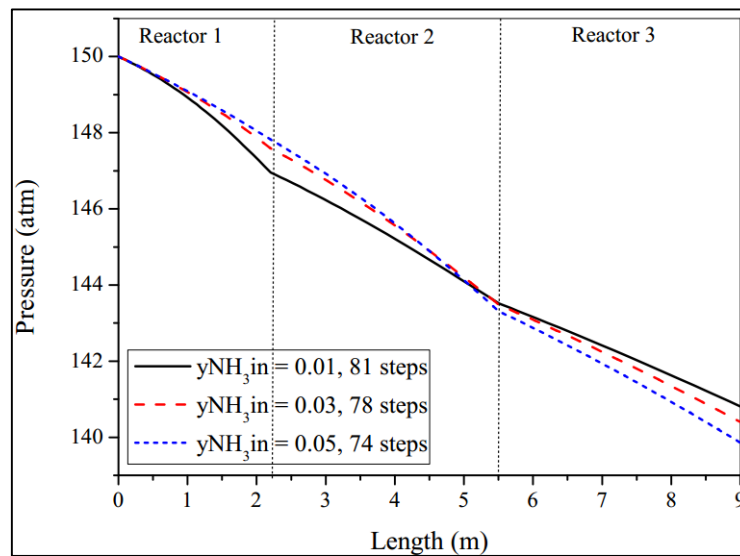
Figure 5.18. Pressure profiles in beds (yNH3in = 0.01, 0.03 and 0.05).

Furthermore, the conversion profiles are given in Figure 5.19.
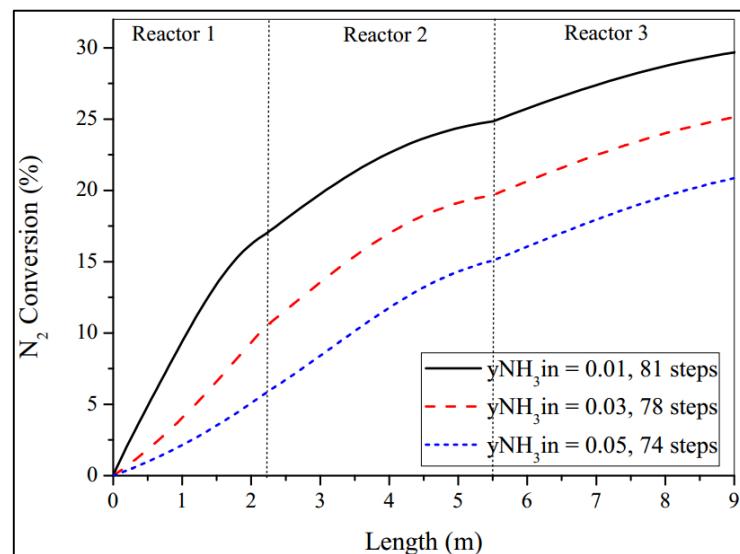
Figure 5.19. Conversion profiles in beds (yNH3in = 0.01, 0.03 and 0.05).

We can observe that molar fraction $y_{NH_3\,in} = 0.01$ gives the largest conversion profile (next to 30 %), due to an elevated rate value. On the other hand, $y_{NH_3\,in} = 0.05$ provides a final conversion close to 20 %. However, there is a risk of operating at low values of $y_{NH_3\,in}$, due to the dangerous temperature profile in Figure 5.17.

To summarize, the effectiveness factor η profiles are given in Figure 5.20. It can be seen that low molar fractions give a saturation in the 1st bed η profile. It occurs due to a high reaction rate, which provides elevated conversions. However, in subsequent reactors, η is almost constant. Therefore, it shows the difficulty of conversion in the 2nd and 3rd reactors when $y_{NH_3\,in} = 0.01$.
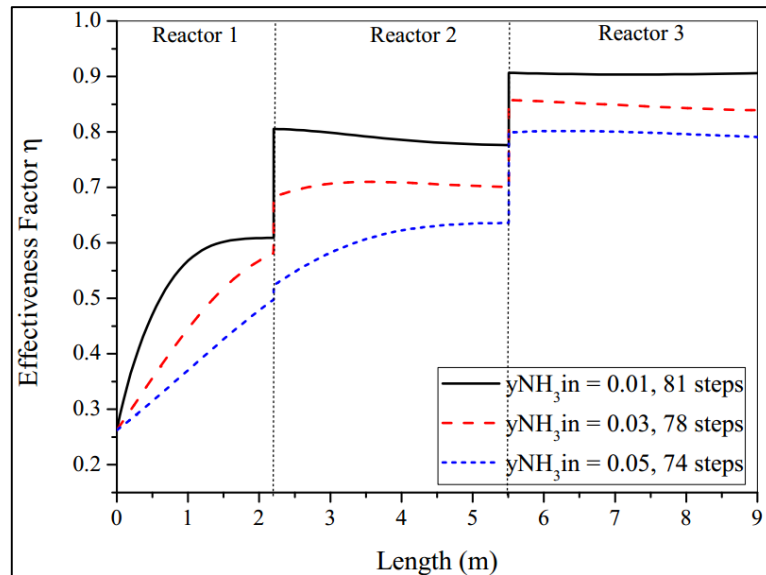
Figure 5.20. Effectiveness factor η profiles in beds (yNH3in = 0.01, 0.03 and 0.05).

5.4.2 Autothermal Model

The main advantage of the autothermal model compared to the adiabatic case is the heat removal along the reactor. However, the temperature cannot exceed the limit of 810 K, which is the limit of many iron catalysts. A countercurrent autothermal reactor with the same autothermal volume of Section 5.3.2 is used in all this analysis.

5.4.2.1 Effect of inlet temperature T_{in}

In the first analysis, the values of inlet temperature are 653.15 K, 673.15 K and 693.15 K. These values are equivalent to 380 ºC, 400 º C and 420 ºC, respectively. Moreover,

the dimensions of reactor used are given in Table 5.11. The catalyst parameters are given in Table 4.12.

Table 5.11. Parameters for inlet temperature variation in autothermal model (653.15 K, 673.15 K and 693.15 K).

Constraints for countercurrent simulation			
$y_{N_2\,in}$	0.22	n_t	250
$y_{H_2\,in}$	0.66	$D_r(m)$	1.5
$y_{NH_3\,in}$	0.03	$L_r(m)$	2.5
$y_{CH_4\,in}$	0.045	$a'(m^2/m)$	11.78
$y_{Ar\,in}$	0.045	$U\,(W/m^2.K)$	650
$P_{in}(atm)$	225	$\dot{m}(kg/s)$	6

The inlet temperature profiles for reactant gas are given in Figure 5.21. As inlet temperature rises, the maximum temperature reached also increases. Moreover, the length which presents the largest temperature changes. For T_{in} = 653.15 K, the length is 0.9 m, while for T_{in} = 693.15 K, the value is 0.6 m. It occurs because at the highest temperatures, the rate value increases, releasing more energy.
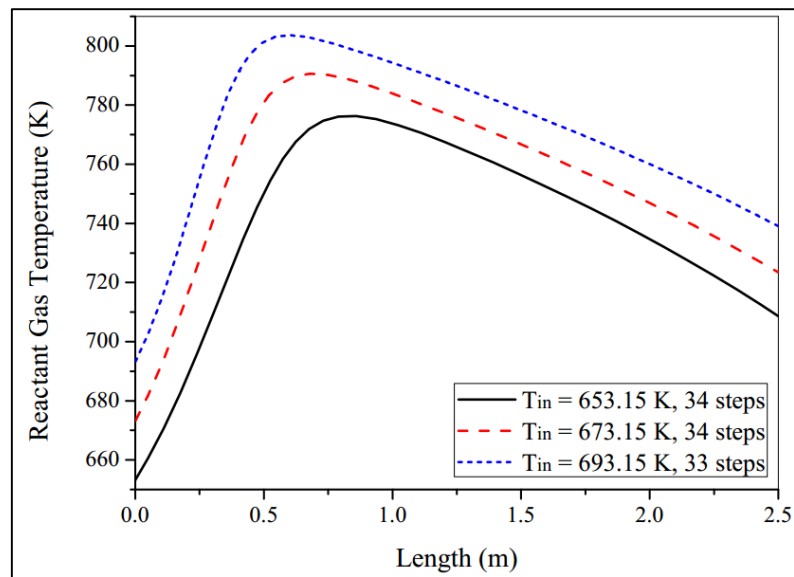
Figure 5.21. Reactant gas temperature profile in autothermal converter (Tin = 653.15 K, 673.15 K and 693.15 K).

Another important measure is the cooling gas temperature, which flows countercurrent to the reactant gas. The profiles are shown in Figure 5.22. All the three profiles give similar variations. The only difference noted is in temperature at the top of the reactor. With smaller T_{in} values, cooling gas temperature at the end of reactor decreases.
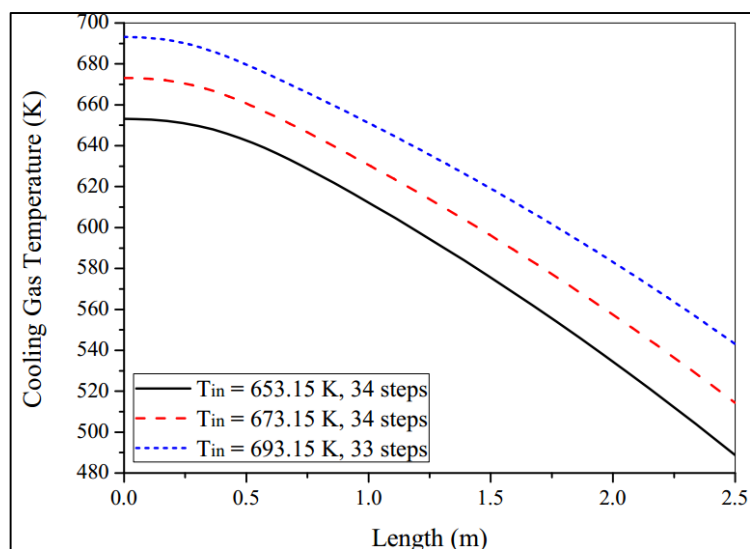
Figure 5.22. Cooling gas temperature profiles in autothermal converter (Tin = 653.15 K, 673.15 K and 693.15 K).

The pressure along the converter presents the same behavior as in the adiabatic model. When T_{in} increases, the pressure loss also increases, because more energy is released. Therefore, viscosity rises and dP/dL in the Ergun Equation increases. This is given in Figure 5.23.
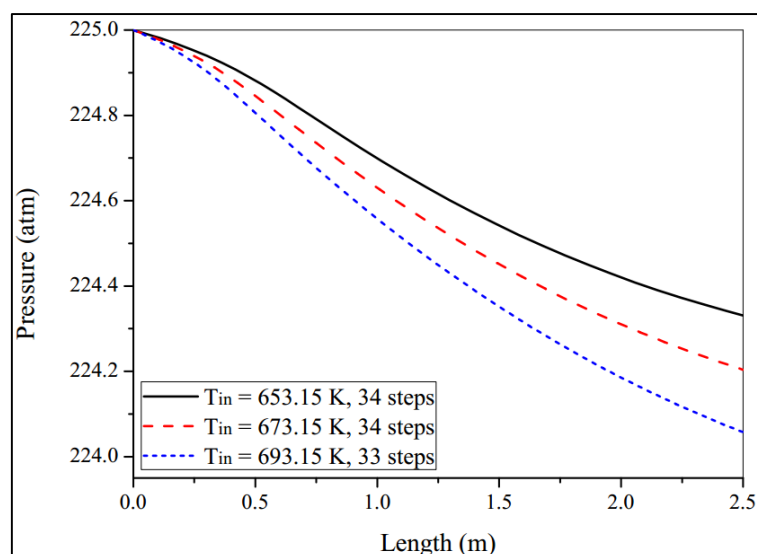
Figure 5.23. Pressure profiles in autothermal converter (Tin = 653.15 K, 673.15 K and 693.15 K).

The conversion profile is also calculated depending on T_{in} values. The results are summarized in Figure 5.24. Even with larger rates, the largest T_{in} values provide low conversions. It occurs because the equilibrium conversion decreases when temperature rises (exothermic reaction). Therefore, after the maximum value of T_{in}, the smaller temperatures present larger changes in conversion. However, if T_{in} decreases too much, a kinetic limitation will happen, because the rate will be very slow. This analysis is completed in Figure 5.26.
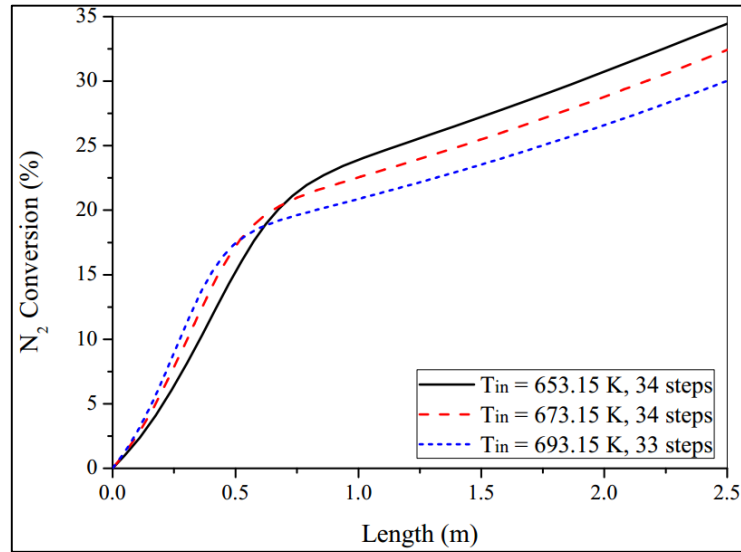
Figure 5.24. Conversion profiles in autothermal converter (Tin = 653.15 K, 673.15 K and 693.15 K).

The conversion is also influenced by effectiveness factor η. The profiles of η are given in Figure 5.25.
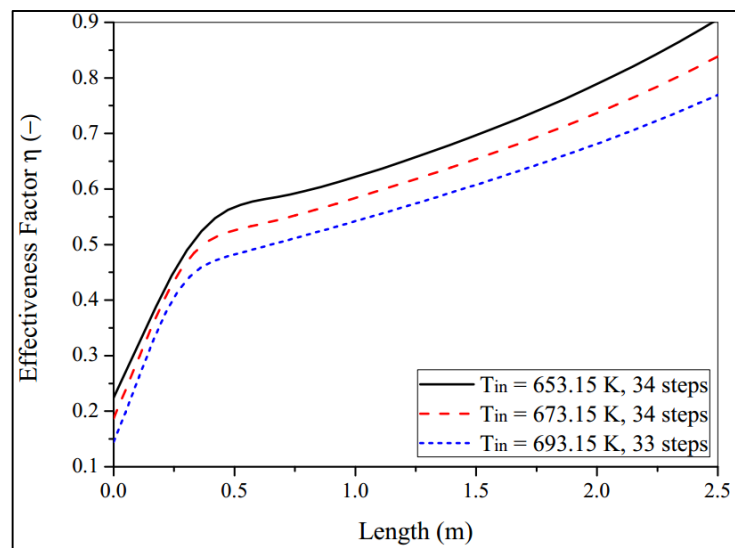
Figure 5.25. Effectiveness factor η profiles in autothermal converter (Tin = 653.15 K, 673.15 K and 693.15 K).

A higher inlet temperature provides smaller values of η. It happens because the reaction is exothermic, decreasing equilibrium conversion. In the three cases, the effectiveness factor presents a rapid change at the beginning of reactors. This point is equivalent to the maximum temperature region. After this point, η always increases, making mass transfer less difficult along the converter.

Moreover, the output conversion in function of inlet temperature is given in Figure 5.26.
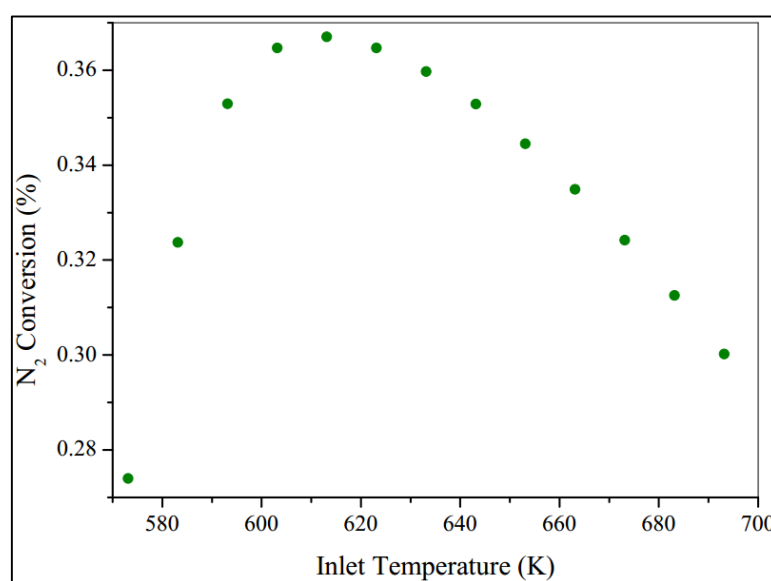
Figure 5.26. Final conversion in autothermal reactor varying with inlet temperature.

It can be seen that the temperature of 615 K (approximately 340 ℃) gives the maximum conversion for the converter. Therefore, temperatures lower than 615 K provide high equilibrium conversions, but low reactions rates. The opposite is always verified. To summarize, even in an autothermal reactor, there are limits to inlet temperature for the operation.

An inversion point of operation is also detected in the outlet temperature, as given in Figure 5.27. In the region of $T_{in} = 615\ K$, the outlet temperature changes the saturation pattern to a linear variation. Moreover, a higher output temperature complicates the cooling and separation system after the reactor. Therefore, the previous point of higher conversion also gives a good outlet temperature.
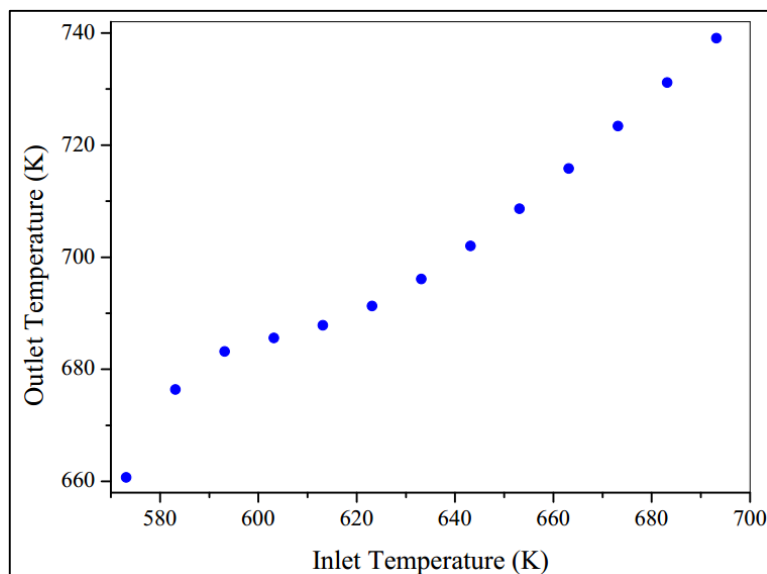
Figure 5.27. Reactant gas outlet temperature in autothermal reactor varying with inlet temperature.

Finally, the maximum temperature along the converter is given in Figure 5.28. As inlet temperature increases, it was predicted that the maximum temperature in the autothermal reactor would also rise. The saturation pattern at the end of Figure 5.28 occurs due to smaller equilibrium conversions.
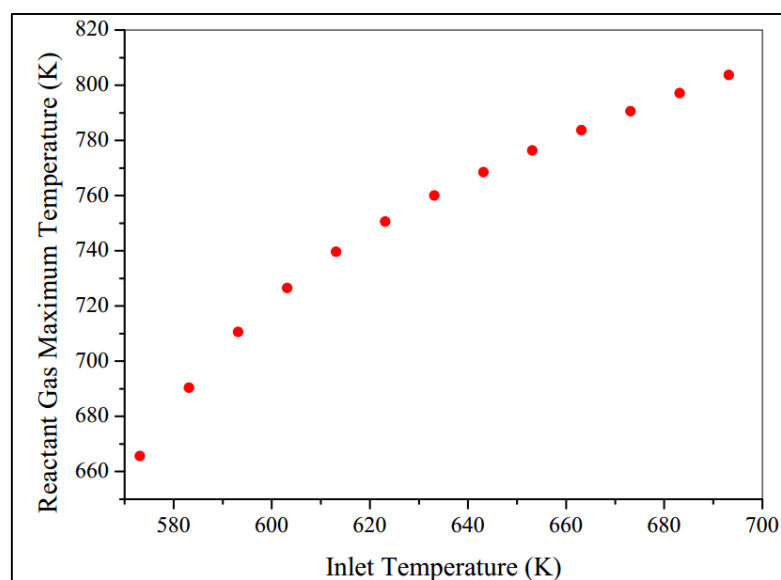
Figure 5.28. Reactant gas maximum temperature in autothermal reactor varying with inlet temperature.

5.4.2.2 Effect of inlet pressure P_{in}

The dimensions of the reactor are the same as in the previous section. The only changes are in inlet temperature (613.15 K) and in pressure variations (150, 225 and 300 atm). Additional data is given in Table 5.12.

Table 5.12. Parameters for inlet pressure variation in the autothermal model (150, 225 and 300 atm).

Constraints for countercurrent simulation			
$y_{N_2\,in}$	0.22	n_t	250
$y_{H_2\,in}$	0.66	$D_r\,(m)$	1.5
$y_{NH_3\,in}$	0.03	$L_r\,(m)$	2.5
$y_{CH_4\,in}$	0.045	$a'\,(m^2/m)$	11.78
$y_{Ar\,in}$	0.045	$U\,(W/m^2.K)$	650
$T_{in}(K)$	613.15	$\dot{m}(kg/s)$	6

The temperature profile of reactant gas is provided in Figure 5.29. At high pressures, the activities are larger. It makes reaction rates increase. Therefore, the temperature presents larger values in P_{in} = 300 atm. Furthermore, high pressures make profiles steeper, reducing the places where temperature is maximum. To summarize, as pressure increases, the number of iterations of method also increases. It occurs because at higher pressures the differential equations (especially for temperature) became more nonlinear, making truncation errors higher.

Similar dynamics are observed in cooling gas temperature profiles, as given in Figure 5.30. With higher temperatures, the gas needs to exchange more energy. Therefore, the ΔT between inlet and outlet of reactor is higher in P_{in} = 300 atm. Moreover, for this reason, the top temperature was smaller in P_{in} = 150 atm.
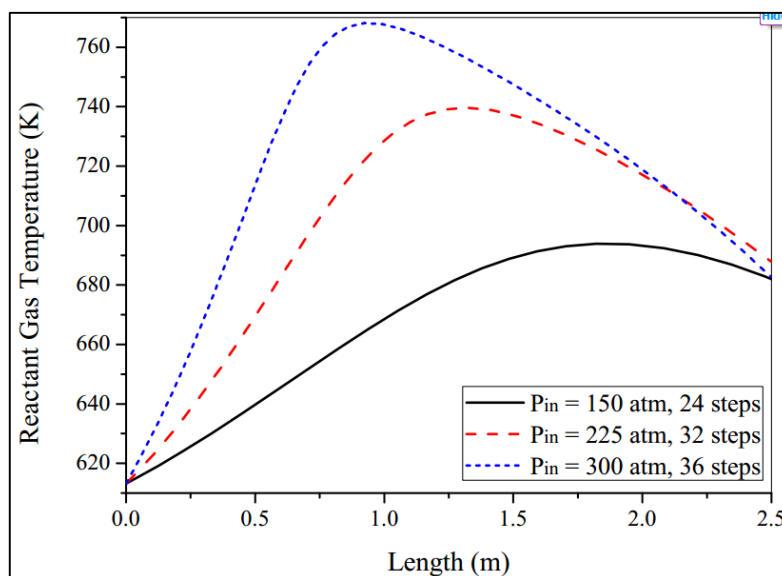
Figure 5.29. Reactant gas temperature profiles in autothermal converter (Pin = 150 atm, 225 atm and 300 atm).
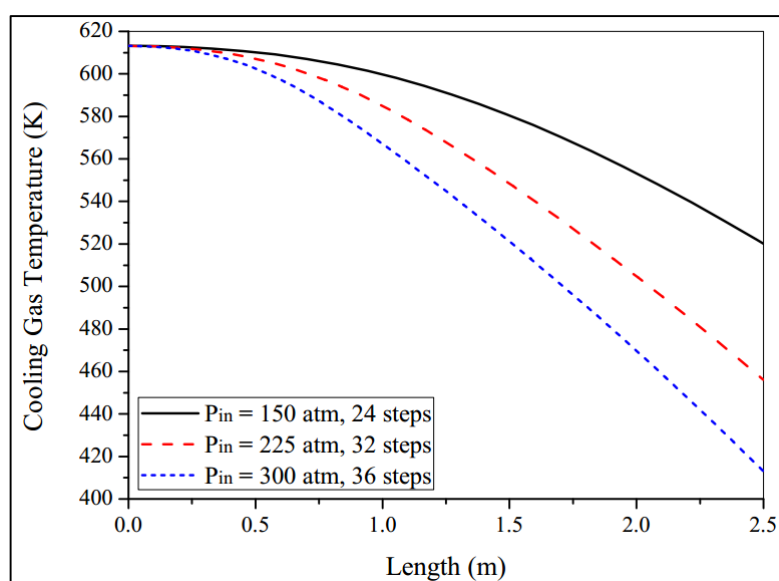
Figure 5.30. Cooling gas temperature profiles in autothermal converter (Pin = 150 atm, 225 atm and 300 atm).

In Figure 5.29, as pressure increases, the temperatures inside the reactor also rises, because of the rise in the reaction rate. Therefore, we also could expect elevated conversions for higher pressures. It is confirmed in Figure 5.31. At 300 atm, the conversion of nitrogen is up to 45 %. Even with this elevated conversion at 300 atm, the temperature does not surpass the limit of the catalyst. However, this operation is risker because of multiple steady-states (VAN HEERDEN, 1953).
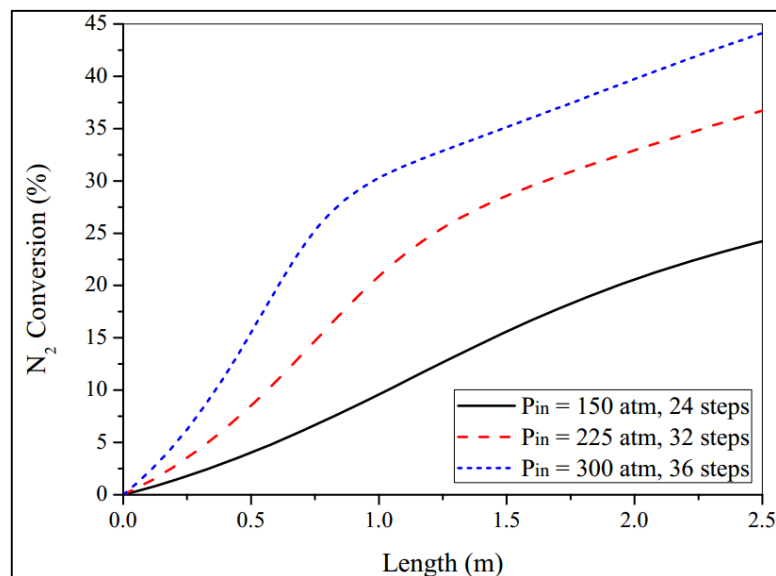
Figure 5.31. Conversion profiles in autothermal converter (Pin = 150 atm, 225 atm and 300 atm).

Another surprising result was the effectiveness factor η profile along the autothermal converter. More information is given in Figure 5.32.
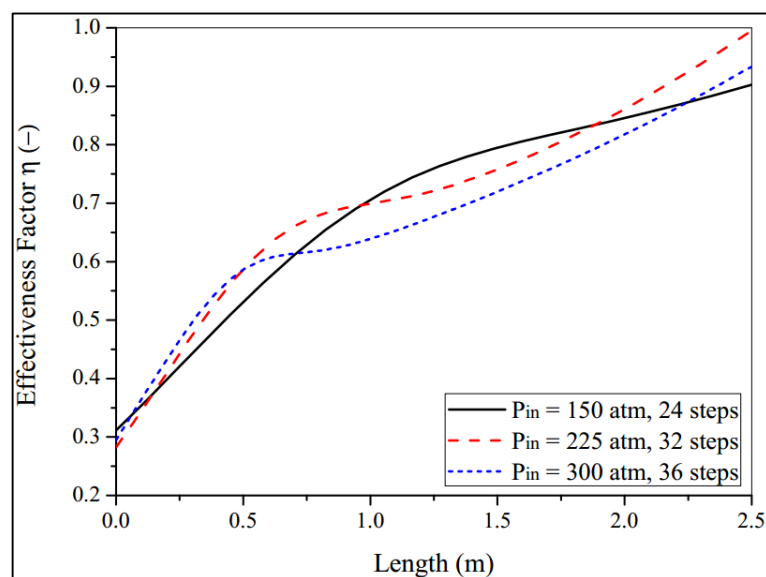
Figure 5.32. Effectiveness factor η profiles in autothermal converter (Pin = 150 atm, 225 atm and 300 atm).

The maximum value of η is reached at a pressure of 225 atm. However, it is expected that the highest values are found at 300 atm. However, the temperature growth at 300 atm makes the reaction less effective, making η increase less than 250 atm. The difference between both pressures is noted after the bend of Figure 5.32 (maximum temperature region).

To summarize, the pressure profiles are not presented due to differences in magnitude values. Moreover, the highest value of pressure loss was less than 1 % (150 atm case).

5.4.2.3 Effect of inlet NH$_3$ molar fraction yNH3$_{in}$

As ammonia is the main component of the reaction system, its variation is important. Moreover, small changes in the NH$_3$ molar fraction at the reactor entrance can make the rate explode, because a_{NH_3} is in denominator (see Equation (3.22)). An explosion in the reaction rate can also lead to numerical problems.

For this analysis, the same molar proportion of the previous cases between N$_2$ and H$_2$ is maintained, that is, 3. Therefore, when NH$_3$ content is varied, the molar difference is accounted for by inert (CH$_4$ and Ar). More information is shown in Table 5.13.

Table 5.13. Parameters for inlet NH$_3$ molar fraction variation in the autothermal model (0.01, 0.03 and 0.05).

Constraints for autothermal simulation $y_{NH_3\,in}$					
$y_{N_2\,in\,1}$	0.22	$y_{N_2\,in\,2}$	0.22	$y_{N_2\,in\,3}$	0.22
$y_{H_2\,in\,1}$	0.66	$y_{H_2\,in\,2}$	0.66	$y_{H_2\,in\,3}$	0.66
$y_{NH_3\,in\,1}$	0.01	$y_{NH_3\,in\,2}$	0.03	$y_{NH_3\,in\,3}$	0.05
$y_{CH_4\,in\,1}$	0.055	$y_{CH_4\,in\,2}$	0.045	$y_{CH_4\,in\,3}$	0.035
$y_{Ar\,in\,1}$	0.055	$y_{Ar\,in\,2}$	0.045	$y_{Ar\,in\,3}$	0.035
$T_{in}(K)$	613.15	$P_{in}(atm)$	225	$\dot{m}(kg/s)$	6.0
$U\,(W/m^2.K)$	650	$a'(m^2/m)$	11.78	$L_r(m)$	2.5

Moreover, other parameters such as the number of tubes and reactor diameter are also maintained. The effect of the ammonia molar fraction in reactor temperature is given in Figure 5.33. Observing Figure 5.33, we note that a smaller $y_{NH_3\,in}$ value provides a larger rate. It changes the maximum temperature value and its location in the reactor. Furthermore, a high value of y_{NH_3} makes difficult the conversion along the reactor, due to smaller rates. Therefore, the temperature presents a smoother profile in $y_{NH_3\,in} = 0.05$. Moreover, with small values of $y_{NH_3\,in}$, the method needs more iterations to converge, because of the rise in nonlinearity.
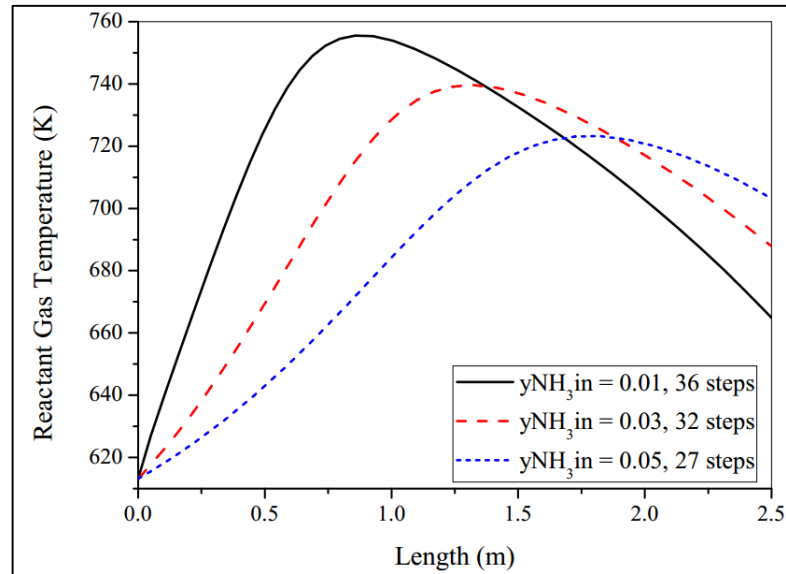
Figure 5.33. Reactant gas temperature profiles in autothermal reactor (yNH3in = 0.01, 0.03 and 0.05).

The same analogy can be applied to the cooling gas temperature, which is expressed in Figure 5.34. As $y_{NH_3\ in}$ = 0.01 provides a higher rate, a higher temperature difference must be reached. On the other hand, $y_{NH_3\ in}$ = 0.05 presents smaller rates, leading to reduced values of temperature at the top of the reactor L = 2.5 m.
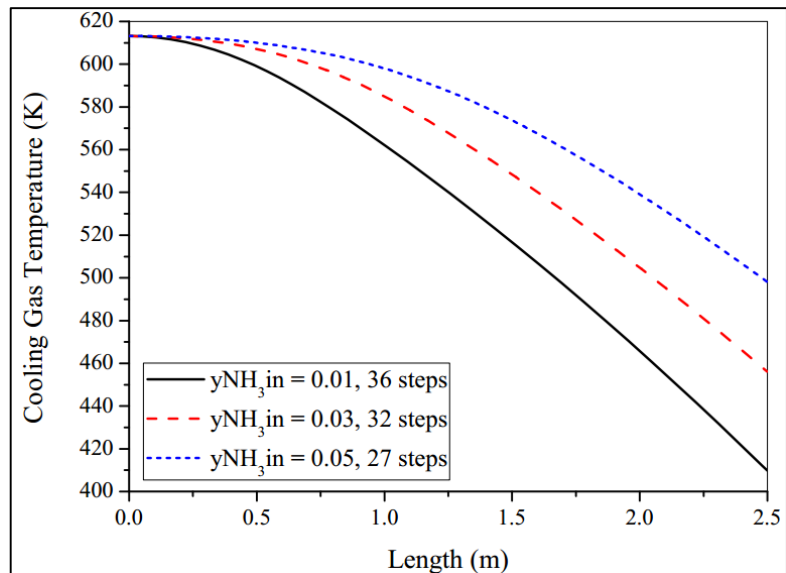
Figure 5.34. Cooling gas temperature profiles in autothermal reactor (yNH3in = 0.01, 0.03 and 0.05).

Moreover, the pressure drop along the converter is negligible, as expressed in Figure 5.35. The maximum value is 0.5 %, which happens in $y_{NH_3\ in}$ = 0.01, due to a greater

rate value, which increases temperature and gas viscosity. However, the results in Figure 5.35 show that pressure drop is not a problem in autothermal reactors, because mass flow is normally smaller than in adiabatic beds and the flow is divided into tubes.
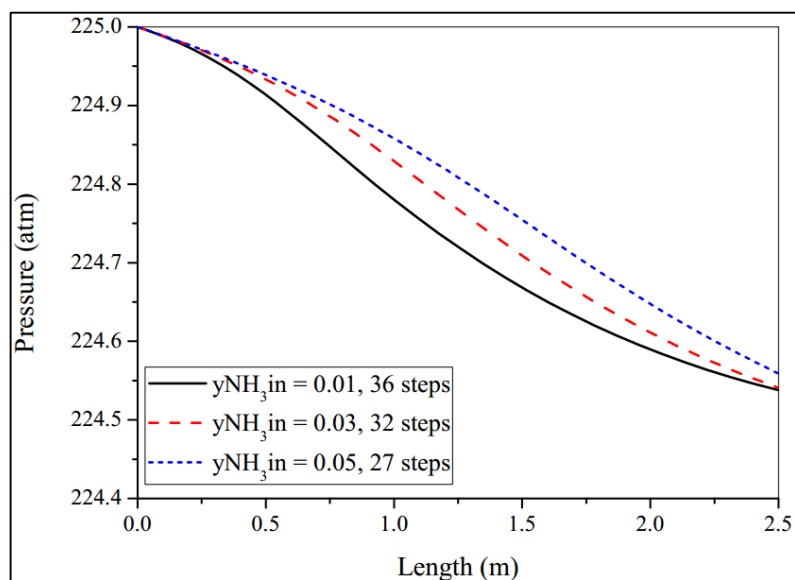
Figure 5.35. Pressure profiles in autothermal reactor (yNH3in = 0.01, 0.03 and 0.05).

Furthermore, the conversion profile depending on NH_3 molar content is given in Figure 5.36.
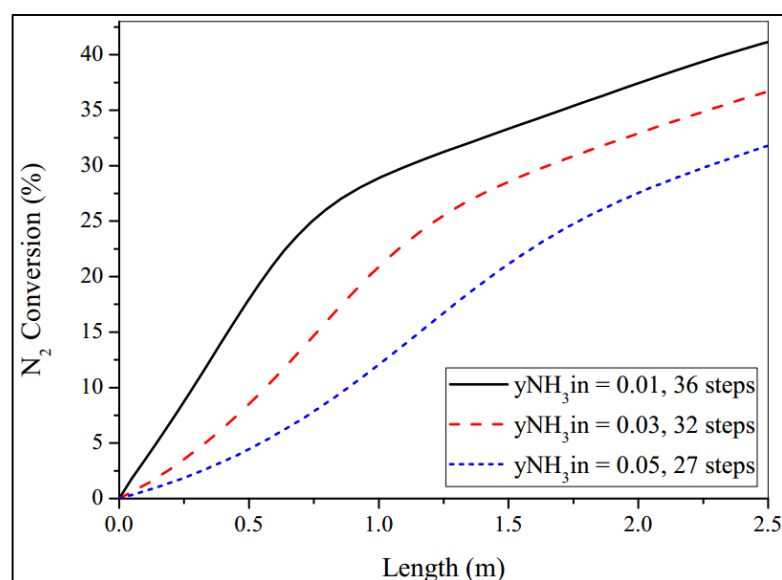
Figure 5.36. Conversion profiles in autothermal reactor (yNH3in = 0.01, 0.03 and 0.05).

All the profiles showed similar tendencies. However, a smaller $y_{NH_3 \, in}$ provides a larger conversion profile. Therefore, if the reactor operates with $y_{NH_3 \, in}$ = 0.05, a larger converter is required, because the residence time has to be raised. On the other hand, a small

NH_3 content in the inlet stream makes the operation more difficult due to temperature elevation, at the cost of higher conversions.

To summarize, the effectiveness factor profiles are given in Figure 5.37.
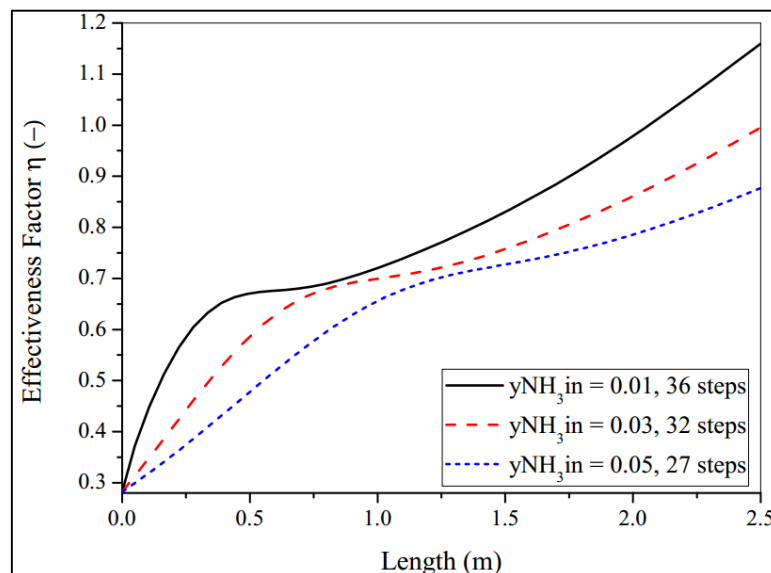
Figure 5.37. Effectiveness factor η profiles in autothermal reactor (yNH3in = 0.01, 0.03 and 0.05).

In smaller molar fractions, the η factor rises after the maximum temperature point. However, the method predicts higher values than 1 at the end of reactor. It can be considered an incorrect prediction, once all the heat is released. Moreover, as conversion rises too much in a small space (Figure 5.36), the correlation for η factor could have predicted wrong values.

5.4.2.4 Effect of heat transfer coefficient U

The heat transfer coefficient is a parameter which supports the energy removal along the reactor. At high values of U, the cooling tubes remove more heat, making temperature profiles smoother. On the other hand, the reactor removes less energy, approaching an adiabatic behavior. Therefore, this parameter is important for autothermal operations.

In this section, some values of U will be varied. The consequences in conversion, temperatures and pressure are monitored. The parameters for simulation are given in Table 5.14. All the previous dimensions are preserved.

Table 5.14. Parameters for inlet temperature variation in autothermal model (450, 650 and 850 W/m².K).

Constraints for countercurrent simulation			
$y_{N_2\,in}$	0.22	n_t	250
$y_{H_2\,in}$	0.66	$D_r(m)$	1.5
$y_{NH_3\,in}$	0.03	$L_r(m)$	2.5
$y_{CH_4\,in}$	0.045	$a'(m^2/m)$	11.78
$y_{Ar\,in}$	0.045	$\dot{m}(kg/s)$	6
$P_{in}(atm)$	225	$T_{in}(K)$	613.15

The reactant gas temperatures profiles are given in Figure 5.38. Observing Figure 5.38, we note that the length in the reactor which presents the largest temperature does not change. However, the maximum temperature value changes for $U = 450$ W/m².K, the maximum T is 753 K, while for $U = 650$ W/m².K, T is 739 K. Moreover, another important value is the final value for the reactant gas at the end of the reactor. For $U = 450$ W/m².K, the final T value is 724 K and $U = 650$ W/m².K is 687 K. It takes place because a large U removes more energy in the reactor, decreasing temperature more rapidly. Therefore, a large modification of profile occurs changing the U value.
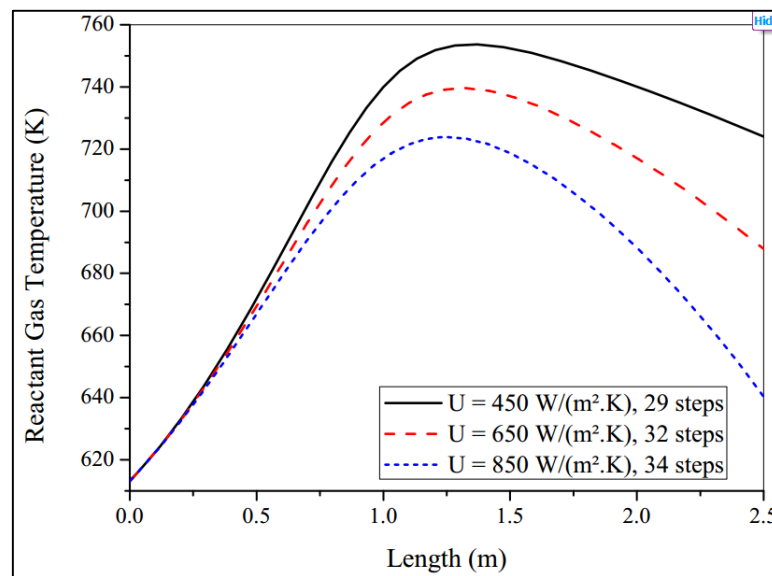
Figure 5.38. Reactant gas temperature profiles in autothermal reactor (U = 450, 650 and 850 W/m².K).

The same tendency happens for the cooling gas temperature, observing Figure 5.39. When U increases, the temperature at the top of the reactor decreases, because more heat needs to be exchanged in the same space. Moreover, as the U value increases, the derivative in T_g became higher (Equations (4.77) and (4.79)), raising nonlinearity. Therefore, more iterations need to be performed.
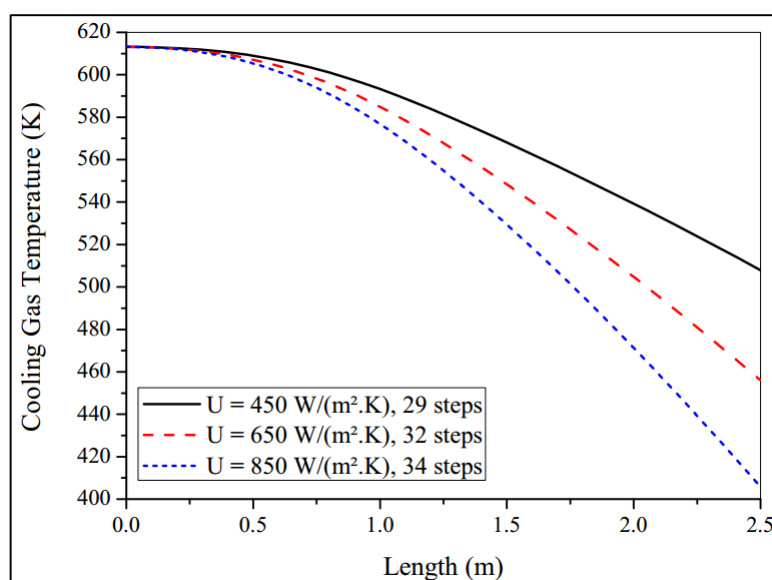
Figure 5.39. Cooling gas temperature profiles in autothermal reactor (U = 450, 650 and 850 W/m².K).

The pressure profile of the reactor is given in Figure 5.40. Again, the pressure drop is negligible, reaching the maximum of 0.30 % for U = 450 W/m².K. After all, when U decreases, more energy is released, making reaction rates higher.
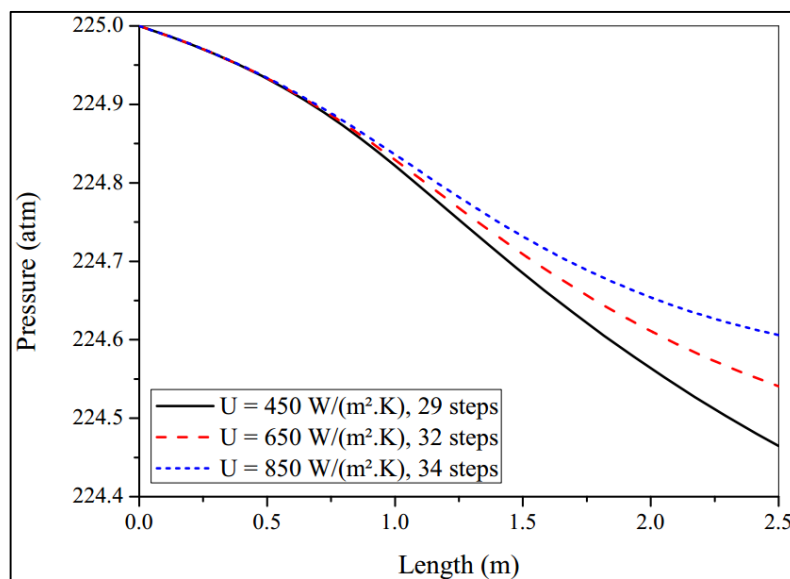
Figure 5.40. Pressure profiles in autothermal reactor (U = 450, 650 and 850 W/m².K).

Finally, the conversion profile is provided in Figure 5.41. When U increases, the final conversion also increases. It occurs because more energy is removed by the reaction, decreasing the speed of the reverse reaction. However, U cannot be raised too much, otherwise the rate would be very low.
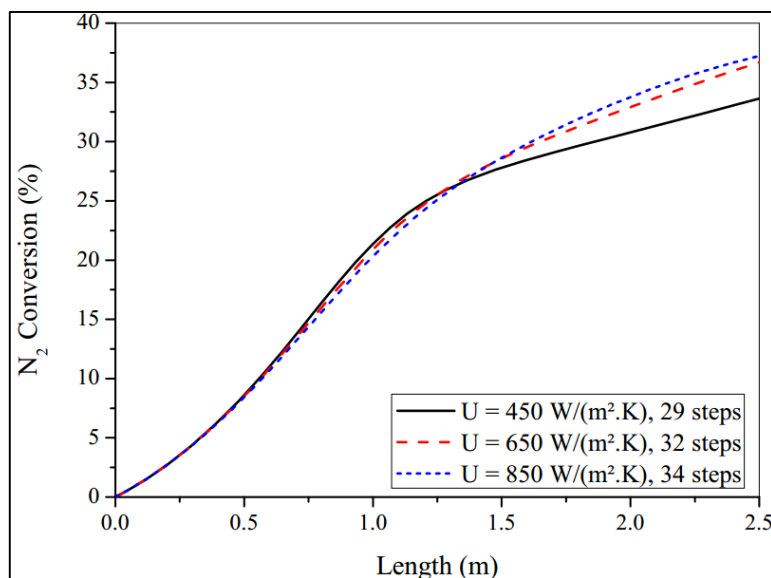
Figure 5.41. Conversion profiles in autothermal reactor (U = 450, 650 and 850 W/m².K).

The effectiveness factor η profiles are given in Figure 5.42. As U increases, the temperature decreases in the reactor, raising equilibrium conversion and η values. However, in $U = 850$ W/m².K, there are errors computing η (higher than 1).
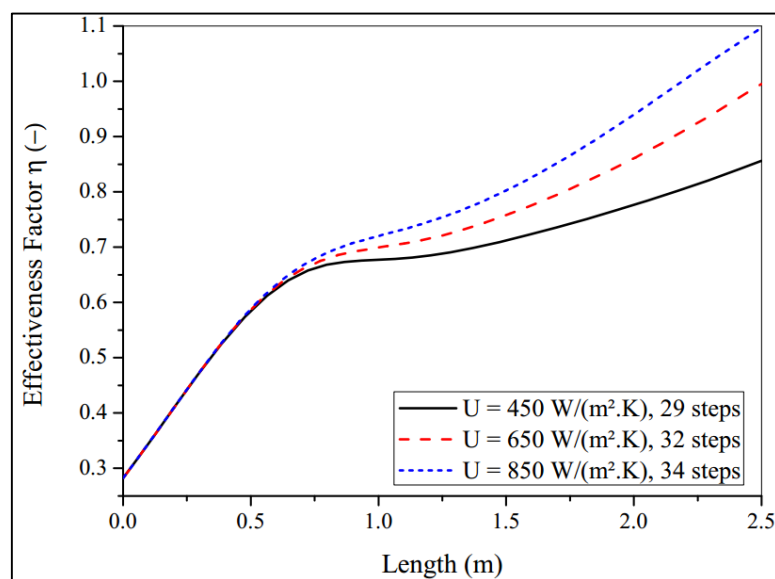
Figure 5.42. Effectiveness factor η profiles in autothermal reactor (U = 450, 650 and 850 W/m².K).

Finally, the values of outlet conversion, temperature and maximum temperature inside the converter are monitored with U variations. The conversion variation with U is shown in Figure 5.43. Low values of U provide low conversions, due to low equilibrium rates. However, when U values rise too much, the conversion decreases, because low rates occur.
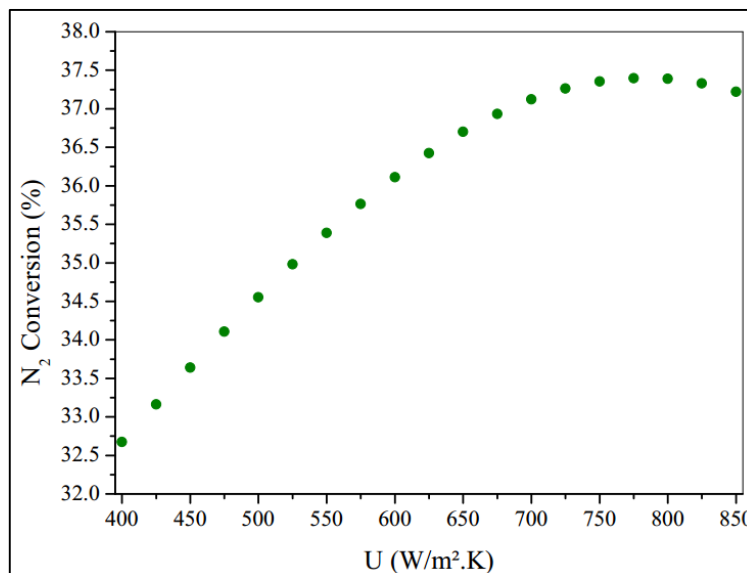
Figure 5.43. Conversion variation with heat transfer coefficient U.

Finally, the outlet temperature and maximum temperature inside the autothermal converter decreases linearly with U, as given in Figure 5.44 and Figure 5.45. After all, the heat removal rate is linear along the autothermal reactor.
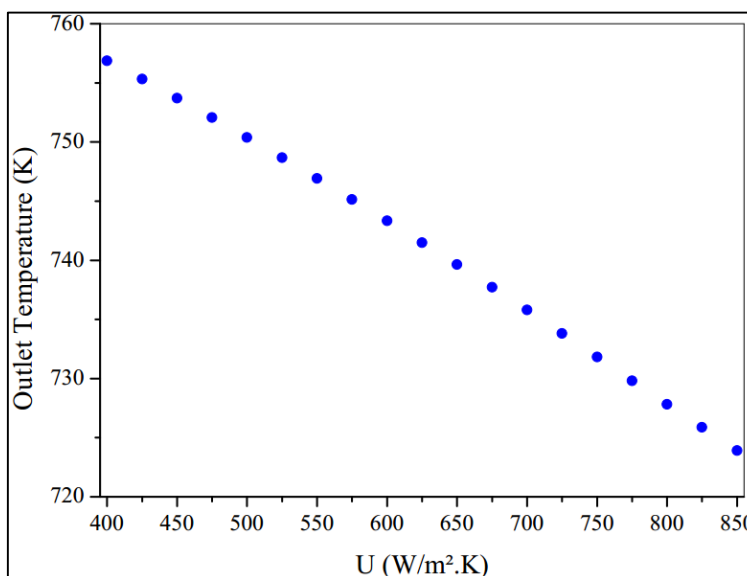
Figure 5.44. Outlet temperature variation with heat transfer coefficient U.
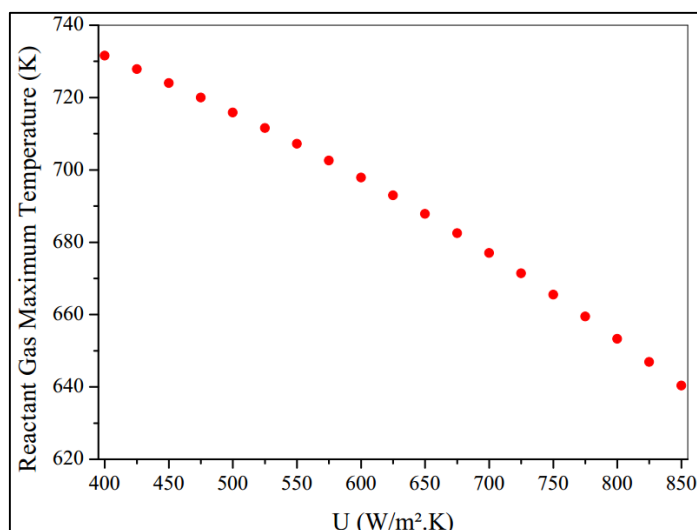
Figure 5.45. Maximum temperature in reactant gas with heat transfer coefficient U.

5.5 Mass Boundary Layer Analysis

In the previous sections, the pseudo-homogeneous approach was used. Therefore, it is supposed that no differences between the catalyst surface and bulk exist (in composition, temperature and pressure). In this investigation, an isothermal and isobaric catalyst particle is taken. However, the difference of concentration ΔC_i in NH$_3$ [mol/m^3], diffusivity coefficient D_{NH_3} [m^2/s], mass transfer coefficient k_c [m/s] and boundary layer thickness δ [m] are calculated. Therefore, the magnitude of errors compared to the pseudo-homogeneous approach can be seen. Only one adiabatic reactor and one autothermal converter are simulated.

5.5.1 Adiabatic Reactor (One Converter)

The parameters for adiabatic simulation are given in Table 5.15. The dimensions of the first bed are the same as Section 5.4.1.

Table 5.15. Parameters for boundary layer calculations in adiabatic model.

Constraints for adiabatic simulation $T_{in_1} = 643.15\ K$			
$P_{in}(atm)$	225	$y_{N_2\ in}$	0.22
$D_r(m)$	1.7	$y_{H_2\ in}$	0.66
$\dot{m}(kg/s)$	30.0	$y_{NH_3\ in}$	0.03
$y_{Ar\ in}$	0.045	$y_{CH_4\ in}$	0.045

Firstly, the variation of ΔC_i in NH$_3$ is given in Figure 5.46.
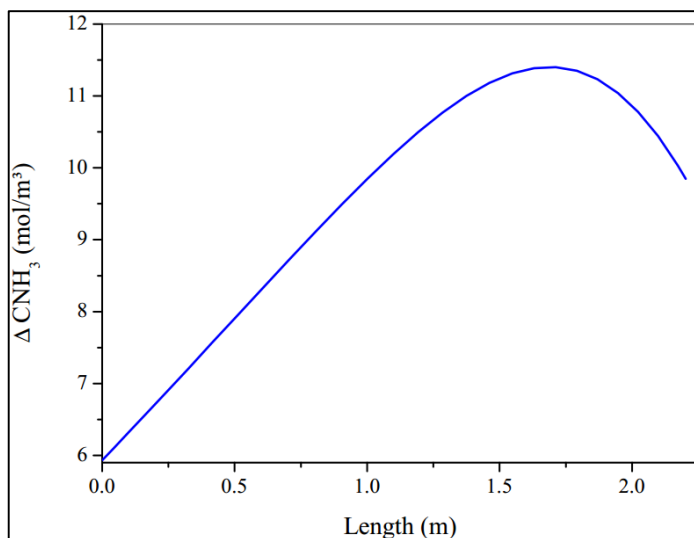
Figure 5.46. Concentration difference of NH$_3$ between catalyst surface and bulk along adiabatic converter.

In Figure 5.46, it is observed that ΔC_{NH_3} rises along the reactor, and it decreases at the end of the converter. The reduction in ΔC_{NH_3} at the end of the reactor occurs because external resistances decrease. The maximum value of ΔC_{NH_3} is 11,5 mol/m^3. However, the minimum value estimated of ammonia concentration is 133 mol/m^3 (beginning of the reactor), while ΔC_{NH_3} was 6 mol/m^3 at this point. Therefore, the maximum difference reaches 8% in the adiabatic converter. So, the pseudo-homogeneous approach is correct, because the highest resistances are inside particles (η) and not outside.

Moreover, the mass diffusivity in NH$_3$ is shown in Figure 5.47.
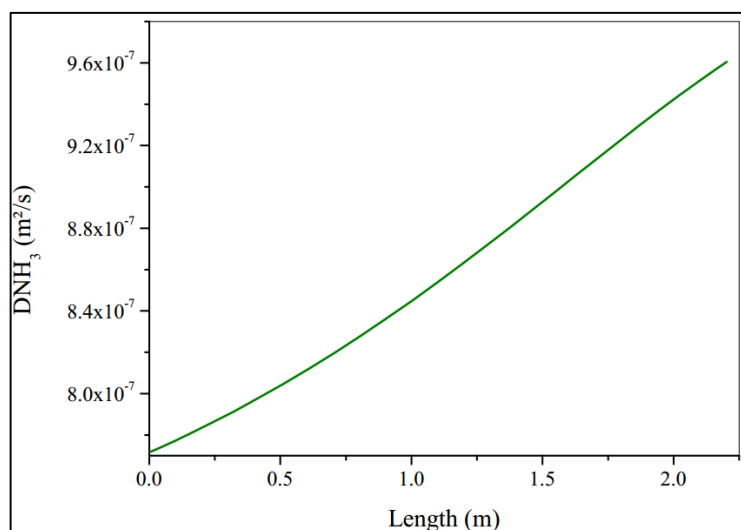
Figure 5.47. Mass diffusivity of NH3 (m²/s) along adiabatic converter.

It can be observed that diffusivity always increases along the adiabatic converter. After all, the diffusivity rises with temperature. However, the gas diffusivity values along the converter are low (about 10^{-7}), due to high pressure conditions.

The rise in diffusivity along the converter makes mass transfer coefficient k_c decrease in the reactor. Therefore, the mass resistance decreases, because more NH_3 is converted. Furthermore, k_c values are low even in turbulent flow, due to high pressure conditions.
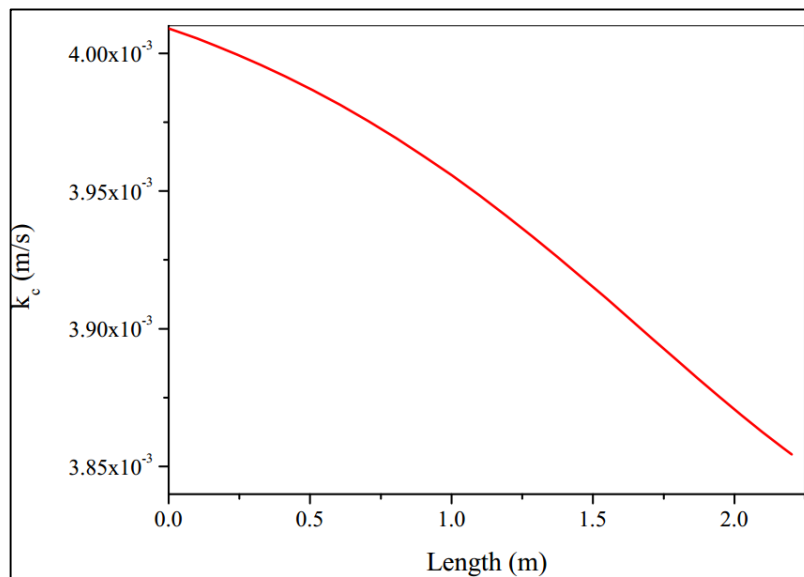
Figure 5.48. Mass transfer coefficient (m/s) along adiabatic converter.

Finally, boundary layer thickness δ is given in Figure 5.49.
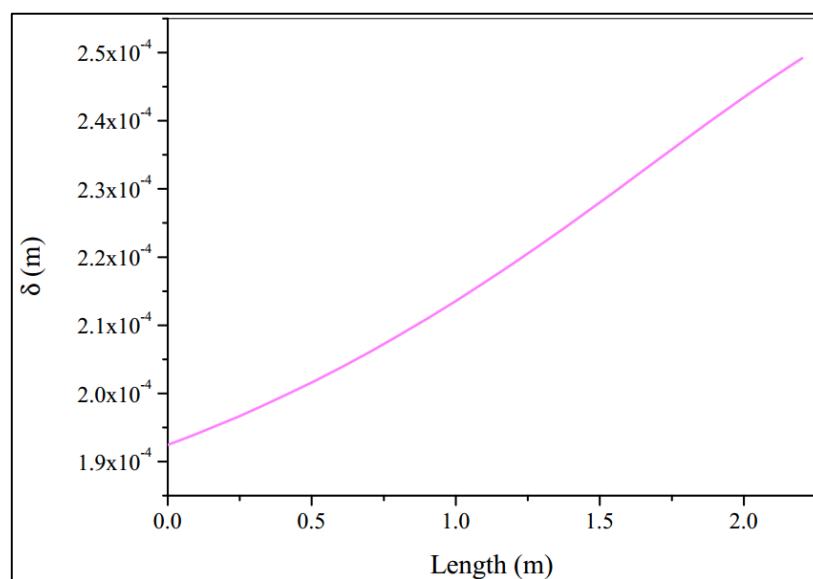
Figure 5.49. Boundary layer thickness along adiabatic converter.

In Figure 5.49, δ values increase along the adiabatic operation. After all, the diffusivity D_{NH_3} increases (numerator of Equation (4.91)) and k_c decreases (denominator of Equation (4.91)). However, even with its highest value, δ is very low for an industrial converter. It happens because residence time is small and the gas flow is turbulent.

5.5.2 Autothermal Reactor

The autothermal converter presents a maximum temperature point. Therefore, some changes related to mass transfer are expected at that point. Moreover, the dimensions of our autothermal reactor are the same as used in Section 5.4.2, as reported in Table 5.16. The same catalyst dimensions of Table 4.12 was used.

Table 5.16. Parameters for boundary layer calculations in the autothermal model.

Constraints for countercurrent simulation			
$T_{in} = 683.15\ K$			
$y_{N_2\,in}$	0.22	n_t	250
$y_{H_2\,in}$	0.66	$D_r(m)$	1.5
$y_{NH_3\,in}$	0.03	$L_r(m)$	2.5
$y_{CH_4\,in}$	0.045	$a'(m^2/m)$	11.78
$y_{Ar\,in}$	0.045	$U\ (W/m^2.K)$	650
$P_{in}(atm)$	225	$\dot{m}(kg/s)$	6

The NH_3 concentration difference is given in Figure 5.50. The highest value of ΔC_{NH_3} occurs at the maximum temperature point. After all, the mass diffusivity also increases at this point, making the reaction rate reach its peak. However, it is important to note that after the maximum temperature the values of ΔC_{NH_3} decrease, reaching $2\ mol/m^3$ from half way along the reactor to the end. Therefore, even in the autothermal case, the external resistances are lower compared to particle resistances.
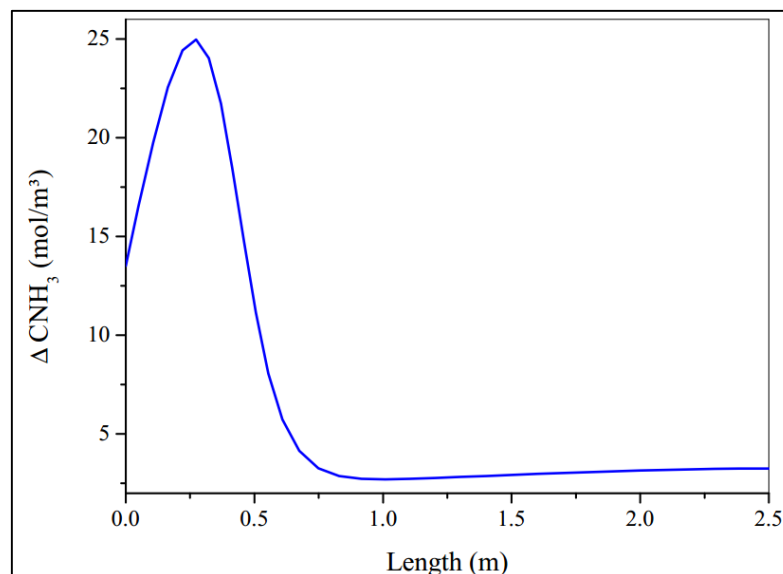
Figure 5.50. Concentration difference of NH3 between catalyst surface and bulk along autothermal converter.

The mass diffusivity profile also presented a peak in the maximum temperature bend, as shown in Figure 5.51. Furthermore, low values of D_{NH_3} were also computed due to high pressure in the reactor.
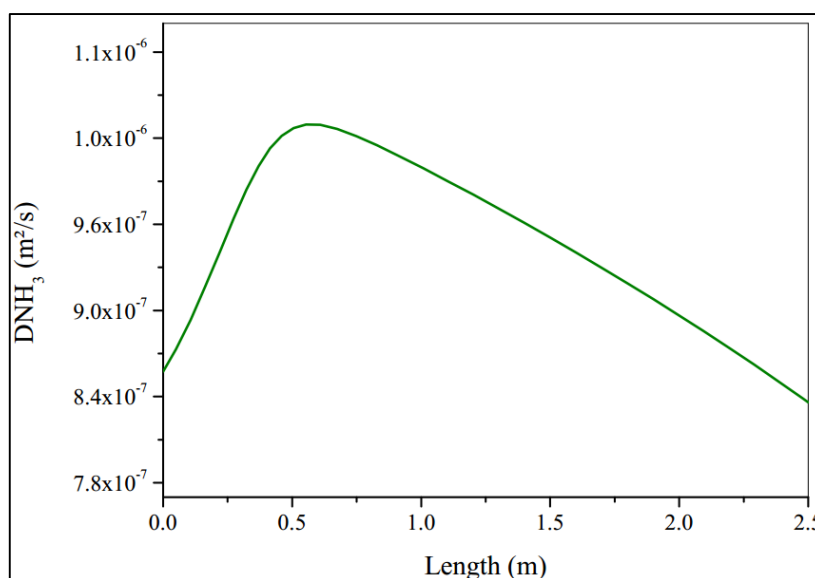
Figure 5.51. Mass diffusivity of NH3 (m²/s) along autothermal converter.

The mass transfer coefficient k_c is higher compared to the adiabatic reactor, as given in Figure 5.52. However, even in turbulent flows, the values remain low due to elevated pressures in the reactor. Moreover, compared to the adiabatic case, the autothermal option offers less resistance.
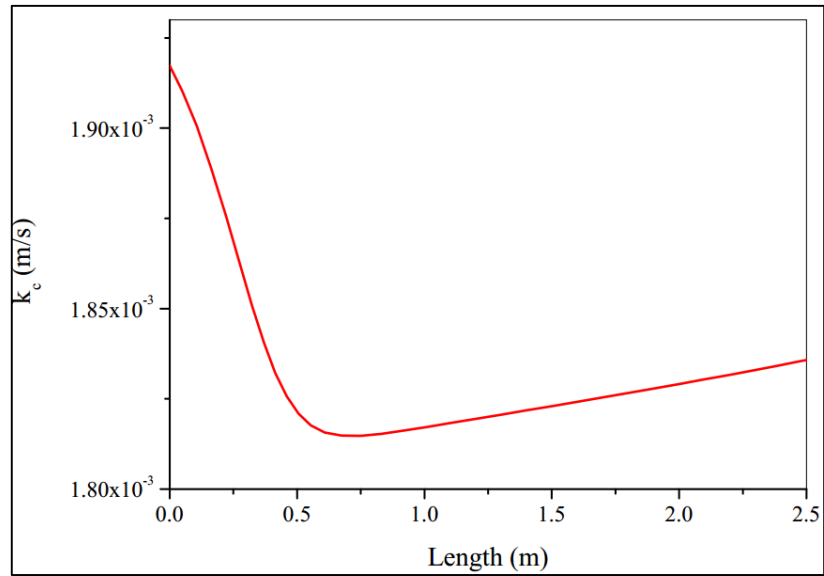
Figure 5.52. Mass transfer coefficient (m/s) along autothermal converter.

To summarize, the boundary layer thickness is given in Figure 5.53. The value of δ presents a peak at the maximum temperature point. Moreover, δ decreases because diffusivity also decreases at the end of the reactor.
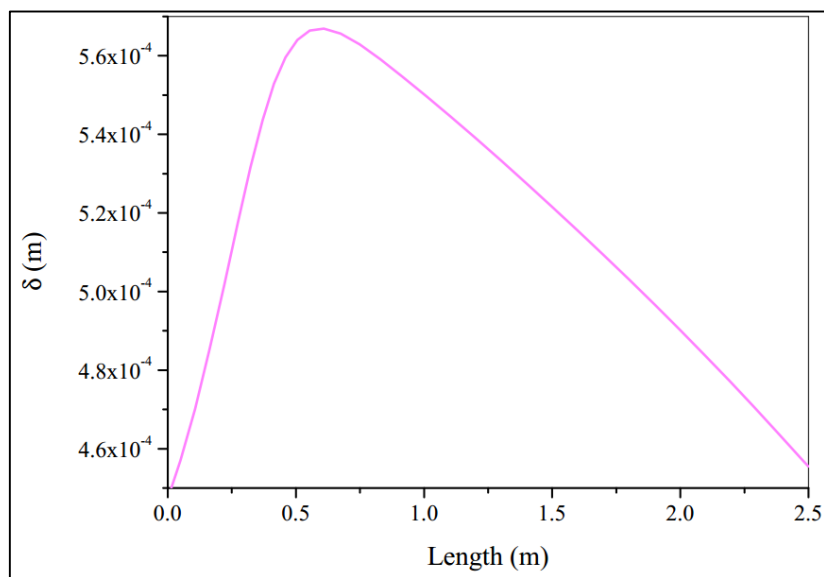
Figure 5.53. Boundary layer thickness along autothermal converter.

6   CONCLUSIONS/SUGGESTIONS

The operation of ammonia reactors is a great challenge. There is a large range of temperatures and pressures in its operation. Moreover, NH_3 is a polar gas and H_2 is a quantic gas, which brings more difficulty to modeling. Therefore, cubic *EoS* needs to be used in reactant gas modeling. Then, the expressions of *PR* and *SRK* are modeled.

In the first analysis, the historical modeling of ammonia synthesis reactors is made. Furthermore, the operation modes and main ammonia synthesis rate are modeled. It is observed that many expressions for reaction are used. The catalyst activity also changes from one equation to another. The α value varies according to the chemical activity model used, catalyst surface, support, and so on. Then, for *EoS* models, the catalyst activity for the reaction rate must be changed.

Both adiabatic and autothermal reactors are modeled. Initially, the pseudo-homogeneous approach is taken. Therefore, differences of temperature and concentration between catalyst particles and bulk are not accounted for. Moreover, only axial gradients are supposed in reactors. The Singh and Saraf rate expression with chemical activity computed by *EoS* is used. Also, Runge-Kutta methods with fixed and variable step size are computed.

The activity α is tuned to the *EoS* approach before validation. Moreover, the *RK4* and *RKF* methods are compared. Due to fewer iterations and the error control strategy, the *RKF* method is chosen to compute the remaining results. In the validation section, the adiabatic reactor presents a maximum relative error of 1.5 % in temperature and 11.7 % in conversion with the fitted model. On the other hand, the autothermal model presents a maximum error of 3 % in temperature. Therefore, both models prove reliable in simulating ammonia reactors.

After validation, a sensitivity analysis is made for adiabatic and autothermal models. The influence of inlet temperature, inlet pressure, inlet ammonia molar fraction and heat transfer coefficient are computed. In the adiabatic model, the operation at 300 atm, proves dangerous, as temperatures rise too much in the first converter. Moreover, equilibrium conversion decreases along this reactor. The autothermal reactor provides higher conversions, however it uses lower mass flows. This reactor shows less equilibrium limitation compared to the adiabatic, once heat is removed along it.

To summarize the results, an estimation of boundary layer properties is performed. The correlations computed differences in concentration in boundary layer supposing an

isothermal particle. In both models, the diffusion coefficient is very low, due to higher pressures. Moreover, the thickness of the boundary layer and difference of concentration are also low. Therefore, the significant resistances are inside the catalyst particles (computed by η), and not external to the pellets.

Furthermore, ammonia synthesis reactor modeling brings together different knowledge in chemical engineering. In mass balance, for example, chemical kinetics is used. The solution for a *PFR* requires differential equations with a numerical solution. The estimations of boundary layer require mass transfer, as also correction factor η. The pressure drop in fixed beds is computed using Ergun Equation. Finally, all of this information has to be programmed in code (in our case, Wolfram Mathematica is used). The simulation of reactors always requires great knowledge in many areas.

Suggestions can be made to achieve a better study of NH_3 synthesis reactors:

- Use of Computational Fluid Dynamics to predict flow variations inside the fixed beds or catalyst tubes. In our work, only the Ergun Equation was used.
- Computation of effectiveness factor η using a rigorous approach instead of a correlation. However, it will require the solution of a Boundary Value Problem at each step of the reactor, requiring more computational time.
- Simulation of axial and radial flow in the converter.

7 REFERENCES

ANANTHARAMAN, B.; HAZARIKA, S.; AHMAD, T; NAGVEKAR, M.; ARIYAPADI, S.; GUALY, R. Coal gasification technology for ammonia plants. In: PROCEEDINGS OF THE ASIA NITROGEN & SYNGAS 2012 CONFERENCE. Kuala Lumpur, Malaysia, 2012.

ANDA. Dinâmica do Mercado de Fertilizantes. Available at < http://www.anda.org.br/multimidia/investimentos.pdf>. Accessed at 03/10/2017.

ANNABLE, D. Application of the Temkin kinetic equation to ammonia synthesis in large-scale reactors. **Chemical Engineering Science**, v.1, p.145-154, 1952.

APPL, M. **Ammonia – Principles and Industrial Practice**. 1st edition. Weinheim: Wiley-VCH, 1999.

AZARHOOSH, M. J.; FARIVAR, F.; ALE EBRAHIM, H. Simulation and optimization of a horizontal ammonia synthesis reactor using genetic algorithm. **RSC Advances**, v.4, p.13419-13429. DOI: 10.1039/c3ra45410j, 2014.

BABU, B. V.; ANGIRA, R. Optimal design of an auto-thermal ammonia synthesis reactor. **Computers and Chemical Engineering**, v.29, p.1041-1045, 2005.

BADDOUR, R. F.; BRIAN, P., L. T.; LOGEAIS, B. A.; EYMERY, J. P. Steady-state simulation of an ammonia synthesis converter. **Chemical Engineering Science**, v.20, p.281-292, 1965.

BASF. Energy profile of the catalytic ammonia synthesis. Available at < https://www.basf.com/documents/corp/en/news-and-media/science-around-us/fertilizer-out-of-thin-air/Infografik_Ammoniaksynthese.pdf>. Accessed in 05/10/2017.

BRIAN, P., L. T.; BADDOUR, R. F.; EYMERY, J. P. Transient behaviour of an ammonia synthesis reactor. **Chemical Engineering Science**, v.20, p.297-310, 1965.

BURDEN, R. L.; FAIRES, J. D. **Numerical Analysis**. 9th edition. Canada: Cengage Learning, 2010.

BUZZI FERRARIS, G.; DONATI, G.; REJNA, F.; CARRÀ, S. An Investigation on Kinetic Models for Ammonia Synthesis. **Chemical Engineering Science**, v.29, p.1621-1627, 1974.

CARVALHO, M. **Análise de Desempenho de um Reator de Síntese de Amônia**. 2016. 99 p. Thesis (Master of Technology) – Instituto Alberto Luiz Coimbra de Pós-Graduação e Pesquisa em Engenharia (COPPE), Universidade Federal do Rio de Janeiro, Rio de Janeiro, 2016.

CHAPRA, S. C.; CANALE, R. P. **Métodos Numéricos para Engenharia**. 5ª edição. Mc Graw Hill Brasil, 2009.

DANESH, A. **PVT and Phase Behaviour Of Petroleum Reservoir Fluids**. 1st edition. Volume 47. Elsevier Science, 1988.

DASHTI, A.; KHORSAND, K.; MARVAST, M. A.; KAKAVAND, M. Modeling and Simulation of Ammonia Synthesis Reactor. **Petroleum &Coal**, v.48, n.2, p.15-23, June 2006. ISSN 1337-7027.

DWIVEDI, P. N.; UPADHYAY, S. N. Particle-Fluid Mass Transfer in Fixed and Fluidized Beds. **Industrial & Engineering Chemistry Process Design and Development**, v.16, n.2, p.157-165, 1977.

DYSON, D. C.; SIMON, J. C. A kinetic expression with diffusion correction for ammonia synthesis on industrial catalyst. **Industrial and Engineering Chemistry Fundamentals**, v.7, p.605-610, 1968.

EBRAHIMI, M.; MOUSAVI-DEHGANI, S. A.; DABIR, B.; SHAHRABADI, A. A comparison of PC-SAFT and PR-Peneloux equations of state in predicting the compressibility factors of lean gas-carbon dioxide mixtures at high pressures. **Journal of Natural Gas Science and Engineering**, v.31, p.681-691, 2016.

EDGAR, T. F.; HIMMELBLAU, D. M.; LASDON, L. S. **Optimization of chemical processes**. 2nd edition. Mc Graw Hill Chemical Engineering Series, 2001.

ELNASHAIE, S. S. Response to Comments on "Simulation and Optimization of an Industrial Ammonia Reactor". **Industrial and Engineering Chemistry Research**, v.28, p.1267, 1989.

ELNASHAIE, S. S.; ABASHAR, M. E.; AL-UBAID, A. S. Simulation and Optimization of an Industrial Ammonia Reactor. **Industrial and Engineering Chemistry Research**, v.27, p.2015-2022, 1988.

EMMETT, P. H.; KUMMER, J., T. Kinetics of Ammonia Synthesis. **Industrial and Engineering Chemistry**, v.35, n.6, p.677-683, 1943.

ERGUN, S. Fluid flow through packed columns. **Chemical Engineering Progress**, v.48, n.2, p.89-94, 1952.

ESTURILIO, G. G. **Modelagem e Controle Preditivo de um Reator de Amônia**. 2012. 90 p. Thesis (Master of Technology) – Departamento de Engenharia Química, Escola Politécnica da Universidade de São Paulo, Universidade de São Paulo, São Paulo, 2012.

FARIVAR, F.; ALE EBRAHIM, H. Modeling, Simulation, and Configuration Improvement of Horizontal Ammonia Synthesis Reactor. **Chemical Product and Process Modeling**, v.9, p.89-95, 2014, DOI: 10.1515/cppm-2013-0037.

FOGLER, H. S. **Elements of Chemical Reaction Engineering**. 4th edition. Prentice Hall, 2005.

GAINES, L. D. Optimal Temperatures for Ammonia Synthesis Converters. **Industrial & Engineering Chemistry Process Design and Development**, v.16, p.381-389, 1979.

GILLESPIE, L. J.; BEATTIE, J. A. The Thermodynamic Treatment of Chemical Equilibria in Systems Composed of Real Gases. A Relation of Heat of Reaction Applied to Ammonia Synthesis. The Energy and Entropy Constants for Ammonia. **Physical Review**, v.36, p.1008-1013, 1930.

GUACCI, U.; TRAINA, F.; BUZZI FERRARIS, G.; BARIZONE, R. On the Application of the Temkin Equation in the Evaluation of Catalysts for the Ammonia Synthesis. **Industrial & Engineering Chemistry Process Design and Development**, v.16, n.2, p.166-176, 1977.

HOLTER, E. **Feedforward for Stabilization of an Ammonia Synthesis Reactor**. 2010. 86 p. Thesis (Master of Science) – Department of Engineering Cybernetics, Norwegian Institute of Science and Technology, Norway, 2010.

KIROVA-YORDANOVA, Z. Exergy analysis of industrial ammonia synthesis. **Energy**, v.29, p.2373-2384. DOI: 10.1016/j.energy.2004.03.036, 2004.

KONTOGEORGIS, G. M.; FOLAS, G. K. **Thermodynamic Models for Industrial Applications: From Classical and Advanced Mixing Rules to Association Theories**. 1st edition. Wiley, 2010.

LARSON, A. T.; DODGE, R. L. The Ammonia Equilibrium. **Journal of American Chemical Society**, v.45, p.2918-2930, 1923.

LOPEZ-ECHEVERRY, J. S.; REIF-ACHERMAN, S.; ARAUJO-LOPEZ, E. Peng-Robinson equation of state: 40 years through cubics. **Fluid Phase Equilibria**, v.447, p.39-71, 2017.

MORUD, J.; SKOGESTAD, S. The Dynamics of Chemical Reaction with Heat Integration. In: AICHE ANNUAL MEETING. 1993.

MURASE, A.; ROBERTS, H. L.; CONVERSE, A. O. Optimal Thermal Design of an Autothermal Ammonia Synthesis Reactor. **Industrial & Engineering Chemistry Process Design and Development**, v.9, n.4, p.503-513, 1970.

MICHELSEN, M. L.; MOLLERUP, J. M. **Thermodynamic Models: Fundamentals and Computational Aspects**. 2nd edition. Tie-Line Publications, 1986.

NICHITA, D. V. A reduction method for phase equilibrium calculations with cubic equations of state. **Brazilian Journal of Chemical Engineering [online]**, v.23, n.3, p.427-434, 2006.

NIELSEN, A. **An investigation on promoted iron catalysts for the synthesis of ammonia**. 3rd edition. Jul. Gjellerups Forlag, 1968.

PATTENT OFFICE. Consumer and Corporate Affairs Canada (Ottawa, Canada). Alwyn Pinto. **Synthesis Process and Reactor**. CA: 1216734. Issued 870120. Class 23-426. 1988.

PEDERSEN, K. S.; CHRISTENSEN, P. L.; SHAIKH, J. A. **Phase Behavior of Petroleum Reservoir Fluids**. 2nd edition. CRC Press, 2014.

PÉNELOUX, A.; RAUZY, E; FRÉZE, R. A Consistent Correction for Redlich-Kwong-Soave Volumes. **Fluid Phase Equilibria,** v.8, p.7-23, 1982.

REDDY, K. V.; HUSAIN, A. Modeling and Simulation of Ammonia Synthesis Loop. **Industrial & Engineering Chemistry Process Design and Development**, v.21, p.359-367, 1982.

REIS, J. A. D. **Simulação de uma Unidade de Síntese de Amônia**. 1992. 104 p. Thesis (Master of Technology) – Faculdade de Engenharia de Campinas, Universidade Estadual de Campinas, Campinas, 1992.

ROBERTS, G. **Chemical Reactions and Chemical Reactors**. 1st edition. Wiley, 2008.

RODRIGUES, M. T. M. **Cinética da Síntese da Amônia**. 1984. 224 p. Thesis (Master of Technology) – Departamento de Engenharia Química, Faculdade de Engenharia de Campinas, Universidade Estadual de Campinas, Campinas, 1984.

SINGH, C. P. P. **Process Simulation of Ammonia Plant**. 1978. 168 p. Thesis (Doctor of Philosophy) – Department of Chemical Engineering, Indian Institute of Technology, Kanpur, 1978.

SINGH, C. P. P.; SARAF, D., N. Simulation of Ammonia Synthesis Reactors. **Industrial & Engineering Chemistry Process Design and Development**, v.18, p.364–370, 1979, DOI: 10.1021/i260071a002.

SINGH, V. B. **Modeling of Quench Type Ammonia Converters**. 1975. 11 p. Thesis (Master of Technology) – Department of Chemical Engineering, Indian Institute of Technology, Kanpur, 1975.

SIMON, J. M. **Computer Control of the Ammonia Process: A Simulation Study of an Ammonia Quench Converter in Both Steady and Transient Modes**. 1968. 169 p. Thesis (Doctor of Philosophy) – Rice University, Houston, 1968.

TEMKIN, M.; PYZHEV, V. Kinetics of the synthesis of ammonia on promoted iron catalysts. **Journal of Physical Chemistry. (USSR)**, v.13, p.851, 1939.

TEMKIN, M.; MOROZOV, N. M.; SHEPTINA, E. N. **Kinetika Kataliz**, v.4, p.565, 1963.

UPRETI, S. R.; DEB, K. Optimal Design of an Ammonia Synthesis Reactor using Genetic Algorithms. **Computers and Chemical Engineering**, v.21, p.87-92, 1997.

VAN HEERDEN, C. Autothermic Process-Process and Reactor Design. **Industrial and Engineering Chemistry**, v.45, n.6, p.1242-1247, 1953.

WHAT-WENT-HOW. Fundamentals of Hydrotreating – Part 3. Available at <http://what-when-how.com/petroleum-refining/the-hydrotreating-process-part-3/>. Accessed at 03/10/2017.

WU, X.; LI, C.; JIA, W. An improved viscosity model based on Peng–Robinson equation of state for light hydrocarbon liquids and gases. **Fluid Phase Equilibria**, v.380, p.147-151, 2014.

8 APPENDIX

In the appendix, additional information for thermodynamic properties and ODE solutions are given. The Numerical Methods Section explains the main numerical methods used in this dissertation. Thermodynamic Formulation describes step by step the equations used for the *EOS* cubic calculation.

8.1 Numerical Methods

Basically, the main numerical methods used for the ammonia reactor are root-finding and initial-value problems. The main ideas are given in the following sections.

8.1.1 Newton-Raphson Method

The procedure for the Z_{mix} calculation is a root-finding problem. The numerical method used must be robust. In addition, the procedure will be called upon hundreds of times (varying with T, P and $\{y_i\}_{vec}$). Therefore, rate of convergence also has to be high.

Newton-Raphson is a fixed-point iteration procedure, as described in Equation (8.1). Function $f(Z_i)$ is detailed in equation (4.8). The next value of Z is corrected by the derivative of a function. The analytic derivative in this method performs a quadratic convergence, which makes rapid convergence to "true root" (CHAPRA and CANALE, 2009). The mixture studied is in the gas phase, so an initial guess for Z is one (*i.e*, for $i = 0$).

$$Z_{i+1} = Z_i - \frac{f(Z_i)}{f'(Z_i)} \tag{8.1}$$

The analytic derivative $f'(Z_i)$ is described in Equation (8.2).

$$f'(Z_i) = 3.Z_i^{\;2} + 2.p.Z_i + q \tag{8.2}$$

Therefore, the general equation for Z_i calculation is given in Equation (8.3).

$$Z_{i+1} = Z_i - \left(\frac{Z_i^{\;3} + p.Z_i^{\;2} + q.Z_i + r}{3.Z_i^{\;2} + 2.p.Z_i + q} \right) \tag{8.3}$$

A concise flowsheet for Z_i calculation is shown in Figure 8.1.
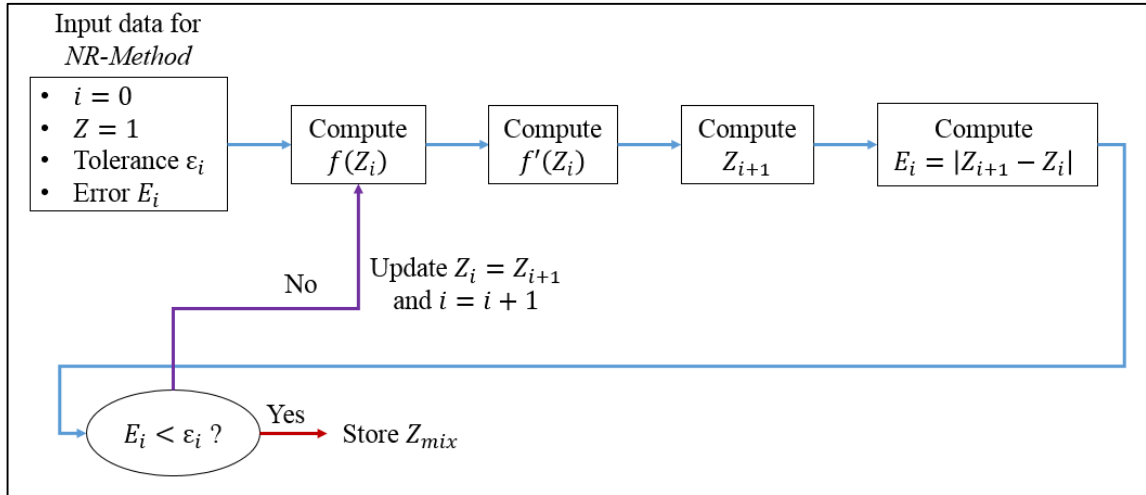
Figure 8.1. Flowchart for Z_{mix} calculation using the Newton-Raphson Method.

8.2 Thermodynamic Formulation

Especially in cubic *EoS*, the use of first and second derivatives is extensive. Properties like enthalpy and internal energy are necessary to compute C_p and C_v for mixtures, respectively.

8.2.1 Ideal Gas Heat Capacity C_p Formulation

The ideal gas heat capacity $C_p^{ig}{}_i$ $[J/mol]$ formulates the basis for real gas calculations. Our formulation determines $C_p^{ig}{}_i$ depending on eleven constants, as detected in equation (8.4) to (8.6). Temperature T is in K.

If $T \geq c_7$ and $T \leq c_8$, we have Equation (8.4).

$$C_p^{ig}{}_i(T) = c_1 + c_2.T + c_3.T^2 + c_4.T^3 + c_5.T^4 + c_6.T^5 \tag{8.4}$$

If $T < c_7$, relation (8.5) is valid.

$$C_p^{ig}{}_i(T) = c_9 + c_{10}.T^{c_{11}} \tag{8.5}$$

If $T > c_8$, Equation (8.6) describes $C_p^{ig}{}_i$.

$$C_p^{ig}{}_i(T) = c_8.T \tag{8.6}$$

Once $C_p^{ig}{}_i$ is computed, one can calculate the heat capacity $C_p^{ig}{}_{mix}$ for a mixture, as given in Equation (8.7).

$$C_p^{ig}{}_{mix}(T) = \sum_{i=1}^{N_{comp}} y_i . C_p^{ig}{}_i(T) \tag{8.7}$$

8.2.2 Ideal Gas Heat Capacity C_v Formulation

For an ideal gas, the difference between C_p^{ig} and C_v^{ig} is the constant R, as given in Equations (8.8) and (8.9).

$$C_p^{ig}{}_i(T) - C_v^{ig}{}_i(T) = R \tag{8.8}$$

$$C_v^{ig}{}_i(T) = C_p^{ig}{}_i(T) - R \tag{8.9}$$

The same analogy can be used for mixtures, as given in Equation (8.10).

$$C_v^{ig}{}_{mix}(T) = C_p^{ig}{}_{mix}(T) - R \tag{8.10}$$

Therefore, we must compute C_p^{ig} for each substance using Equations (8.4) to (8.6) in order to calculate C_v^{ig}. After that, one computed $C_p^{ig}{}_{mix}$ with Equation (8.7) and $C_v^{ig}{}_{mix}$ in (8.10).

8.2.3 Ideal Gas Enthalpy Formulation

The enthalpy for an ideal gas mixture is computed with the integral of equation (8.7). Therefore, we have the integral of a summation, described by relation (8.11).

$$H_{mix}^{ig}(T) = \sum_{i=1}^{N_{comp}} H_i^{ig}(T) = \int_{T_{ref}}^{T} C_p^{ig}{}_{mix}(T)dT = \int_{T_{ref}}^{T} \left[\sum_{i=1}^{N_{comp}} y_i . C_p^{ig}{}_i(T) \right] dT \tag{8.11}$$

So, the enthalpy of each component must be computed, with the same conditions of ideal gas heat capacity.

If $T \geq c_7$ and $T \leq c_8$, we have Equation (8.19).

$$H_i^{ig}(T) = \sum_{j=1}^{6}\left[\frac{c_j.\left(T^j - T_{ref}{}^j\right)}{j}\right] \tag{8.12}$$

If $T < c_7$, relation (8.13) is valid.

$$H_i^{ig}(T) = c_9.\left(T - T_{ref}\right) + \left(\frac{c_{10}}{c_{11}+1}\right).\left[T^{(c_{11}+1)} - T_{ref}{}^{(c_{11}+1)}\right] \tag{8.13}$$

If $T > c_8$, Equation (8.14) describes H_i^{ig}.

$$H_i^{ig}(T) = \left(\frac{c_8}{2}\right).\left[T^2 - T_{ref}{}^2\right] \tag{8.14}$$

8.2.4 Ideal Internal Energy Formulation

The same analogy used for the H_{mix}^{ig} calculation is used for the internal energy mixture U_{mix}^{ig}. First, the individual heat capacities $C_v^{ig}{}_i$ must be computed. Afterwards, the integral for $C_v^{ig}{}_{mix}$ will be calculated. A general approach is described in Equation (8.15).

$$U_{mix}^{ig}(T) = \sum_{i=1}^{N_{comp}} U_i^{ig}(T) = \int_{T_{ref}}^{T} C_v^{ig}{}_{mix}(T)dT = \int_{T_{ref}}^{T}\left[\sum_{i=1}^{N_{comp}} y_i.C_v^{ig}{}_i(T)\right]dT \tag{8.15}$$

Again, analogous polynomial expressions are obtained, as given in Equations (8.16) to (8.18). If $T \geq c_7$ and $T \leq c_8$, we have Equation (8.16).

$$U_i^{ig}(T) = R.\left(T_{ref} - T\right) + \sum_{j=1}^{6}\left[\frac{c_j.\left(T^j - T_{ref}{}^j\right)}{j}\right] \tag{8.16}$$

If $T < c_7$, relation (8.17) is valid.

$$U_i^{ig}(T) = R.\left(T_{ref} - T\right) + c_9.\left(T - T_{ref}\right) + \left(\frac{c_{10}}{c_{11}+1}\right).\left[T^{(c_{11}+1)} - T_{ref}{}^{(c_{11}+1)}\right] \tag{8.17}$$

If $T > c_8$, Equation (8.18) describes U_i^{ig}.

$$U_i^{ig}(T) = R.\left(T_{ref} - T\right) + \left(\frac{c_8}{2}\right).\left[T^2 - T_{ref}{}^2\right] \tag{8.18}$$

8.2.5   Residual Enthalpy Formulation

Residual properties are corrections when mixture deviates from the reference state (real and ideal conditions). The ideal formulation corrects temperature, while residual formulation corrects temperature and pressure. Residual enthalpy is shown in Equations (8.19) and (8.20).

$$H_{mix} - H_{mix}^{ig} = H_{mix}^{res} \qquad (8.19)$$

$$\frac{H_{mix}^{res}}{R.T} = (Z_{mix} - 1) - \int_{v}^{\infty} \left[T.\left(\frac{\partial Z_{mix}}{\partial T}\right)_{v} \right] \frac{dv}{v} \qquad (8.20)$$

Therefore, the derivative $\left(\frac{\partial Z_{mix}}{\partial T}\right)_{v}$ must be solved to compute the integral in relation (8.20). Isolating Z_{mix} in equation (4.7), we obtain Equation (8.21):

$$Z_{mix} = \left(\frac{v}{R}\right).\left(\frac{p}{T}\right) \qquad (8.21)$$

Using the quotient rule, derivative of Equation (8.21) is obtained in relation (8.22).

$$\left(\frac{\partial Z_{mix}}{\partial T}\right)_{v} = \left(\frac{v}{RT^2}\right)\left[T.\left(\frac{\partial P}{\partial T}\right)_{v} - P\right] \qquad (8.22)$$

Now the derivative $\left(\frac{\partial P}{\partial T}\right)_{v}$ must be solved. This derivative is calculated based on the formulation of cubic *EoS* given in Equation (4.2). The development is given in relations (8.23) and (8.24).

$$\left(\frac{\partial P}{\partial T}\right)_{v} = \frac{\partial}{\partial T}\left(\frac{R.T}{v - b}\right)_{v} - \frac{\partial}{\partial T}\left[\frac{a(T)}{(v + \delta_1.b).(v + \delta_2.b)}\right]_{v} \qquad (8.23)$$

$$\left(\frac{\partial P}{\partial T}\right)_{v} = \frac{R}{v - b} - \left[\frac{1}{(v + \delta_1.b).(v + \delta_2.b)}\right].\frac{da(T)}{dT} \qquad (8.24)$$

The derivative $\frac{da(T)}{dT}$ must be explored. Now one must replace $a(T)$ with a definition in relation (4.5).

$$a = \frac{(R.T)^2}{p}.A_{mix} \qquad (8.25)$$

Substituting Equation (8.25) in A_{mix} definition (Equation (4.17)), one obtains a general relation for $a(T)$.

$$a = \frac{(R.T)^2}{p}.A_{mix} \tag{8.26}$$

Now we can specify A_{mix} and A_{ij}, as given in Equations (8.27) and (8.28).

$$a = \frac{(R.T)^2}{p}.\sum_{i=1}^{N_{comp}}\sum_{j=1}^{N_{comp}} y_i.y_j.A_{ij} \tag{8.27}$$

$$a = \frac{(R.T)^2}{p}.\sum_{i=1}^{N_{comp}}\sum_{j=1}^{N_{comp}} y_i.y_j.\left(1-k_{ij}\right).\sqrt{A_{ii}A_{jj}} \tag{8.28}$$

The factors A_{ii} and A_{jj} are specified in Equation (4.14). We must replace this definition in Equation (8.28), as given in relation (8.29).

$$a = \frac{(R.T)^2}{p}.\sum_{i=1}^{N_{comp}}\sum_{j=1}^{N_{comp}} y_i.y_j.\left(1-k_{ij}\right).\sqrt{\left[\Omega_a.\left(\frac{P_r}{T_r^2}\right)_i.\alpha_i\right]\left[\Omega_a.\left(\frac{P_r}{T_r^2}\right)_j.\alpha_j\right]} \tag{8.29}$$

Replacing term $\frac{(R.T)^2}{p}$ in summation, Equation (8.30) is obtained.

$$a = \sum_{i=1}^{N_{comp}}\sum_{j=1}^{N_{comp}} y_i.y_j.\left(1-k_{ij}\right).\sqrt{\left[\left(\frac{\Omega_a.R^2.T_c^2}{P_c}\right)_i.\alpha_i\right]\left[\left(\frac{\Omega_a.R^2.T_c^2}{P_c}\right)_j.\alpha_j\right]} \tag{8.30}$$

Organizing terms in the equation above, we have equality (8.31).

$$a = \sum_{i=1}^{N_{comp}}\sum_{j=1}^{N_{comp}} y_i.y_j.\left(1-k_{ij}\right).\sqrt{\left(\frac{\Omega_a.R^2.T_c^2}{P_c}\right)_i.\left(\frac{\Omega_a.R^2.T_c^2}{P_c}\right)_j}\sqrt{\alpha_i.\alpha_j} \tag{8.31}$$

The only term which depends on temperature is $\sqrt{\alpha_i.\alpha_j}$. All other terms are constant with temperature variation. Therefore, the calculation of derivative $\frac{da(T)}{dT}$ depends on derivative of expression $\frac{d\sqrt{\alpha_i.\alpha_j}}{dT}$. This derivative is specified in relations (8.32) to (8.34).

Using product rule, we have Equation (8.32).

$$\frac{d\sqrt{\alpha_i.\alpha_j}}{dT} = \left(\sqrt{\alpha_i}.\frac{d\sqrt{\alpha_j}}{dT} + \sqrt{\alpha_j}.\frac{d\sqrt{\alpha_i}}{dT}\right) \tag{8.32}$$

With α_i definition in Equation (4.13), we can solve derivative $\frac{d\sqrt{\alpha_i}}{dT}$ using the chain rule, as defined in Equation (8.33).

$$\frac{d\sqrt{\alpha_i}}{dT} = -\left(\frac{1}{2}\right).f(\omega_i).\left(\frac{1}{\sqrt{T_{c_i}}}\right).\left(\frac{1}{\sqrt{T}}\right) \tag{8.33}$$

We have arrived at the last temperature dependent term. Now we can return to Equation (8.32) and replace the derivative in relation (8.33).

$$\frac{d\sqrt{\alpha_i.\alpha_j}}{dT} = \left(-\frac{1}{2}\right).\left[\sqrt{\alpha_i}.f(\omega_j).\frac{1}{\sqrt{T_{c_j}}}.\frac{1}{\sqrt{T}} + \sqrt{\alpha_j}.f(\omega_i).\frac{1}{\sqrt{T_{c_i}}}.\frac{1}{\sqrt{T}}\right] \tag{8.34}$$

Finally, we have an expression for $\frac{da(T)}{dT}$, given in quality (8.35).

$$\frac{da}{dT} = \left(-\frac{1}{2}\right).\sum_{i=1}^{N_{comp}}\sum_{j=1}^{N_{comp}} y_i.y_j.(1-k_{ij}).\sqrt{\gamma_i.\gamma_j}.\left[\sqrt{\alpha_i}.f(\omega_j).\frac{1}{\sqrt{T_{c_j}}}.\frac{1}{\sqrt{T}} + \sqrt{\alpha_j}.f(\omega_i).\frac{1}{\sqrt{T_{c_i}}}.\frac{1}{\sqrt{T}}\right] \tag{8.35}$$

The terms γ_i and γ_j are represented in Equation (8.36).

$$\gamma_i = \left(\frac{\Omega_a.R^2.T_c^2}{P_c}\right)_i \tag{8.36}$$

Therefore, we have derivative $\left(\frac{\partial P}{\partial T}\right)_v$ in Equation (8.24) solved. So, the derivative $\left(\frac{\partial Z_{mix}}{\partial T}\right)_v$ in Equation (8.22) is also solved.

$$\left(\frac{\partial Z_{mix}}{\partial T}\right)_v = \left(\frac{v}{RT^2}\right).\left[\frac{1}{(v+\delta_1.b).(v+\delta_2.b)}\right].\left[a-T.\left(\frac{da}{dT}\right)\right] \tag{8.37}$$

Replacing $\left(\frac{\partial Z_{mix}}{\partial T}\right)_v$ in Equation (8.20), we find relations (8.38) and (8.39).

$$\frac{H_{mix}^{res}}{R.T} = (Z_{mix} - 1)$$

$$- \int_v^\infty \left\{ T.\left(\frac{v}{RT^2}\right).\left[\frac{1}{(v + \delta_1.b).(v + \delta_2.b)}\right].\left[a - T.\left(\frac{da}{dT}\right)\right]\right\} \frac{dv}{v} \qquad (8.38)$$

$$\frac{H_{mix}^{res}}{R.T} = (Z_{mix} - 1) - \left(\frac{1}{R.T}\right).\left[a - T.\left(\frac{da}{dT}\right)\right]. \int_v^\infty \frac{dv}{(v + \delta_1.b).(v + \delta_2.b)} \qquad (8.39)$$

The only term missing for H_{mix}^{res} determination is the integral of Equation (8.39), which is solved from equation (8.40) to (8.42).

$$\int_v^\infty \frac{dv}{(v + \delta_1.b).(v + \delta_2.b)} = -\left[\frac{1}{b.(\delta_1 - \delta_2)}\right].ln\left(\frac{v + \delta_2.b}{v + \delta_1.b}\right) \qquad (8.40)$$

Now the numerator and denominator in expression ln will be organized, because generally Z_{mix} is computed, not v. A definition of coefficient b is detailed in Equation (8.41).

$$b = B_{mix}.\left(\frac{R.T}{p}\right) \qquad (8.41)$$

Replacing equation (8.41) for Equation (8.40), we find Equation (8.42).

$$\int_v^\infty \frac{dv}{(v + \delta_1.b).(v + \delta_2.b)} = -\left[\frac{1}{b.(\delta_1 - \delta_2)}\right].ln\left(\frac{Z_{mix} + \delta_2.B_{mix}}{Z_{mix} + \delta_1.B_{mix}}\right) \qquad (8.42)$$

Now equation (8.42) can be replaced in equality (8.39), giving relations (8.43) and (8.44).

$$\frac{H_{mix}^{res}}{R.T} = (Z_{mix} - 1) - \left(\frac{1}{R.T}\right).\left[a - T.\left(\frac{da}{dT}\right)\right].\left[\frac{-1}{b.(\delta_1 - \delta_2)}\right].ln\left(\frac{Z_{mix} + \delta_2.B_{mix}}{Z_{mix} + \delta_1.B_{mix}}\right) \qquad (8.43)$$

$$H_{mix}^{res} = R.T.(Z_{mix} - 1) + \left[a - T.\left(\frac{da}{dT}\right)\right].\left[\frac{1}{b.(\delta_1 - \delta_2)}\right].ln\left(\frac{Z_{mix} + \delta_2.B_{mix}}{Z_{mix} + \delta_1.B_{mix}}\right) \qquad (8.44)$$

Lastly, we can reverse ln, giving the final relation for residual enthalpy in cubic EoS H_{mix}^{res} in Equation (8.45).

$$H_{mix}^{res} = R.T.(Z_{mix} - 1) + \left[\frac{T.\left(\frac{da}{dT}\right) - a}{b.(\delta_1 - \delta_2)}\right].ln\left(\frac{Z_{mix} + \delta_1.B_{mix}}{Z_{mix} + \delta_2.B_{mix}}\right) \qquad (8.45)$$

8.2.6 Residual Internal Energy Formulation

The internal energy also contains a correction for high-pressure situations. As is the same for enthalpy, in ideal gas situations, the residual contributions tend to zero. The residual term is described by Equations (8.46) and (8.47).

$$U_{mix} - U_{mix}^{ig} = U_{mix}^{res} \tag{8.46}$$

$$U_{mix}^{res} = \int_{\infty}^{v} \left[T \cdot \left(\frac{\partial P}{\partial T} \right)_v - P \right] dv \tag{8.47}$$

Fortunately, the derivative $\left(\frac{\partial P}{\partial T} \right)_v$ was determined in a previous section (in Equation (8.24)). The term P is computed according to the *EoS* format, given in relation (4.2). Then, Equation (8.47) becomes (8.48) and (8.49):

$$\left[T \cdot \left(\frac{\partial P}{\partial T} \right)_v - P \right] = \left[\frac{1}{(v + \delta_1 \cdot b) \cdot (v + \delta_2 \cdot b)} \right] \cdot \left[a - T \cdot \left(\frac{da}{dT} \right) \right] \tag{8.48}$$

$$\int_{\infty}^{v} \left[T \cdot \left(\frac{\partial P}{\partial T} \right)_v - P \right] dv = \int_{\infty}^{v} \left[\frac{a - T \cdot \left(\frac{da}{dT} \right)}{(v + \delta_1 \cdot b) \cdot (v + \delta_2 \cdot b)} \right] dv \tag{8.49}$$

Observing the relation above, the numerator of an integral is constant with v. Therefore, our integral becomes Equation (8.50).

$$\int_{\infty}^{v} \left[T \cdot \left(\frac{\partial P}{\partial T} \right)_v - P \right] dv = \left[a - T \cdot \left(\frac{da}{dT} \right) \right] \int_{\infty}^{v} \left[\frac{1}{(v + \delta_1 \cdot b) \cdot (v + \delta_2 \cdot b)} \right] dv \tag{8.50}$$

One can change the limit of the integral, obtaining Equation (8.51).

$$\int_{\infty}^{v} \left[T \cdot \left(\frac{\partial P}{\partial T} \right)_v - P \right] dv = \left[T \cdot \left(\frac{da}{dT} \right) - a \right] \int_{v}^{\infty} \left[\frac{1}{(v + \delta_1 \cdot b) \cdot (v + \delta_2 \cdot b)} \right] dv \tag{8.51}$$

The integral above is solved in Equation (8.42). So, an expression for residual internal energy is computed in relation (8.52).

$$U_{mix}^{res} = \left[\frac{T \cdot \left(\frac{da}{dT} \right) - a}{b \cdot (\delta_1 - \delta_2)} \right] \cdot ln \left(\frac{Z_{mix} + \delta_1 \cdot B_{mix}}{Z_{mix} + \delta_2 \cdot B_{mix}} \right) \tag{8.52}$$

Furthermore, an additional relation is discovered. The difference between H_{mix}^{res} and U_{mix}^{res} depends on compressibility factor Z_{mix} (in Equation (8.53)).

$$H_{mix}^{res} - U_{mix}^{res} = R.T.(Z_{mix} - 1) \tag{8.53}$$

8.2.7 Residual Heat Capacity Cₚ Formulation

The same as for enthalpy, the real heat capacity for a gas has two parts: ideal and residual. It is described by Equation (8.54).

$$C_{p\,mix} = C_p^{ig}{}_{mix} + C_p^{res}{}_{mix} \tag{8.54}$$

$C_p^{ig}{}_{mix}$ is the ideal gas heat capacity for mixture $[J/mol]$ computed by equation (8.7). $C_p^{res}{}_{mix}$ is the residual heat capacity for mixture $[J/mol]$ and $C_{p\,mix}$ is total heat capacity for mixture $[J/mol]$.

Therefore, we must compute residual heat capacity. The definition depends on residual enthalpy, as detailed in Equation (8.55).

$$C_p^{res}{}_{mix} = \left(\frac{\partial H_{mix}^{res}}{\partial T}\right)_P \tag{8.55}$$

H_{mix}^{res} is given by relation (8.45). We must derivate it. Auxiliary expressions given in Equations (8.56) to (8.59) give the main derivatives.

$$Term\,1 = [R.T.(Z_{mix} - 1)] \tag{8.56}$$

$$Term\,2 = \left[\frac{T.\left(\frac{da}{dT}\right) - a}{b.(\delta_1 - \delta_2)}\right] \tag{8.57}$$

$$Term\,3 = ln\left(\frac{Z_{mix} + \delta_1.B_{mix}}{Z_{mix} + \delta_2.B_{mix}}\right) \tag{8.58}$$

$$\left(\frac{\partial H_{mix}^{res}}{\partial T}\right)_P = \left(\frac{\partial Term\,1}{\partial T}\right)_P + \left(\frac{\partial Term\,2}{\partial T}\right)_P.Term\,3 + \left(\frac{\partial Term\,3}{\partial T}\right)_P.Term\,2 \tag{8.59}$$

The derivative for $Term\,1$ involves $\left(\frac{\partial Z_{mix}}{\partial T}\right)_P$, as given in expressions (8.60) to (8.62), with the Chain Rule.

$$\left(\frac{\partial Term\, 1}{\partial T}\right)_P = \left(\frac{\partial}{\partial T}\right)_P [R.T.(Z_{mix} - 1)] \tag{8.60}$$

$$\left(\frac{\partial Term\, 1}{\partial T}\right)_P = \left(\frac{\partial}{\partial T}\right)_P [R.T.Z_{mix} - R.T)] \tag{8.61}$$

$$\left(\frac{\partial Term\, 1}{\partial T}\right)_P = R.\left[T.\left(\frac{\partial Z_{mix}}{\partial T}\right)_P + Z_{mix} - 1\right] \tag{8.62}$$

Now we must compute $\left(\frac{\partial Z_{mix}}{\partial T}\right)_P$. It can be done using triple product, as described in relations (8.63) and (8.64).

$$\left(\frac{\partial Z_{mix}}{\partial T}\right)_P \cdot \left(\frac{\partial f}{\partial Z_{mix}}\right)_T \cdot \left(\frac{\partial T}{\partial f}\right)_{Z_{mix}} = -1 \tag{8.63}$$

$$\left(\frac{\partial Z_{mix}}{\partial T}\right)_P = \frac{\left[\frac{\partial(-f)}{\partial T}\right]_{Z_{mix}}}{\left(\frac{\partial f}{\partial Z_{mix}}\right)_T} \tag{8.64}$$

However, which function is f? It is the implicit form of cubic *EoS*, given by Equation (4.8) ,Table 4.2 and Table 4.3. Therefore, we must specify each of the derivatives above, described in Equations (8.65) to (8.67).

$$Term\, 4 = -Z_{mix}^{2}.s + 2.B_{mix}.Z_{mix}(t - u) + Z_{mix}.t + u.B_{mix}\left(3.B_{mix}^{2} + 2\right) + A_{mix} \tag{8.65}$$

$$\left[\frac{\partial(-f)}{\partial T}\right]_{Z_{mix}} = \left(\frac{dA_{mix}}{dT}\right).(B_{mix} - Z_{mix}) + \left(\frac{dB_{mix}}{dT}\right).Term\, 4 \tag{8.66}$$

$$\left(\frac{\partial f}{\partial Z_{mix}}\right)_T = 3.Z_{mix}^{2} + 2.Z_{mix}.(s.B_{mix} - 1) + \left[A_{mix} + u.B_{mix}^{2} - t.B_{mix}(B_{mix} + 1)\right] \tag{8.67}$$

Again, we must determine new derivatives. They are $\left(\frac{dA_{mix}}{dT}\right)$ and $\left(\frac{dB_{mix}}{dT}\right)$, described in Equations (8.68) and (8.69).

$$\left(\frac{dA_{mix}}{dT}\right) = \frac{p}{(R.T)^2} \cdot \left[\left(\frac{da}{dT}\right) - \left(\frac{2.a}{T}\right)\right] \tag{8.68}$$

$$\left(\frac{dB_{mix}}{dT}\right) = -\left(\frac{p}{R.T^2}\right).b \tag{8.69}$$

The derivative $\left(\frac{da}{dT}\right)$ is calculated in residual enthalpy. It is computed by equation (8.35). Lastly, the determination of $\left(\frac{\partial Z_{mix}}{\partial T}\right)_P$ and therefore, $\left(\frac{\partial Term\,1}{\partial T}\right)_P$ was possible. *Term 4*, $\left(\frac{dA_{mix}}{dT}\right)$ and $\left(\frac{dB_{mix}}{dT}\right)$ in Equation (8.70) were given in (8.65), (8.68) and (8.69) respectively.

$$\left(\frac{\partial Z_{mix}}{\partial T}\right)_P = \frac{\left(\frac{dA_{mix}}{dT}\right).(B_{mix} - Z_{mix}) + \left(\frac{dB_{mix}}{dT}\right).Term\,4}{3.Z_{mix}^2 + 2.Z_{mix}.(s.B_{mix} - 1) + \left[A_{mix} + u.B_{mix}^2 - t.B_{mix}(B_{mix} + 1)\right]} \tag{8.70}$$

Now we must go back to equation (8.59) to investigate $\left(\frac{\partial Term\,2}{\partial T}\right)_P$. This derivative is described by Equations (8.71) and (8.72).

$$\left(\frac{\partial Term\,2}{\partial T}\right)_P = \left[\frac{1}{b.(\delta_1 - \delta_2)}\right].\frac{\partial}{\partial T}\left[T.\left(\frac{da}{dT}\right) - a\right]_P \tag{8.71}$$

$$\left(\frac{\partial Term\,2}{\partial T}\right)_P = \left[\frac{1}{b.(\delta_1 - \delta_2)}\right].\left(T.\frac{d^2a}{dT^2}\right) \tag{8.72}$$

In Equation (8.72), the derivative $\left(\frac{d^2a}{dT^2}\right)$ had not been calculated yet. We obtain it deriving again $\left(\frac{da}{dT}\right)$, which is described by Equation (8.35). Rearranging Equation (8.35), we have Equations (8.73) and (8.74).

$$a_{c_{ij}} = \left(-\frac{1}{2}\right).y_i.y_j.(1 - k_{ij}).\sqrt{\left(\frac{\Omega_a.R^2.T_c^2}{P_c}\right)_i.\left(\frac{\Omega_a.R^2.T_c^2}{P_c}\right)_j} \tag{8.73}$$

$$\frac{da}{dT} = \sum_{i=1}^{N_{comp}} \sum_{j=1}^{N_{comp}} a_{c_{ij}}.\left[\sqrt{\alpha_i}.f(\omega_j).\frac{1}{\sqrt{T_{c_j}}}.\frac{1}{\sqrt{T}} + \sqrt{\alpha_j}.f(\omega_i).\frac{1}{\sqrt{T_{c_i}}}.\frac{1}{\sqrt{T}}\right] \tag{8.74}$$

The term $a_{c_{ij}}$ does not vary with temperature. Consequently, the derivation must be done with term in brackets, which is called $Term\,5$. Deriving this term, we obtain Equations (8.75) to (8.77).

$$\frac{d}{dT}Term\ 5 = \frac{d}{dT}\left[\sqrt{\alpha_i}.f(\omega_j).\frac{1}{\sqrt{T_{c_j}}}.\frac{1}{\sqrt{T}} + \sqrt{\alpha_j}.f(\omega_i).\frac{1}{\sqrt{T_{c_i}}}.\frac{1}{\sqrt{T}}\right] \tag{8.75}$$

$$\frac{d}{dT}Term\ 5 = \frac{f(\omega_j)}{\sqrt{T_{c_j}}}\left[\frac{d}{dT}\sqrt{\alpha_i}.\frac{1}{\sqrt{T}} + \frac{d}{dT}\left(\frac{1}{\sqrt{T}}\right).\sqrt{\alpha_i}\right] + \frac{f(\omega_i)}{\sqrt{T_{c_i}}}\left[\frac{d}{dT}\sqrt{\alpha_j}.\frac{1}{\sqrt{T}} + \frac{d}{dT}\left(\frac{1}{\sqrt{T}}\right).\sqrt{\alpha_j}\right] \tag{8.76}$$

The derivative $\frac{d\sqrt{\alpha_i}}{dT}$ is solved in Equation (8.33). In addition, the derivative $\frac{d}{dT}\left(\frac{1}{\sqrt{T}}\right)$ is computed below. Therefore, the unknown derivatives in Equation (8.76) are now answered.

$$\frac{d}{dT}\left(\frac{1}{\sqrt{T}}\right) = -\left(\frac{1}{2}\right).\frac{f(\omega_i)}{\sqrt{T_{c_i}}.\sqrt{T}} \tag{8.77}$$

Finally, we have computed derivative $\left(\frac{d^2 a}{dT^2}\right)$, which is defined in Equations (8.78) to (8.80).

$$Term\ 6 = \left(\frac{f(\omega_i)}{\sqrt{T_{c_i}}}\right).\left[\left(-\frac{1}{2}\right).\left(\frac{f(\omega_j)}{\sqrt{T_{c_j}}.\sqrt{T}}\right).\left(\frac{1}{\sqrt{T}}\right) + \left(-\frac{1}{2}\right).\left(\frac{\sqrt{\alpha_j}}{T^{3/2}}\right)\right] \tag{8.78}$$

$$Term\ 7 = \left(\frac{f(\omega_j)}{\sqrt{T_{c_j}}}\right).\left[\left(-\frac{1}{2}\right).\left(\frac{f(\omega_i)}{\sqrt{T_{c_i}}.\sqrt{T}}\right).\left(\frac{1}{\sqrt{T}}\right) + \left(-\frac{1}{2}\right).\left(\frac{\sqrt{\alpha_i}}{T^{3/2}}\right)\right] \tag{8.79}$$

$$\frac{d^2 a}{dT^2} = \sum_{i=1}^{N_{comp}} \sum_{j=1}^{N_{comp}} a_{c_{ij}}.(Term\ 6 + Term\ 7) \tag{8.80}$$

The derivative $\left(\frac{\partial Term\ 2}{\partial T}\right)_P$ in equation (8.72) is completely described. Our last step is to solve the derivative $\left(\frac{\partial Term\ 3}{\partial T}\right)_P$ to compute $C_p^{res}{}_{mix}$ analytically. Therefore, we derive $\left(\frac{\partial Term\ 3}{\partial T}\right)_P$, obtaining Equation (8.81).

$$\left(\frac{\partial Term\ 3}{\partial T}\right)_P = \left(\frac{\partial}{\partial T}\right)_P\left[ln\left(\frac{Z_{mix} + \delta_1.B_{mix}}{Z_{mix} + \delta_2.B_{mix}}\right)\right] \tag{8.81}$$

One can apply the Chain Rule in Equation (8.81). Then, we solve the derivative and final Equation (8.83).

$$Term\ 8 = \left[\frac{(\delta_1 - \delta_2)}{(Z_{mix} + \delta_1.B_{mix}).(Z_{mix} + \delta_2.B_{mix})}\right] \tag{8.82}$$

$$\left(\frac{\partial Term\ 3}{\partial T}\right)_P = Term\ 8.\left[Z_{mix}.\left(\frac{dB_{mix}}{dT}\right) + B_{mix}.\left(\frac{\partial Z_{mix}}{\partial T}\right)_P\right] \tag{8.83}$$

Finally, we have $C_p^{res}{}_{mix}$ $[J/mol]$ analytically in Equation (8.84).

$$C_p^{res}{}_{mix} = R.\left[T.\left(\frac{\partial Z_{mix}}{\partial T}\right)_P + Z_{mix} - 1\right] + \left[ln\left(\frac{Z_{mix} + \delta_1.B_{mix}}{Z_{mix} + \delta_2.B_{mix}}\right)\right].\left[\frac{1}{b.(\delta_1 - \delta_2)}\right].\left(T.\frac{d^2a}{dT^2}\right)$$
$$+ \left[\frac{(\delta_1 - \delta_2)}{(Z_{mix} + \delta_1.B_{mix}).(Z_{mix} + \delta_2.B_{mix})}\right].\left[Z_{mix}.\left(\frac{dB_{mix}}{dT}\right) + B_{mix}.\left(\frac{\partial Z_{mix}}{\partial T}\right)_P\right] \tag{8.84}$$

Another way to calculate $C_p^{res}{}_{mix}$ in Equation (8.55) uses numerical derivatives. After all, enthalpy depends more on temperature than pressure. Therefore, we do not need to calculate any of the derivatives above, only the enthalpy values. The derivative $\left(\frac{\partial H_{mix}^{res}}{\partial T}\right)_P$ is approached by a first order derivative $\frac{dH_{mix}^{res}}{dT}$, as given in Equations (8.85) to (8.87).

Two-point derivative:

$$C_p^{res}{}_{mix} = \frac{H_{mix}^{res}(T + \Delta T) - H_{mix}^{res}(T)}{\Delta T} - O(h) \tag{8.85}$$

Three-point derivative (mid-point rule):

$$C_p^{res}{}_{mix} = \frac{H_{mix}^{res}(T + \Delta T) - H_{mix}^{res}(T - \Delta T)}{2.\Delta T} - O(h^2) \tag{8.86}$$

Five-point derivative (mid-point rule):

$$C_p^{res}{}_{mix} = \frac{H_{mix}^{res}(T - 2.\Delta T) - 8.H_{mix}^{res}(T - \Delta T) + 8H_{mix}^{res}(T + \Delta T) - H_{mix}^{res}(T + 2.\Delta T)}{12.\Delta T}$$
$$+ O(h^4) \tag{8.87}$$

In the relations above, ΔT is the temperature step $[K]$ and O is the local truncation error. Obviously, the more points we use in derivatives overhead, the higher the order of error. For example, a two-point formula has a first order error while a five-point formula has a fourth order error.

8.2.8 Residual Heat Capacity C_v Formulation

The residual contribution for heat capacity at a constant volume is computed according to Equation (8.88).

$$C_v^{res}{}_{mix} = \left(\frac{\partial U_{mix}^{res}}{\partial T}\right)_v \tag{8.88}$$

The derivative is described in Equations (8.89) and (8.90).

$$\left(\frac{\partial U_{mix}^{res}}{\partial T}\right)_v = \left(\frac{\partial}{\partial T}\right)_v \left\{ \left[\frac{T.\left(\frac{da}{dT}\right) - a}{b.(\delta_1 - \delta_2)}\right] . \ln\left(\frac{Z_{mix} + \delta_1.B_{mix}}{Z_{mix} + \delta_2.B_{mix}}\right) \right\} \tag{8.89}$$

$$\left(\frac{\partial U_{mix}^{res}}{\partial T}\right)_v = \ln\left(\frac{Z_{mix} + \delta_1.B_{mix}}{Z_{mix} + \delta_2.B_{mix}}\right)\left(\frac{\partial}{\partial T}\right)_v \left[\frac{T.\left(\frac{da}{dT}\right) - a}{b.(\delta_1 - \delta_2)}\right] \tag{8.90}$$

Then, we reach the final expression for $C_v^{res}{}_{mix}$ in (8.91).

$$C_v^{res}{}_{mix} = \ln\left(\frac{Z_{mix} + \delta_1.B_{mix}}{Z_{mix} + \delta_2.B_{mix}}\right) . \left[\frac{T.\left(\frac{d^2a}{dT^2}\right)}{b.(\delta_1 - \delta_2)}\right] \tag{8.91}$$

The second derivative $\left(\frac{d^2a}{dT^2}\right)$ was calculated in Equation (8.80).